# Numerical simulation and optimisation of micro-EDM using geometrical methods and machine learning

A thesis submitted to the University of Wales, Cardiff

for the degree of

Doctor of Philosophy

By

Anthony Benoît Surleraux

Materials and Manufacturing
School of Engineering
University of Wales, Cardiff
United Kingdom

July, 2015

# Abstract

As the need for smaller, more compact and integrated products has evolved, it is no surprise that manufacturing technologies have significantly evolved in order to make miniaturisation to smaller scales possible. More specifically non-conventional machining technologies, relative newcomers in the field of machining, have proven well suited to the task at hand.

Among those technologies is micro-EDM (short for Electrical Discharge Machining) that has been the subject of numerous developments.

A certain number of variants of micro-EDM exists among which are wire micro-EDM, die-sinking micro-EDM, micro-EDM milling and micro-EDM drilling. While die-sinking macro-EDM is quite common, its micro counterpart isn't due to problematic tool wear.

In order to optimise the die-sinking micro-EDM process in terms of time and cost and make its use more interesting and viable, the present work aims at optimizing the initial tool shape so that it compensates for future wear.

The first step was to design a simulation tool effectively able to predict the location and magnitude of wear during the simulation process. An iterative geometrical method was developed, first using NURBS as support geometries then voxels embedded in an octree data structure in order to improve speed and accuracy.

The input parameters used in the simulation were initially taken from empirical data. However those could be tedious to acquire and, in order to simplify the process, some approaches using multi-linear regression models were used to link the machining parameters to the expected output.

The third step was to make use of the simulation tool and the results it provided to design a tool optimisation algorithm that would iteratively test tool shapes and compare the resulting workpieces with the targeted result.

Finally, a neural network was trained with optimal tool shapes corresponding to various desired results in order to not have to redo potentially lengthy simulations.

# Acknowledgements

I would like to thank and express my special appreciation to my supervisor, Dr Samuel Bigot for his invaluable input, patience and dedication during those years. He has given me the opportunity to embark in this long and captivating journey that a PhD and its culmination, the thesis, are.

Many thanks to Dr Jean-Philippe Pernot, a former teacher of mine that took the time and energy to follow me after my graduation. His advice and love of mathematical formalisation were greatly appreciated.

To Dr Pierre Kerfriden, thanks for his great ideas that have given me the basis for much of my work as well as for the patience he has shown when came the time to correct my thesis.

I am indebted to my brother, Michael, that has often helped me out when I needed and was always there for me.

To my parents, Marc and Yong, I would like to express my gratitude for their continuous support and love. They have taught me everything a school can't. I wouldn't be where I am without them.

Above all I would like to thank Cristina for her unwavering love and support. I know I can always count on her. Simply put, she's the best.

“La Victoire appartient aux plus persévérants”

- Napoléon Bonaparte

# Declaration

This work has not previously been accepted in substance for any degree and is not being concurrently submitted in candidature for any degree.

Signed ....................................................(Candidate)

Date...............................

**Statement 1**

This thesis is being submitted in partial fulfilment of the requirements for the degree of PhD.

Signed ....................................................(Candidate)

Date.................................

**Statement 2**

This thesis is the result of my own investigations, except where otherwise stated. Other sources are acknowledged by footnotes giving explicit references. A bibliography is appended.

Signed ....................................................(Candidate)

Date.................................

**Statement 3**

I hereby give consent for my thesis, if accepted, to be available for photocopying and for inter-library loan, and for the title and summary to be made available to outside organisations.

Signed ....................................................(Candidate)

Date.................................

# Table of contents

# List of figures

# List of tables

# List of notations

The various notations that are used in the remainder of the document are given here. They are separated into different sections in order to be more easily searchable. Notations in bold are vectors.

**Electrical discharge machining general parameters**

| Symbol | Units | Description |
|---|---|---|
| $t_{off}$ | s | Time-off interval |
| $t_{on}$ | s | Time-on interval |
| $t_{spark}$ | s | Discharge duration |
| $I_{peak}$ | A | Peak current |
| $V_{peak}$ | V | Peak voltage |
| $V_{gap}$ | V | Gap voltage |
| $UR$ | $m^3$.s-1 | Unit removal rate |
| $E_d$ | J.m-2 | Energy density |
| $r_c$ | m | Plasma channel radius |
| $C_d$ | m | Crater diameter |
| $V_{crater}$ | m3 | Crater volume |
| $F_c$ | % | Energy distribution workpiece |
| $E_{cond}$ | % | Energy lost by heat conduction |
| $E_{debris}$ | % | Energy absorbed by debris |
| $M_g$ | m | Machining gap |

## EDM Thermal models

| Symbol | Units | Description |
|---|---|---|
| $T$ | K | Temperature |
| $r$ | m | Radial distance |
| $z$ | m | Vertical distance |
| $t$ | s | Time |
| $K_t$ | W.m-1.K-1 | Thermal conductivity |
| ρ | kg.m-3 | Material density |
| $C_p$ | J.kg-1.K-1 | Specific heat capacity |
| α | m2.s-1 | Thermal diffusivity |
| α' | m2.s-1 | Adjusted Thermal diffusivity |
| $m$ | J.kg-1 | Melting heat |
| $T_m$ | K | Melting temperature |
| $q$ | W.m-2 | Plasma heat flux |
| $T_i$ | K | Initial temperature |
| ierfc(x) | No units | Integral Error Function |
| erf(x) | No units | Error function |
| erfc(x) | No units | Complementary error function |
| $T_{eq}$ | K | Crater temperature limit |

## NURBS, Octrees and the simulation tools

……

| **Symbol** | **Units** | **Description** |
|---|---|---|
| $\mathbf{U}$ | No units | B-Spline knot vector |
| $u_i$ | No units | B-Spline knot value |
| $N_{i,0}$ | No units | i-th B-Spline basis function of degree 0 |
| $N_{i,p}$ | No units | i-th B-Spline basis function of degree p |
| $\mathbf{C}_p(\mathrm{u})$ | No units | NURBS Curve of degree p |
| $\mathbf{P}_\mathrm{i}$ | No units | Control point |
| $w_\mathrm{i}$ | No units | Weight associated to a control point $\mathbf{P}_\mathrm{i}$ |
| $\mathbf{S}_{p,q}(u,v)$ | No units | NURBS Surface of degrees $p$ and $q$ in the $u$ and $v$ directions |
| $\mathrm{N}_{\mathrm{leaves}}$ | No units | Number of leaf nodes in an octree |
| $D_g$ | m | The simulation's objective depth |
| $\mathbf{S}_e(u, v)$ | No units | NURBS Surface of degrees $\mathrm{p_e}$ and $\mathrm{q_e}$ in the u and v directions that represents either the tool ($e$=$t$) or the workpiece ($e$=$w$) |
| $\Delta z$ | m | Increment of the tool descent |
| $V_e$ | $\mathrm{m}^3$ | Volume enclosed by the NURBS patch $\mathbf{S}_e$ |
| $U_e$ | No units | Parametric space of the NURBS patch $\mathbf{S}_e$ |
| $T_{k,h}$ | No units | Triangle part of a quadrangle that locally approximates $\mathbf{S}_e(u_k, v_k)$ |

| Symbol | Units | Description |
|---|---|---|
| $D_b$ | No units | Ratio to the best volume estimation |
| $D_f$ | No units | Ratio to the fastest volume estimation |
| $V_e^r$ | m$^3$ | Volumes of the crater for the workpiece ($e$=$w$) and the tool ($e$=$t$) |
| $\omega_e^{[k]}$ | No units | Unit warping vector |
| $\Delta V_e$ | m$^3$ | Difference between the current volume enclosed by the NURBS patch $\mathbf{S}_e$ and the initial volume enclosed by the NURBS patch $\mathbf{S}_e$ |
| $T_v$ | m$^3$ | Tolerance on the volume removal process |
| $\mathbf{C}_e^{[k]}$ | No units | Centre of the sphere used to add a crater at iteration $k$ on patch Se |
| $\Pi_{\mathrm{e}}^{[k]}$ | No units | Plane that includes $C_e^{[k]}$ and has $\omega_e^{[k]}$ as a normal vector |
| $d_{lower}$ | m | Lower bound when approximating the distance between two nodes |
| $d_{upper}$ | m | Upper bound when approximating the distance between two nodes |
| $d$ | m | Actual smallest distance between two elements |
| $d_{supremum}$ | m | Smallest of upper bounds |
| $s_{res}$ | m | Resolution to reach when searching for the minimum distance between two octrees |

| **Symbol** | **Units** | **Description** |
|---|---|---|
| $V_{threshold}$ | V | Voltage below which a spark can be detected |
| $I_{start}$ | A | Current at which a spark can be detected |
| $I_{end}$ | A | Current at which a spark can no longer be detected |
| $S_p(t)$ | No units | The sparks presence function |

### Tool optimisation

| Symbol | Units | Description |
|---|---|---|
| $W_{target}$ | No units | Target workpiece |
| $W_{virtual}$ | No units | Virtual workpiece |
| $W_{result}$ | No units | Resulting workpiece after an iteration |
| $T_{virtual}$ | No units | Virtual tool |
| $A\%$ | % | Accuracy of an iteration |
| $A_{Wtarget}$ | $\mathrm{m}^2$ | Target workpiece feature area |
| $\varepsilon$ | $\mathrm{m}^2$ | Mismatch area between the target and the result workpieces |
| $R_e$ | m | Crater radius for the electrode $e$ |
| $D_e$ | m | Crater depth for the electrode $e$ |
| $\gamma$ | No units | Ratio between $R_e$ and $D_e$ |
| $\beta$ | No units | Ratio between $V_t$ and $V_w$ |

# Chapter 1

# Introduction

The famous speech of Richard Feynman (Feynman, 1960) given in 1959 is a testimony to the beginnings of the fields of micromanufacturing and nanomanufacturing as well as their associated challenges. The need for smaller and smaller components has naturally developed as the electronics industry was seeking to improve their processes for the manufacturing of electronic components. Since then, a broad field of industries have found practical uses in micro-scale components and features. Among them are the IT components industry, the medical and biomedical industries, telecommunications and automotive industries (Alting, Kimura, Hansen, & Bissacco, 2003).

The historical fact that the electronics industry has driven the development of micro components explains that processes and technologies related to silicon-based microstructures are significantly more advanced and mature than those related to metal, polymers or ceramics (Menz, 2002).

Micromanufacturing is part of a greater ensemble, micro-production. The object at the centre of it is the micro-product itself made of micro-parts. Around the product are processes such as micro-control, micro-assembly (Van Brussel, et al., 2000) and micro-measurement (Masuzawa, 2000). A global overview of those notions is depicted in Figure 1.

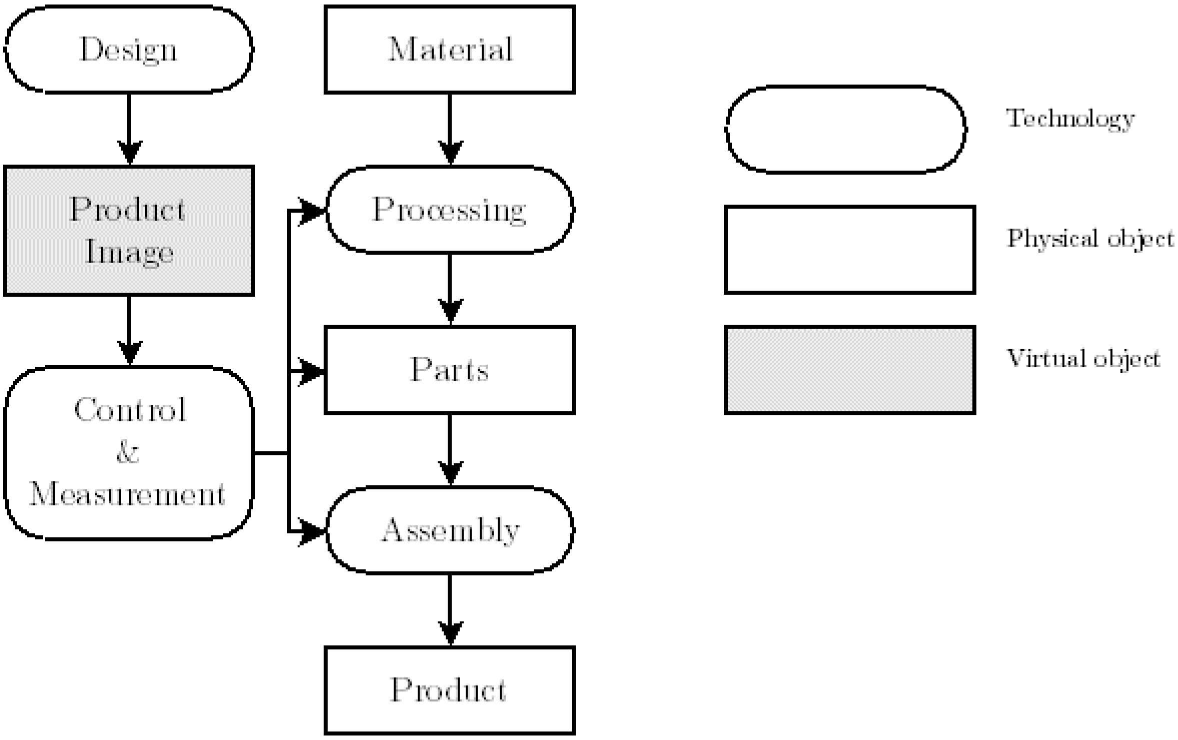

Figure 1: Overview of the micro-production concept and its components. (Masuzawa, 2000)

The definition of micro-products is itself subject to discussion. A first approach, and the most natural, would be to limit any considerations to size. The term “micro” could be taken literally as 1 to 999 µm or. However, the constant evolution of manufacturing processes’ abilities makes it hard to clearly define a lower bound for dimensions. Using the term “micro” could also be associated with difficulty: something too small to be easily machined. The definition of a micro-element and the exact figures of its size vary enormously between people, eras, machining process or material. However a recurring range can be grossly defined as anything that involves features between 1 to 500 µm.

In addition to the definition based on size, micro-products also possess another characteristic which is the high level of integration of components and functionalities.

Manufacturing not related to the electronics industry has developed recently to the point that current micro-manufacturing technologies aren't the most adapted for mass production of micro-parts. In order to make the various products available to an increasing number of customers and at a lower cost, pressure has been put on the development and improvement of micromanufacturing (Alting, Kimura, Hansen, & Bissacco, 2003).

Table 1 presents an overview of the various manufacturing processes that have been applied to the manufacturing of micro-products.

Micro-products are often the result of collaboration between various fields due to the complexity of their applications. For example, the design of a fluid chemical analysis sensor requires input from disciplines such as chemistry, biology and fluid mechanics. This necessarily different approach towards product design has an impact in the way its manufacturing is designed.

In addition the inherent advantages linked to their ability to machine microscopic features, an additional advantage is worth mentioning.

The development of new and innovative materials that possess unique mechanical and/or thermal properties has completely changed the field of product design. The innovation in the field of materials leads to similar innovation in products. Among them are tungsten carbide, titanium alloys, nickel alloys and other super alloys. They are characterised by excellent properties such as a very high hardness or a lower sensitivity to corrosion or weight. However these new materials are also often considered to be hard to machine (Jahan, Rahman, & Wong, 2011) which leads to the development of technologies with the potential to machine these.

Table 1: Technology overview for micro products (Alting, Kimura, Hansen, & Bissacco, 2003), (Masuzawa, 2000), (Dimov, Brousseau, Minev, & Bigot, 2012).

| **Working Principle** | **Material Interaction** | | | |
|---|---|---|---|---|
| | **Subtractive** | **Mass Containing** | **Additive** | **Joining** |
| **Mechanical force** | Cutting, grinding, blasting, ultrasonic machining | Rolling, deep drawing, forging, punching | | Ultrasound, cold pressure welding |
| **Melting/ Vaporization (Thermal)** | Electrical discharge machining, laser beam machining, electron beam melting | | Chemical vapour deposition, physical vapour deposition | Welding, soldering, bonding (ball, wedge, compliant) |
| **Ablation** | Laser beam machining, focused ion beam, ultra-short pulse laser | | | |
| **Dissolution** | Electro-chemical machining, isotropic or anisotropic etching, reactive ion etching | | | |
| **Solidification** | | Casting, injection moulding | | |
| **Recomposition** | | | Electroforming, chemical deposition | |
| **Polymerisation or Lamination** | | | Stereolithography, photoforming, polymer deposition, nanoimprint lithography, magnetolithography, laser printing | gluing |
| **Sintering** | | Combination of mechanical and thermal principles | | |

In order to make those materials completely viable for mass production, it is required to possess mature manufacturing technologies able to process them. Once such a condition is met, the use of innovative materials can be made universal and open up new applications.

In the micro-manufacturing field in particular, several main technologies have been developed for the machining of those “difficult to cut” materials. The contactless nature of micro-EDM makes it a very promising technology when considering those new high-performance materials. A certain number of challenges exist in the development of micro-EDM, the main one being its application to large-scale production.

Among the technologies reported in Table 1, micro-EDM can be considered one of the most promising. As previously mentioned, its macro contactless nature that preserves the workpiece from any kind of residual stresses or debris left on the workpiece surface and its ability to machine any conductive material are its core strengths.

Additionally it possesses a certain number of other characteristics:

- The capability to machine any kind of complex three-dimensional feature. Two main variants of micro-EDM exist that are well suited for these applications. The first, die-sinking micro-EDM (plunge micro-EDM, conventional micro-EDM are other names) aims at reproducing a 3D cavity through the use of a tool shaped negatively to the feature to produce. The second, micro-EDM milling uses a rotating cylindrical or tubular electrode to machine the feature layer-by-layer. Those two methods are able to produce very sharp edges (up to the radius of the electrode used added to the machining gap) as well as cavities and protrusions that would be difficult to accomplish with conventional technologies.

- The machining speed of micro-EDM, around 0.6-6mm$^3$/h, (Bigot, Ivanov, & Popov, 2005)(depending on the variant and the parameters considered) is significantly lower than other technologies, conventional or otherwise. Laser beam machining (LBM), for one, has a greater material removal rate ($> 10^4$ mm$^3$/min) (Knowles, et al., 2006).

- The tool wear of the micro-EDM processes (except for wire-µEDM) is extremely important. The reason lies in the intrinsic nature of the process. The electrical discharges at the origin of the removal of the material don't discriminate fully between the tool and the workpiece. As a result, the tool is inevitably worn. Due to the complex and stochastic nature of the process, it is hardly predictable.

- An excellent surface finish with an average roughness $R_a$ smaller than 0.1 µm (Maradia, et al., 2013) is possible with micro-EDM technologies and is another area it shines when compared with other technologies. The roughness is linked to the size of the craters produced by the process and is strictly dependent on the used process parameters. It is noteworthy that while die-sinking or drilling micro-EDM are capable of achieving such a surface finish, wire and milling micro-EDM deliver a slightly worse roughness (Bigot, Ivanov, & Popov, 2005) ($R_a > 0.5$ µm for milling, $R_a >$ 0.2 µm for the wire process). It is of note that some research has focused on the improvement of micro-EDM milling accuracy (Qian, Wang, Ferraris, & Reynaerts, 2013).

Considering those elements, it appears that micro-EDM is characterised by several main advantages that are offset mainly by its machining time. Because of the tool wear, the already significant machining time is increased. Die-sinking micro-EDM for example would require the use of half a dozen or so electrodes (Maradia, et al., 2012) before being obtaining the desired feature within the specified tolerances. However, proven methods exist in the cases of micro-EDM milling and micro-EDM drilling to compensate for this wear.

The aim of the present work is to explore the possibilities to further improve and optimize the die-sinking micro-EDM process in order to increase its competitiveness and viability in the field of non-conventional micro-manufacturing technologies. Die-sinking micro-EDM is characterized by its ability to produce complex 3D cavities with a surface finish that is superior to the one achievable by micro-EDM milling (Bigot, Ivanov, & Popov, 2005). There is a knowledge gap in the prevention or compensation of tool wear in die-sinking micro-EDM that would enable it to become a true industrial process.

# Chapter 2

# Micro Electrical Discharge Machining

## 2.1. Overview

The present section aims at giving a global presentation of micro-Electrical Discharge machining and its natural ancestor EDM. Firstly, a brief history of EDM is given presenting the main actors and events in the development of this machining process. A second part presents the main principles of EDM with a focus on the discharge that is at the centre of the whole process.

The next section deals with the main differences between micro-EDM and its macro equivalent and underlines that those differences, while based on them, aren't limited to size considerations.

Section 2.5 presents the main variants of conventional micro-EDM as well as the main issues and advantages linked to each of them. Several examples of their applications is also provided.

Next the main aspects of a micro-EDM machine are covered. The pulse generator, servo control and dielectric circulation systems are described.

Section 2.7 aims at giving an overview of the state of the art in the field of micro-EDM modelling as well as simulation. This section leads to a conclusion of the state of the art in the simulation field which is at the basis of the present work.

## 2.2. History

While electrical discharges and arcs are a commonly known phenomenon nowadays, it has still been studied extensively by quite a few researchers across the ages.

The first appearance of the use of discharges in manufacturing dates to the mid-1600s when Robert Boyle tried to create metal powder from a solid rod and gave the first description of material removal through electrical discharges.

However, the parenthood of Electrical Discharge Machining as a viable non-conventional machining process, is attributed to the couple of Russian physicists Natalya and Boris Lazarenko during World War II (Lazarenko & Lazarenko, 1944).

They were tasked in 1943 to find a solution to the problematic erosion of tungsten electrical contacts and, consequently, studied the erosion process extensively. While they did not a find a solution to that specific issue, they also described how the erosion process could be well-controlled if the electrodes were to be immerged in a dielectric fluid. Their publication describes an RC circuit and defines specific energies to charge into the capacitor in order to obtain a stable machining process.

While the initial applications of this newly controlled technology could be used for material removal, the Lazarenko realised that a certain distance needed to be maintained between the tool and the workpiece in order to improve and stabilize the process further. That distance is known as the machining gap and is maintained through the use of a servo-control.

The accession of EDM to a commonly used workshop technology didn't happen until the 1950s when it was perceived as a machining process able to fulfil the ever-increasing needs of the market. Once known as a simple removal machine used in the removal of broken taps and drills from aluminium castings, it became a widespread industrial process most notable with the transition from hand-fed electrodes to CNC controlled 6 axis machining (Jaham, 2013).

The physics behind the material removal process as well as the control of the machining gap were both at the centre of research. Due to the nationality of the Lazarenko, the pioneers of EDM, most of the researchers working on that subject were from the then socialist countries. Most of the machines and tools newly developed at the time were done so by the Research Institute of Moscow. Many young researchers studied in Moscow before bringing the technology back to their home country (Schumacher B M, 2013). Livshiz, director of the EDM group at the Research Institute of Moscow published a review of the variants of EDM (Livshiz, 1957).

The last seventy years have seen an increase in the popularity and applications of EDM and it is now a well-established and controlled non-conventional manufacturing process. The micro-EDM process did not evolve concurrently to its macro counterpart. This specific micro technology did not become popular until the need for miniaturized features became apparent. The first breakthrough for micro-EDM happened when its capacity to drill micro-holes was demonstrated by Karafuji and Masuzawa (Karafuji H, 1968) when they made a micro-hole in a carbide plate of 50 µm.

The final development of the micro-EDM technology had to wait until the advent of software functions that enabled planetary movements of electrodes.

The next section provides with an in-depth presentation of the principle involved in EDM as well as micro-EDM.

## 2.3. Principle

Regardless of the variant of EDM or micro-EDM, the underlying concepts and principles remain the same and are the characteristics of the process (Jameson, 2001).

Two electrodes (the tool and the workpiece) shown in Figure 2 are immerged in a dielectric fluid, usually deionized water or mineral oil (Jaham, 2013), and submitted to an electrical current. As the electrodes get closer to each other, the dielectric breaks down and the current flows between them leading to the apparition of a spark. The spark is a plasma channel that is at the origin of thermal energy which in turn leads to the vaporization and melting of the electrodes' material. Once the current is stopped, the dielectric fluid rushes back where the plasma was and evacuates the resulting debris.

The result of this repeated process if a controlled series of electrical discharges that leaves craters on the electrodes' surfaces.

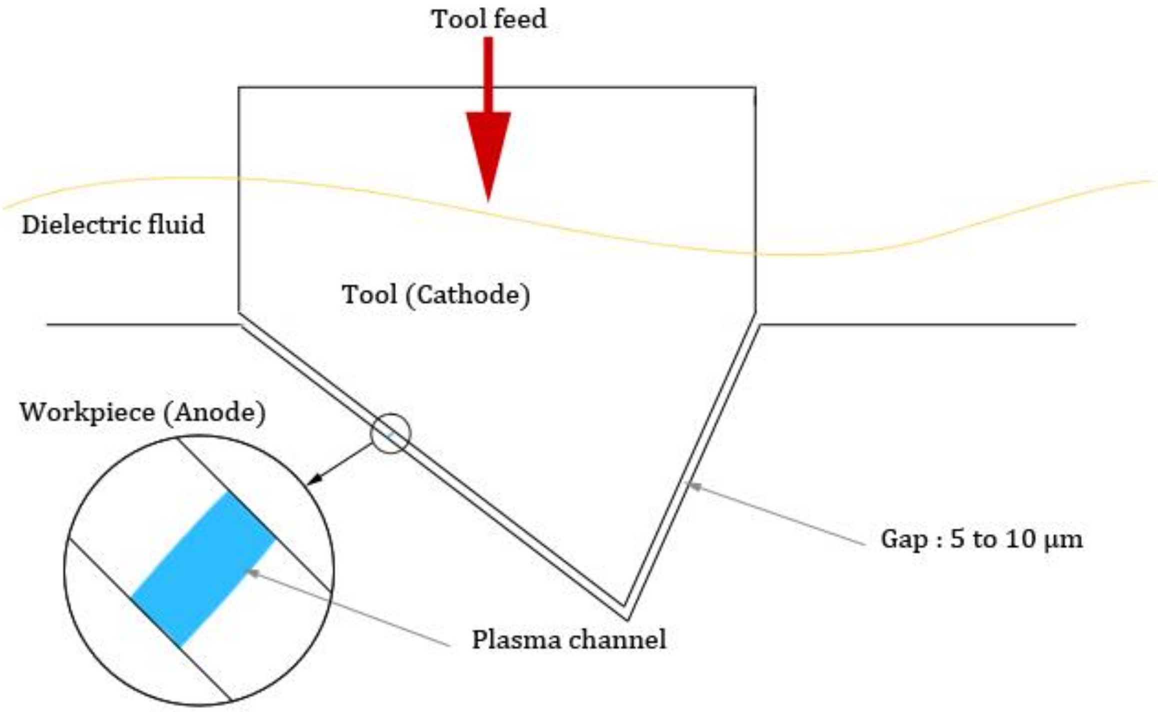

Figure 2: General principle of EDM.

In micro-EDM, those sparks occur between a positively charged anode and a negatively charged cathode. As the process relies on the application of an electric field between both electrodes, they must necessarily be made of electrically conductive materials (It is noteworthy to point out that some techniques exist to introduce the ability to machine non-electrically conductive materials). When the electric field is applied through an applied voltage, its force increases as the distance decreases. The electrons emitted by the cathode collide with neutral atoms that provokes a release of ions and electrons attracted by the increasing electric field.

The increase in the electric field slowly deteriorates the dielectric fluid present between the electrodes. The resistivity of the dielectric is reduced over time until it reaches the point it can act as an insulator and can't prevent the apparition of a spark. The formation of the spark leads to a reduction of the voltage between the two electrodes to zero (at this point, the current flows freely from one electrode to another nullifying the initial difference in electric potential). The spark vaporizes and melts the material which leads to the apparition of gas bubbles (hydrogen, carbon and various oxides) inside the dielectric.

The workpiece material being melted is re-solidified by the dielectric. Those debris are evacuated by the dielectric through flushing. However some of the debris remain in the machining area, decreasing its resistivity. The current is then shut during a time known as the time-off interval ($t_{off}$). The vapour bubble in the machining area collapses as the current flow is interrupted and the dielectric rushes and cools electrodes. With new dielectric in place, the process can be repeated (Takahata, 2009).

The following figures (Figure 3, 4 and 5) illustrate the events previously described that occur during an EDM discharge.

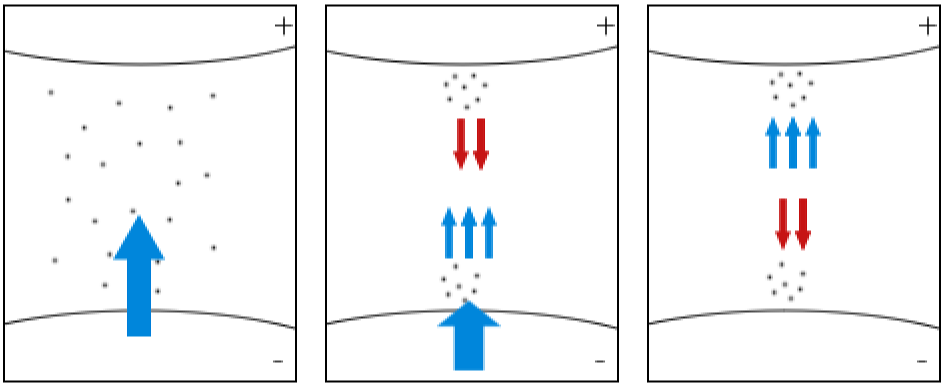

Figure 3: EDM Pre-discharge phase. Electrons and ions are attracted towards the cathode and anode respectively.

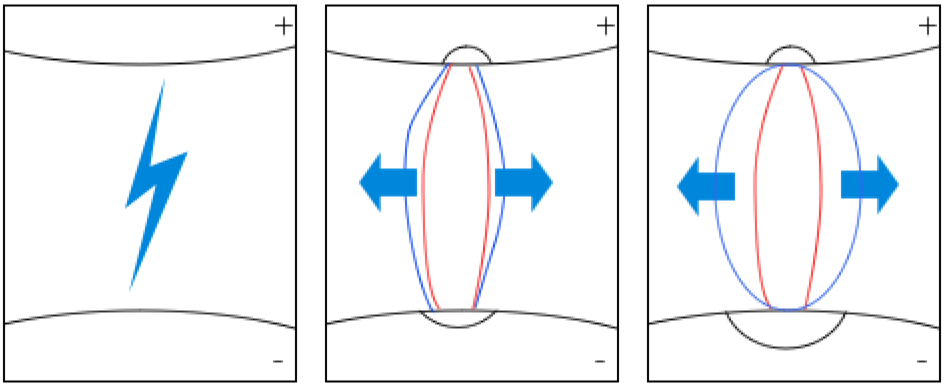

Figure 4: EDM discharge phase. The plasma channel is in red while the expanding gas bubble is in blue.

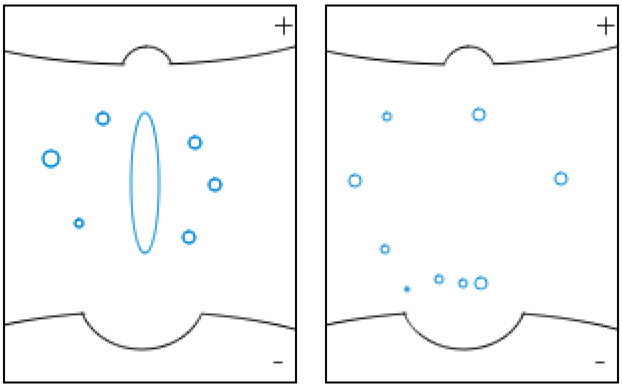

Figure 5: EDM post discharge phase. The plasma channel has collapsed and the gas bubble implodes. The dielectric rushes back in and evacuates debris.

The previous figures also underline the fact that the workpiece isn't the only electrode to be affected by the discharge. Thermal energy dissipation also occurs at the tool leading also to material removal. While inevitable, it is possible, through the choice of adequate process parameters to minimize the removal of material on the tool.

Several main parameters govern the formation of the spark as well as its intensity. They are the peak current ($I_{peak}$), gap voltage ($V_{gap}$), time on ($t_{on}$) and time off ($t_{off}$).

There are quite a number of variants of EDM (and, as a result, of micro-EDM) that are mainly differentiated by the type of electrode used and the relative movement between the workpiece and the tool.

## 2.4. Main differences between micro-EDM and EDM

Even though micro-EDM and EDM have the same underlying principle, a process based on a controlled series of electrical discharges, there are some important differences that need to be underlined. While the dimensions are the main difference, the issues related aren't solved by a simple downscaling of the problem.

The scale of the tool is the most obvious difference. As a result, the technologies used to make those electrodes differ substantially.

The micro EDM process differs also by the energies that are used during machining. Those are significantly lower in order to limit what is known as the unit removal rate per spark (abbreviated $UR$) and to protect the tools that are much more sensitive to the energies being used due to their small size. This fact leads to smaller craters on the workpiece and the tool and, therefore, a high quality surface finish (Uhlmann, Piltz, & Doll, 2005).

Additionally, the erosion phenomenon is preponderant when considering the micro-scale process against the macro one. In (Zahiruddin & Masanori, 2012), this difference in behaviour was studied. The energy density (the ratio between energy absorbed by the workpiece and the area of the plasma channel) is higher in the micro-scale process and is considered to be a good indicator of machining efficiency.

In EDM, even when considering similar energy conditions, it is possible to note a discrepancy in performances between high peak current discharges (characterized by a short spark duration) and low peak current discharges with a longer discharge duration (Kunieda, Lauwers, Rajurkar, & Schumacher, 2005).

Table 2 presents a comparison between the parameters used in micro-EDM and macro-EDM. It is noticeable that the discharge duration when considering the case of micro-EDM is significantly shorter than in macro-EDM. This fact prevents the plasma from expanding fully and result in an increased power density (the heat source being smaller, the density therefore increases). The energy density, in comparison with macro-EDM, is greater by a factor of thirty.

Another main difference between micro and macro-EDM lies in the flushing efficiency of the dielectric fluid. As previously mentioned, in addition to increasing the control and stability of the process, the dielectric is also used to flush the debris resulting from the sparks. In micro-EDM the small size of the various elements (most notably the machining gap) make that flushing more difficult and less efficient (Katz & Tibbles, 2005).

The requirements in terms of axis movements are significantly higher in micro-EDM where the precision required are within the range of tenth of microns.

Table 2: Comparison between micro-EDM and EDM parameters (Zahiruddin & Masanori, 2012).

| **Parameters** | **Symbol** | **Units** | **µEDM** | **Conventional EDM** |
|---|---|---|---|---|
| **Discharge current** | $I_{peak}$ | A | 1.14 | 10.36 |
| **Discharge voltage** | $V_{peak}$ | V | 24 | 17.19 |
| **Discharge duration** | $t_{spark}$ | µs | 0.07 | 17 |
| **Crater diameter** | $C_d$ | µm | 4.25 | 68.4 |
| **Volume removed per pulse** | $V_{crater}$ | $\mu m^3$ | 1.90 | 972.5 |
| **Energy distribution in workpiece** | $F_c$ | % | 10.37 | 34 |
| **Energy lost by heat conduction** | $E_{cond}$ | % | 6.02 | 30 |
| **Energy absorbed by debris** | $E_{debris}$ | % | 4.35 | 1 |
| **Plasma radius** | $r_c$ | µm | 6.8 | 171.12 |

The polarity used for the generator also differs. The phenomenon in the plasma channel is a directional one. As a result, one electrode is used more than the other. Due to the important effects of tool wear in micro-EDM, the polarity is reversed so that the tool is worn less than the workpiece.

The final difference between the two processes, and the most important one, is the dimension of the plasma channel that occurs during a discharge.

## 2.5. Types of micro-EDM

### *2.5.1. Micro-Wire EDM*

Micro-wire electrical discharge machining (µWEDM) is a variant of the general concept of µEDM in which a metallic wire of a diameter that can go down to 20 µm (Klocke, Lung, Thomaidis, & Antonoglou, 2004), typically brass, comes off a spool and is fed through the workpiece submerged in a dielectric fluid that also handles the flushing of the debris. The wire is held by two diamond guides CNC-controlled allowing µWEDM to cut intricate shapes. The fact that both of the wire guides can be independently controlled makes the fabrication of tapered shapes possible. The cutting path known as a kerf is greater than the width of the wire since sparking occurs from the edge of the wire. This can easily be predicted and compensated in most cases. Figure 6 depicts the general concept of µWEDM.

The main issue associated with micro-wire electrical discharge machining is wire breakage that drastically reduces the machining efficiency of the process. This issue arises from the difficulties associated with applying a tension on such a small wire (Han, Cheng, Feng, & Isago, 2008).

A certain number of control systems have been developed in order to detect on-line any abnormality associated with wire breakage and prevent it (Kinoshita, Fukui, & Gamo, 1982), (Rajurkar & Wang, On-line monitor and control for wire breakage in WEDM, 1991), (Yan & Liao, 1996).

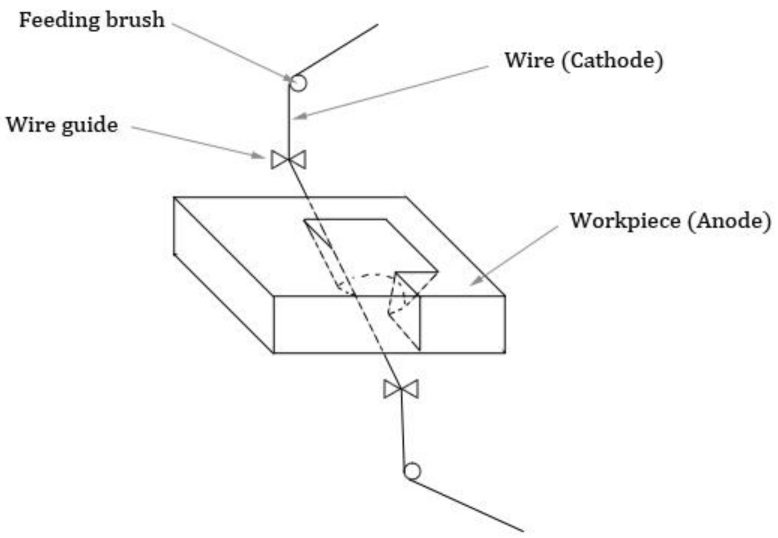

Figure 6: General concept of wire EDM.

### *2.5.2. Micro-EDM die-sinking*

In Die-Sinking micro-EDM the tool and the workpiece, placed in a dielectric fluid (usually oil), are connected to a power supply thus creating an electrical potential. After the breakdown of the dielectric fluid, a plasma channel forms allowing a spark to jump.

The macro version of Die-Sinking micro-EDM (sometimes known as conventional EDM) is used with complex electrode shapes in order to produce the inverse shape. The resulting piece is then usually used as a mould in other manufacturing processes such as plastic micro-injection (Ho & Newman, State of the art electrical discharge machining (EDM), 2003).

One of the main issues when dealing with die-sinking micro-EDM is the tool wear illustrated in Figure 7. This does not apply to wire-EDM in which the wire is continuously fed and replaced during the process. The tool is worn during the process which leads in a change in its geometry. A modification in the shape of the tool will have adverse consequences on the workpiece's resulting geometry.

Die-sinking micro-EDM suffers the most from this phenomenon and a typical die-sinking manufacturing of a complex three-dimensional shape usually involves the use of a dozen or more electrodes before achieving the desired result within acceptable tolerances.

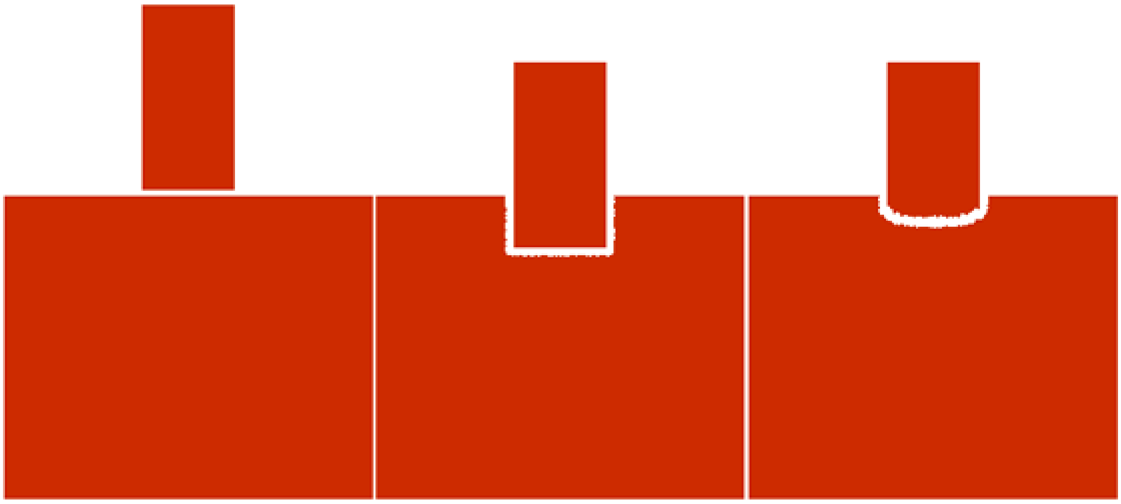

Figure 7: The tool wear problem in die-sinking micro-EDM. a) Before machining b) Ideal machining c) Actual machining

This issue associated with the tool wear is the main reason why micro-EDM milling is the preferred method to produce complex 3D cavities.

### *2.5.3. Micro-EDM milling*

Micro-EDM milling is a type of micro-EDM in which electrodes with simple shapes (usually tubular or cylindrical electrodes) are used in order to produce 3D cavities layer by layer. The process is quite similar to conventional milling in the sense that the tool electrode movement determines the cavity that will be produced.

Micro-EDM milling is significantly affected by the wear problem described previously. However various proven methods exists in the case of micro-EDM milling.

The linear compensation method (LCM) (Yuzawa, Magara, Imai, & Sato, 1997) compensates wear by feeding the electrode into the workpiece after it has moved a certain distance along the tool path. It assumed that the ratio of the electrode feed depth to the moving distance is a constant.

A major drawback of this method is that it is ill-suited to generate complex three-dimensional shapes. It is usually restricted to the machining of 3D cavities that possess straight side walls (Kuo, Chen, Wu, Yan, & Masuzawa, 1997).

The use of an electrode with a simple shape (cylindrical or square-shaped section) along pre-defined paths has been proposed by (Yu, Masuzawa, & Fujino, 1998) to circumvent the issue of tool wear. This method, known as the Uniform Wear Method (UWM), aims at compensating the tool wear through layer-by-layer machining. When the outline of a layer is machined, the tool loses its sharp edges and becomes rounded due to wear. However when the inner part of the layer is machined, due to wear on the axis of the tool feed, the tool recovers its original shape (Narasimhan & Rajurkar, 2005).

The strategy here is to first machine the outlines of a layer of the three-dimensional cavity thus creating wear on the edges of our electrode then to machine the inner part of our layer. Tool feed axis wear will appear destroying the part of the tool where edges were worn and presenting a tool without edge wear for the next layer.

A more recent trend aims at using the Uniform Wear Method with real-time information obtained during the process in order to correct the paths that have been defined previously through the application of the UWM before machining.

(Bleys, et al., 2002) proposed to add on-line tool wear measurement as well as real-time control of the tool feed axis in order to perform wear compensation without resorting to off-line prediction techniques.

### *2.5.4. Micro-EDM drilling*

This type of EDM is quite similar to die-sinking EDM and only differs by its power supply. In the case of die-sinking EDM, the power supply is quite sensitive in order to protect the electrode. In the drilling of small holes, the power supply is quite aggressive in order to blast through the workpiece. This process is commonly used to drill holes through very hard metals allowing wire EDM to use the hole as the start of the wire cut. The process uses cylindrical or tubular electrodes. The tubular electrodes are commonly used when making holes with a great aspect ratio (this situation is known as deep drilling) since it is possible to make the dielectric flow through the tool to improve the flushing and evacuation of debris.

Micro-EDM drilling is the main application of micro-EDM. Among its applications are the machining of diesel engines injection nozzles (Potz, Christ, & Dittus, 2000) or holes in turbine blades for the aerospace industry (Guitrau, 1997).

The machining of holes has the advantage of not being concerned with the wear issue as it is easily compensated in the z-direction through the use of long electrodes. It is of note that the wear is easily predictable in the case of tubular electrodes but not much so when using rods as the flushing inefficiency severely alters the wear phenomenon and results in low quality holes (Pham, Ivanov, Bigot, Popov, & Dimov, 2007).

Considering the difficulty to machine cylindrical electrodes small enough to be used in the drilling of micro-holes and the clamping issues associated with them, those tools are commonly made directly on the machine with a process known as micro-EDG (micro-Electrical Discharge Grinding). Micro-EDM is used to fabricate electrodes with a small diameter from a bigger electrode.

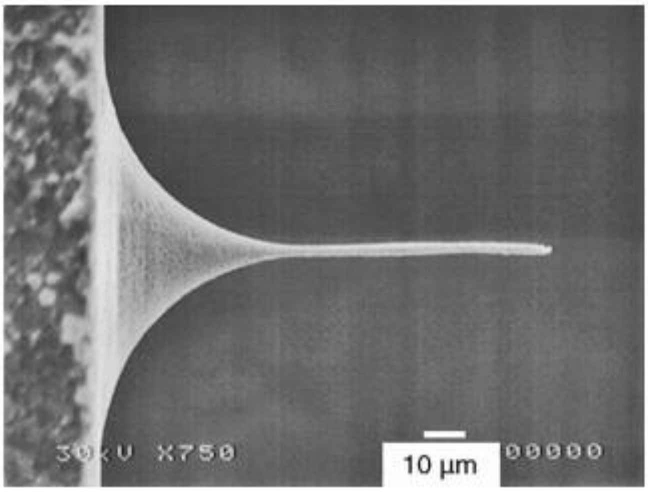

Figure 8: 2.8 µm electrode made of cemented tungsten carbide using super fine particles (SWC). Reproduced from (Han, Yamada, Kawakami, & Kunieda, 2006).

### *2.5.5. Concluding remarks*

From this brief overview of the various variants of micro-EDM that exist, most of them possess proven methods to either compensate the issue of tool wear or wire breakage in the case of wire micro-EDM.

Only die-sinking is lacking a proven method to negate the effects of tool wear on the process. As a result, this specific variant of micro-EDM isn't well-established. However this isn't the case for its macro-scale counterpart (Jameson, 2001).

Added to the fact that die-sinking possesses some enviable qualities (an excellent surface finish and the ability to machine complex 3D geometries). This is the main reason why it is proposed to bridge the gap between micro and macro-scale EDM through the study of tool wear compensation techniques.

## 2.6 Main components of micro-EDM machines

### *2.6.1. Overview*

As with most machines, micro-EDM machining systems are made of several subsystems all performing a very specific task. These sections aim at giving an in-depth description of those subsystems as well as their performance's influence on the machined result.

Among those subsystems can be found:

- The pulse generator responsible for the application of an electrical current between the tool and the workpiece.
- The axis control systems that ensure a precise relative positioning of the tool and the workpiece.

- The dielectric circulation system that is composed in the circulation system itself as well as a filtering system required to remove the debris.
- The central control unit that acts as the manager of all those subsystems and interacts with the operator through a Human-Machine Interface (HMI).

### *2.6.2. The pulse generator*

Arguably the core component of any EDM system is the pulse generator. Its design and choice are extremely important and depends highly on the specific application that is to be made. The difference between micro-EDM and macro-EDM implies different pulse generators need to be used for each scale. The micro-scale situation requires the minimization of the average energy per discharge especially in a finishing situation where process parameters are chosen to maximize the resulting surface finish quality. As a result, those parameters aim at being the less aggressive as possible.

The selection of a pulse generator is fully dependent on this particular requirement and the ultimate choice of a generator is different in EDM and micro-EDM for this reason. The higher voltages and currents in macro-scale EDM associated with lesser requirements in terms of geometrical tolerances usually lead to the use of an aggressive pulse generator in order to maximize the material removal rate (MRR) of the process.

There are a certain number of pulse generators available that can be classified into different categories (Springborn, 1976):

### 1. Rotary impulse generator

The rotary impulse generator depicted in Figure 9 is based on the DC generator principle which creates a sinusoidal wave. However, since there is no way to control it, this type of pulse generator is rarely used.

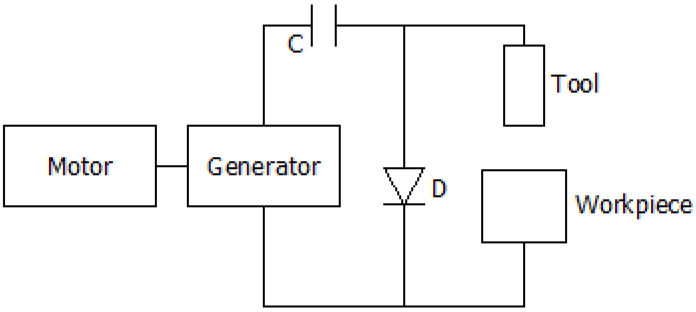

Figure 9: Rotary impulse generator. Adapted from (Mahendran, Devarajan, Nagarajan, & Majdi, 2010)

### 2. Relaxation generator

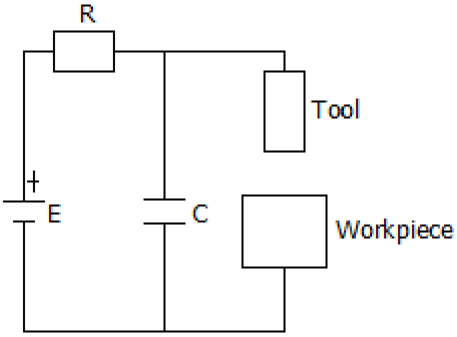

Figure 10: Relaxation generator. Adapted from (Mahendran, Devarajan, Nagarajan, & Majdi, 2010)

The basic principle of the relaxation generator depicted in Figure 10 lies in the charge and the discharge of the capacitor C connected to a power supply E that leads to the generation of a saw tooth voltage waveform.

The capacitor is allowed to charge and discharge when there is a contact between the tool and the workpiece. The duration of the spark is determined by the capacitance of the capacitor and the resistance. Since the resistance is constant, the duration (and therefore frequency) of discharges is dependent on the charging time.

This dependency on the charging explains why this type of transistor results in a small material removal rate.

Additionally, the discharge isn't always uniform due to the variability present in the dielectric medium which leads to a weaker control of the energy per spark. Those drawbacks are overcome by the transistor-type generator which is further described.

### 3. Transistor-type pulse generator

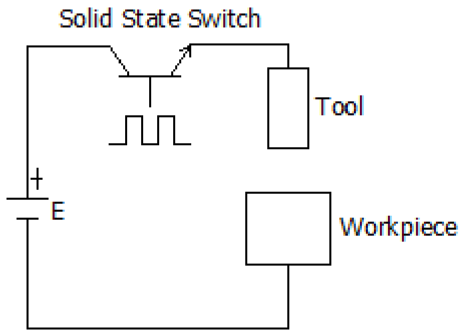

Figure 11: Transistor-type generator. Adapted from (Mahendran, Devarajan, Nagarajan, & Majdi, 2010)

A transistor-type generator is made of a series of resistors and transistors that are placed and connected in a parallel manner to the power supply. The resulting intensity of the current is a direct function of the number of transistors switched on.

The voltage waveform is a rectangular one and offers a significant improvement when compared with the previous two pulse generators. This is due to the absence of capacitors which eliminates the need to wait for their charge. Additionally, this type of generator offers a control over the duration an intensity of a spark and allows for optimisation of the process parameters (Jaham, 2013).

### *2.6.3 The servo control systems*

The control of the distance between the tool and the workpiece is a central consideration of micro-EDM machines. It is one of the main factors that control the quality of the surface finish as well as the accuracy of the various features to be machined.

Therefore, the development of a stable and robust gap control system is of paramount importance for a repeatable and controlled machining (Rajurkar, et al., 2006) (Zhang, Jia, Liu, & Li, 2012).

The usual values for the machining gap in micro-EDM is in the order of magnitude of tens of micros, significantly lower than the usual gap in macro-EDM. This additional constraint makes the development of an accurate servo control system significantly harder and necessary.

Several algorithms dedicated to the prediction of the gap, the tool position and the gap voltage exist and are implemented in the servo control systems. A large machining gap than expected leads to a delayed discharge and a higher value for the gap voltage than set. On the contrary, a smaller gap results in a decreased spark delay and a smaller gap voltage than the reference.

Most systems implement a withdrawal of the tool electrode that enables the increase of the gap voltage in order for the discharge to happen in the correct conditions. Additionally, this system helps avoiding short-circuits due to the electrodes entering in physical contact or the debris potentially remaining in the discharge area (Rajurkar & Wang, 1991).

### *2.6.4 The dielectric circulation and filtering systems*

A critical system on any micro-EDM machine is the dielectric circulation elements. In addition to the circulation of the fluid, the system provides with filtering elements as well as a temperature control. The notion of temperature is quite important considering the fact that, among the various dielectric fluids in use, kerosene is one of the most commons and is of an inflammable nature (Jaham, 2013).

The dielectric circulation system is made of the following items:

- The dielectric fluid (usually kerosene or deionized water)
- The dielectric container
- The low pressure pump
- The high pressure dielectric pump
- The filtering system
- The temperature control of the dielectric fluid

The filtering system is required to keep the dielectric free from the debris. Those debris are solidified metallic particles coming from molten material that has been flushed away from the spark locations.

## 2.7. EDM modelling and simulation

### *2.7.1 Introduction*

One of the drawbacks related to micro-EDM is the action of tool wear during the machining process. As such, the notion of simulation for micro-EDM is of interest as it could potentially increase the knowledge related to the wear phenomenon.

EDM and micro-EDM involve quite a number of different fields such as thermal transfers, hydrodynamics and electrical conduction to cite a few. These various interactions between different fields of physics make the problem of accurately modelling the discharge process that leads to material removal a difficult one.

Pure mathematical modelling has been attempted when considering a single discharge usually involving the heat transfer equation.

Simulation has also been attempted both in the case of a single discharge or the whole process.

This section will provide with some insight into those two approaches applied to EDM as well as micro-EDM.

### *2.7.2. Physics-based modelling*

#### 2.7.2.1. Introduction

Two major situations can be considered that are differentiated by the duration of an electrical discharge. In the case of short sparks, it is supposed that the metal doesn't have sufficient time to be heated and, as a result, material destruction happens mainly by vaporization. In the case of long sparks the thermal aspect becomes preponderant and the material melts. The problem then becomes one of heat transmission. If it is not decided to consider the case of very short discharges, electrical discharge machining can be considered as a heat transmission problem for which the temperature distribution in the workpiece shall be sought in order to determine the shape of the crater. Three main components are to be studied: energy distribution, size and shape of the discharge channel and material ejection. A portion of the energy is evacuated in the dielectric and by radiation, another portion is evacuated in both electrodes by conduction and a negligible part is lost by convection in the workpiece. The exact repartition of the thermal energy relies on different factors that include the boiling temperature of the electrodes' material.

Finally material evacuation has to be considered. Unfortunately all of the molten metal isn't evacuated by the dielectric fluid and considering so will lead to a theoretical material removal rate (MRR) that will be greater than experimental data. This introduces the concept of plasma flushing efficiency which is defined by the fraction of the molten metal that is actually removed.

Work by (Descoeudres, Hollenstein, Walder, & Perez, 2005) has established that the plasma flushing efficiency is dependent on the thermal expansion coefficient of the electrode, the amount of molten material, the plasma channel radius, the thermal properties of material and the flushing conditions.

#### 2.7.2.2. Thermo-electrical modelling

EDM erosion models based on thermo-electrical principles consist in the search of solutions for the heat conduction problem described by the following differential equation:

$$\frac{\partial T}{\partial t} - \alpha \nabla^2 T = 0 \tag{1}$$

$$\text{with } \alpha = \frac{K_t}{\rho C_p} \tag{2}$$

Where α is the thermal diffusivity ($\mathrm{m}^2.\,\mathrm{s}^{-1}$), $K_t$ is the thermal conductivity of the material (in $\mathrm{W.m^{-1}.K^{-1}}$), $\rho$ is the density ($\mathrm{kg.m^{-3}}$) and $C_p$ is the specific heat capacity ($\mathrm{J.kg^{-1}.K^{-1}}$). Some models take the melting heat $m$ into account in the formulation of the thermal diffusivity:

$$\alpha' = \frac{K_t}{\rho(C_p + \frac{m}{T_m})} \tag{3}$$

where $T_m$ is the melting temperature of the material.

The boundary conditions relate to the geometry being considered. Several approaches of the problem exist. Some have used an adiabatic semi-infinite cylinder, a disk heat input and assumed that the energy was equally shared among the cathode and anode (Snoeys & Van Dijck, Investigation of electro discharge machining operations by means of thermo-mathematical model, 1971) (Snoeys & Van Dijck, Plasma channel diameter growth affects stock removal in EDM, 1972). This was followed by a model using a two-dimensional heat flow model bounded by an adiabatic finite cylinder (Van Dijck & Dutre, 1974). (DiBitonto, Eubank, Patel, & Barrufet, Theoretical models of the electrical discharge machining process II: The anode erosion model, 1989) used different sources for each electrode: a disk heat source for the anode and a point heat source for the cathode erosion. Another element of the boundary conditions is the plasma heat flux that can be defined as the following in the case of a uniform temperature distribution:

$$q = \begin{cases} \dfrac{F_c V_{gap} I_{peak}}{\pi r_c^2} & \text{disk source} \\ \dfrac{F_c V_{gap} I_{peak}}{2\pi r^2} & \text{point source} \end{cases} \tag{4}$$

where $F_c$ is the fraction of energy being transferred, $V_{gap}$ is the gap voltage applied to the electrodes, $I_{peak}$ is the peak current and $r_c$ is the plasma channel radius.

It has been observed that there is variation in the plasma radius. There is an expansion followed by stabilization. A common function describing the plasma channel radius, $r_c(t)$ as a function of time is given as follows (DiBitonto, Eubank, Patel, & Barrufet, Theoretical models of the electrical discharge machining process II: The anode erosion model, 1989):

$$r_c \;\; t \;\; = Kt^l \tag{5}$$

where $K$ and $l$ are coefficients depending on the machining parameters and material properties. Those values are determined empirically.

Concerning the plasma heat flux, some researchers have established that the temperature distribution in the plasma channel is not uniform and have adopted a Gaussian distribution as following (Kojima, Natsu, & Kunieda, 2007):

$$q \;\; r,t \;\; = \frac{F_c V_{gap} I_{peak} t_{on}}{2\pi r_c(t)} e^{-\frac{4.5r^2}{r_c^2(t)}} \tag{6}$$

where $F_c$ is the fraction of energy being transferred, $V_{gap}$ is the gap voltage applied to the electrodes, $I_{peak}$ is the peak current, $t_{on}$ is the time-on interval of the spark and $r_c$ is the plasma channel radius.

In order to provide a better understanding of the various elements that have been described, a model from Beck is presented here in more details (Beck, Transient temperatures in a semi-infinite cylinder heated by a disk heat source, 1981).

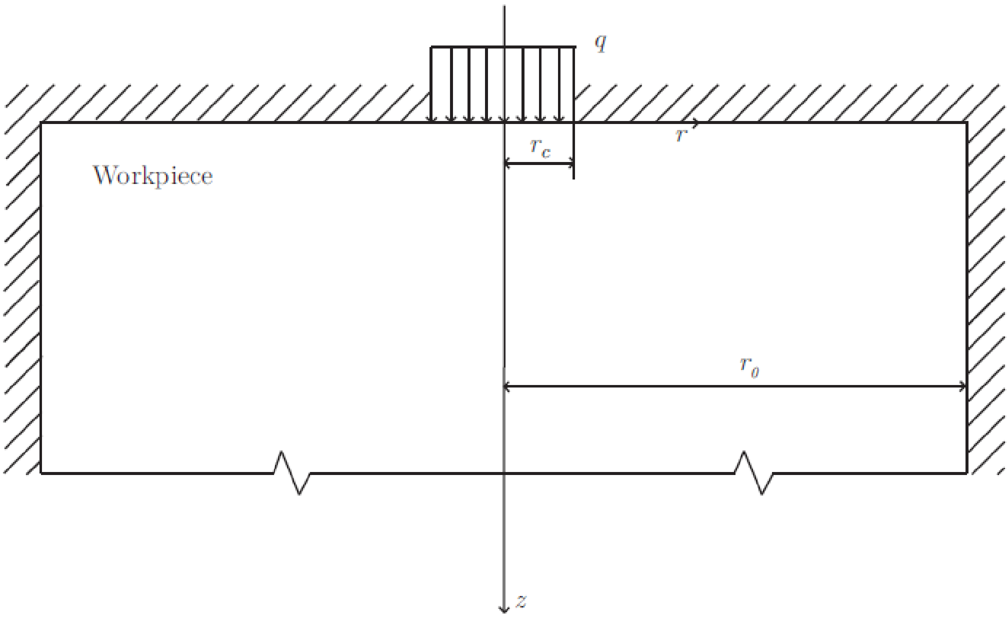

Figure 12: Parameterisation of Beck's model.

As visible on the parameterisation described on Figure 12, the heat source used is that of a disk. The geometry is a semi-infinite cylinder insulated (adiabatic) everywhere except for the region in contact with the heat flux. Solving Equation (1) yields the following solution for the temperature distribution.

$$T\ r,z,t\ = T_i + \frac{2qr_c}{K_t}\left\{\frac{r_c B\ z,t}{r_0^2} + \sum_{i=1}^{\infty}\frac{C_i\ z,t\ J_0\ \lambda_i r\ J_1\ \lambda_i r_c}{2[\lambda_i r_c J_0\ \lambda_i\ r_c\ ]^2}\right\} \tag{7}$$

where

$B\ z,t\ = \sqrt{\alpha t}\ ierfc(\frac{z}{2\sqrt{\alpha t}})$ and $C_i\ z,t\ = e^{-z\lambda_i}\left\{1 + \mathrm{erf}[\lambda_i\sqrt{\alpha t} - \frac{z}{2\sqrt{\alpha t}}]\right\}$

$J_n\ x$ is the Bessel function of the first kind and is defined as follows:

$$J_n\ x\ = \sum_{m=0}^{\infty}\frac{-1\ ^m}{m!\,\Gamma\ m+n+1}\left(\frac{x}{2}\right)^{2m+n} \tag{8}$$

Where $\Gamma(z)$ is the gamma function.

The $\lambda_i$ are determined as the solutions of $J_1\ \lambda_n r_0\ = 0$

The model developed by (DiBitonto, Eubank, Patel, & Barrufet, Theoretical models of the electrical discharge machining process I: A simple cathode erosion model, 1989) leads to the following temperature distribution:

$$T\ r\ = T_i + F_c\cdot\frac{V_{gap}I_{peak}}{2\pi K_t r_0}erfc(\frac{r_0}{2\sqrt{\alpha t}}) \tag{9}$$

The Beck and DiBitonto (for the cathode) models have been used with the parameters tabulated in Table 3. Those were chosen as parameters relevant to micro-EDM in the situation where aluminium is used. The use of steel is more common in micro-EDM but ultra-fine grain aluminium was being used at the time to study the influence of small grain size. The thermal models being designed without a specific material, they should be adapted to aluminium as well. The values for $r_0$ and $r_c$ were determined using the recommendations found in (Pandey & Jilani, 1986). It is noteworthy that Beck's model was not developed specifically to be applied in EDM but as a general mathematical application. As a result the notion of fraction of energy transferred to the electrode is absent. A value of 3.6% was chosen in line with previous findings (Shao & Rajurkar, 2013).

The use of those parameters in Equation (7) leads to the temperature distribution at $t=t_{on}$ shown in Figure 13.

Table 3: Input parameters used for the evaluation of Beck's model.

| **Input** | **Description** | **Value** |
|---|---|---|
| $K_t$ | Thermal conductivity [J/s m K] | 220 |
| $\rho$ | Material density [Kg/m$^3$] | 2700 |
| $C_p$ | Specific heat [J/KgK] | 910 |
| $T_i$ | Initial Temperature [K] | 293 |
| $T_b$ | Boiling Temperature[K] | 2792 |
| $\alpha$ | Thermal diffusivity [m$^2$/s] | 8.95 10$^{-5}$ |
| $r_0$ | Radius of the insulated surface of the workpiece [m] = 50R$_c$ | 0.0041 |
| $r_c$ | Heat source radius at the cathode surface [m] | 8.23 10$^{-5}$ |

| | | |
|---|---|---|
| $F_c$ | Percentage of energy absorbed by the tool [%] | 3.6 |
| $t_{on}$ | Spark duration [µs] | 5 |

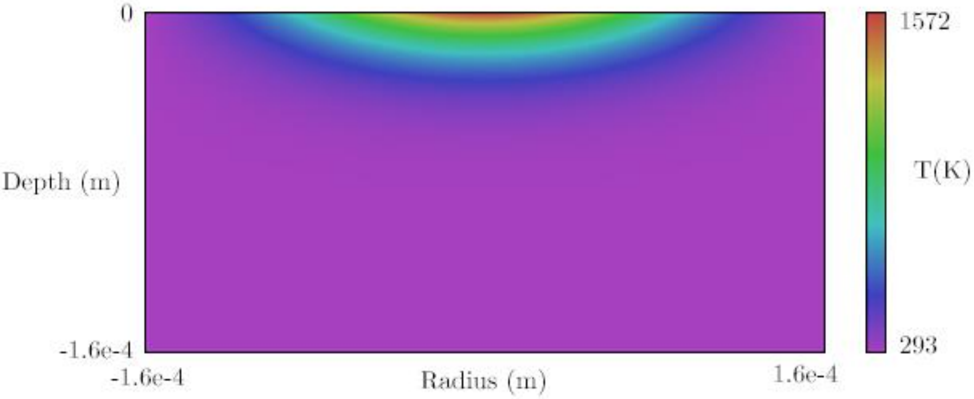

Figure 13: Temperature distribution obtained with Beck's model.

When used with Equation (9), this leads to this other temperature distribution also at $t=t_{on}$ (Figure 14).

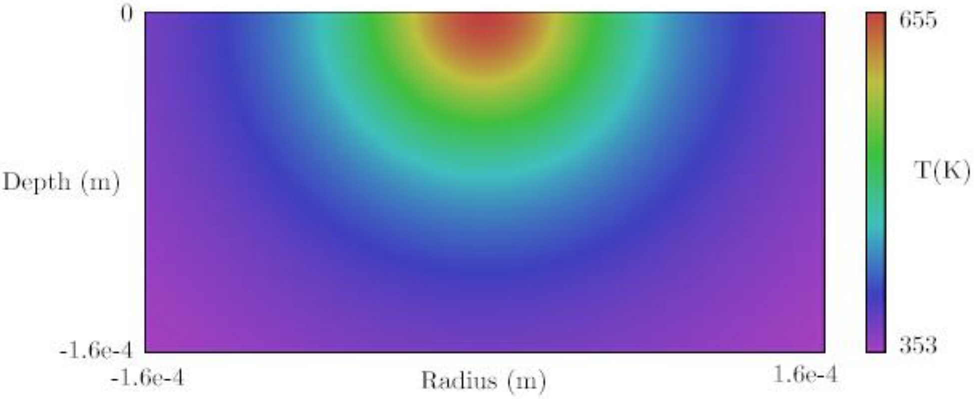

Figure 14: Temperature distribution obtained with DiBitonto's model.

In general, models for EDM applied to micro-EDM tend to significantly underestimate the temperature distribution at any time in the electrode. In Beck's case, the predicted temperature does not reach a value sufficient for the melting, and even less so, the vaporizing of the material. This is also the case to a greater extent in DiBitonto's model. As a result, the applicability of EDM models to the micro-scale isn't viable. Possible reasons for this situation could be attributed to the change in scale that leads to other phenomenon being preponderant.

#### 2.7.2.3. Electro-mechanical modelling

An electro-mechanical model for EDM is adequate in the case of short spark duration as the material supposedly isn't sufficiently exposed in order to heat which is the case in micro-EDM. In (Singh & Ghosh, 1999) researchers have proposed such a model exploiting the stress induced by electrostatic forces. This model is based on the assumption that the plasma region is electrically neutral as the positive ion density is nearly equal to the electron density. The potential difference can't be accommodated in this neutral region creating a thin sheath near the cathode where there is a charge imbalance and where the potential gradient is formed. The presence of such a sheath creates a strong electrical field at the cathode that induces a negative charge. This surface charge is pulled outwards by the field resulting in stress. The research concludes with the observation that at low duration pulses, the crater depth is independent from the spark duration.

### *2.7.3 Simulations*

#### 2.7.3.1. Introduction

This section will focus on the notion of simulation in EDM and micro-EDM with an emphasis on die-sinking micro-EDM. Simulations applied to other variants of micro-EDM will be studied as well in the cases where the ideas presented are deemed to be relevant with the present research.

The typical simulation concept lies in representing the geometry of tool and workpiece, using various techniques such as cellular automata or finite element (FE) models, and in deriving from the gap separating these two elements the most probable discharge location. Consequently, removal or craters on both the electrode and the workpiece can be assessed based on the single spark modelling approach considered and the geometrical models modified accordingly.

#### 2.7.3.2. Numerical simulations

In (Das, Klotz, & Klocke, 2003) the authors used a commercial FEM software called DEFORM to simulate several aspects of the process, while limiting themselves to a single spark discharge. The aim of the authors was to make a prediction of several aspect of the process: the material removal phenomenon, the heat affected microstructure and the residual stress induced in the workpiece during the machining. Using the heat equation, the fraction of energy absorbed by the workpiece, the values of the current and voltage and the plasma characteristics, the model developed with DEFORM FEM simulator was able to predict the thermal characteristics and the residual stresses of the workpiece. For this purpose, the material phase transformation from solid to liquid and vapour was taken into account, and the same was done for the physical characteristics of the workpiece material, which were considered temperature dependent. In this model the residual stresses were supposed to be caused by the temperature gradients which resulted in expansions and contractions of the material due to the thermal cycles of the process. Regarding the crater shape, the authors referred to assumptions from the literature: the central depression of the crater is simulated in the model as well as the protruding edges for which an additional pressure boundary condition was needed. The model was finally validated comparing the simulated results with the experimental ones. The main stress involved in this process resulted to be the compressive one: the material, because of the temperature, tended to expand and this expansion was limited by the surrounding colder material. This resulted in a compression stress. On the contrary, when the material was cooling down, it tended to pull the surrounding cold material and this resulted in a tensile stress in the workpiece. Concerning the temperature distribution, the residual stresses and the crater shape the model outputs were considered accurate and the model was considered suitable for the simulation of the multi-spark discharge process.

The aim of the researchers in (Yang, Guo, Chen, & Kunieda, 2011) was mainly to overtake the limitation of the thermal models about crater formation and to analyse from a molecular point of view, the removal mechanism in the micro-EDM process and to simulate the crater formation mechanism. For this purpose an approach called Molecular Dynamics was applied: this kind of approach is useful in order to consider, at the same time, the thermal and the mechanical behaviour of the discrete parts of the workpiece.

In this model, the workpiece is assumed to be composed of a finite number of discrete elements. The model is made of three domains: cathode, anode and gap;

boundary conditions were imposed considering for example the thickness of the boundary atoms composing the workpiece and the surface involving the sparks.

Concerning the heat source, it was supposed to be circular and the heat income was simulated for the velocity of each atom basing on the Maxwell-Boltzmann distribution. The heat transfer phenomenon was considered as well as the interatomic force between the atoms. The material removal mechanism explained in this model relies on the formation of bubbles of vaporized material; these bubbles are located in a small space between cathode and anode. Those bubbles explode because of the pressure and remove the molten material on the surface in the form of clusters.

Finally, the influence of the electrode surface finish on the crater formation was investigated: the presence of pores on the electrode surface resulted in a worse surface of the workpiece and in a bigger diameter of the craters, which leads to a general worse roughness of the workpiece.

In (Izquierdo, Sanchez, Plaza, & Ortega, 2009) the authors developed a finite elements model aimed at describing and predicting the temperature fields generated by multiple discharges on the workpiece during the process. The model resulted in it being able to simulate and also represent the resulting surfaces. In this case, the describing equation considered the most suitable for the EDM process is a thermal one, with heat transmission coming from the spark. The solution of the thermal problem leads to the temperature distribution inside the workpiece from which it is possible to estimate the shape of the craters. In this paper, the workpiece is discretized by hexahedral elements (cubes) and for each element appropriate boundaries are defined. For each volume an energy balance is carried out considering the losses of energy due for example to the convection. Basically, the energy flux is supposed to pass through each volume across certain faces of the volume element. The modelling of the heat source consisted in the definition of a spark in which the voltage and the current are supposed to be constant during the process. Moreover, the quantity of energy lost is also considered constant. Finally, the dependency of the plasma radius on time had been determined, using previous literature to set the exponent. Once the temperature distribution had been found, the criterion for the estimation of the crater volume was set: every part of the workpiece which reached a temperature higher than $T_{eq}$ was supposed to be removed from the workpiece. Another aspect considered in the paper relates to the spark location, which is influenced by the local gap and by the debris distribution. Differently from other works, the influence of multiple discharges instead of single discharges is considered.

#### 2.7.3.3. Geometrical simulations

Those models are called geometrical in the sense that the physics behind the apparition of craters aren't considered. Only purely geometrical elements of the crater such as their dimensions and/or volumes are taken into account. The use of a purely geometrical solutions makes any simulation faster than with the use of finite-element methods involving numerous solving of complex equations. Therefore the ideas presented here tackle with the complete simulation of an entire micro-EDM process.

The first attempt at geometrical simulation of the die-sinking EDM process was in (Tricarico, Delpretti, & Dauw, 1988). The geometries are described by a set of points that describes the surfaces of the tool and the workpiece and are displaced during the simulation process.

This was a two-dimensional simulation method that was extended to simple three-dimensional shape through rotation of the profiles or swept surfaces.

This was followed by work from (Kunieda, Kowaguchi, & Takita, Reverse simulation of die-sinking EDM, 1999) on die-sinking micro-EDM in which the geometries were modelled by three dimensional meshes. The notion of reverse simulation was also introduced which consisted, after having performed a classic simulation, in inverting the volume removal parameters between the tool and the workpiece. Once this done, the workpiece was fed towards the tool and, at the end of the process, the electrodes returned to their original shape. The amount and distribution of material removed from the workpiece during the reverse simulation gave an indication of the volume to be added to the tool in order to compensate for tool wear during the process. An improvement of this method (Kunieda, Kaneko, & Natsu, Reverse simulation of sinking EDM applicable to large curvatures, 2012) was made in order to apply it to electrodes with large curvatures.

The machining gap isn't taken into account in this method. The material removal is done through the use of the notion of tool wear ratio but isn't a crater-by-crater method. Instead, large rectangular chunks of material are removed.

The three-dimensional geometric simulation of micro-EDM milling processes was performed by (Heo, Jeong, Min, & Lee, 2009). The tool and the workpiece were modelled as Z-maps which present an inherent limitation since they can't represent overhangs.

The use of Z-maps was also implemented in the case of die-sinking micro-EDM by (Zhao, Zhang, Liu, & Yamazaki, 2004). Once again, the use of Z-maps is a limitation that prevents the representation of overhangs. All the sparks that occur are vertical. The authors considered the machining gap through the use of tables meant for wire-EDM.

## 2.8. Proposed work

Considering the previous work that has been undertaken by various researchers, there is progress to be made in the field of tool wear compensation in die-sinking micro-EDM. Previous work has been undertaken in that field with some success.

It is unwise to implement a fully physics-based simulation process when potentially hundreds of thousands of iterations could be required. Therefore, should a complete and fast tool be developed, a geometrical approach should be preferred. While it might be possible that a lack of accuracy might arise when compared with physical models, the gains in terms of computation times would counterbalance this. Furthermore, the complexity and interactions of the physics behind micro-EDM make it unlikely that a single model would be able to accurately model the process.

However all the proposed geometrical methods have their drawbacks. The most common is the nature of the geometrical models used for the representation of the electrodes. All of them use a discretisation of the surfaces at the boundaries of the electrodes either Z-maps or a common discrete mesh. The main limitation of Z-maps has been discussed previously. In the case of usual meshes, they are prone to possible self-intersection which would be a major issue during a simulation.

Additionally, the meshes would need to be refined regularly as the surfaces are deformed to accommodate the presence of new craters.

The current state is a preference towards micro-EDM milling because of the tool wear issue. However, should that problem be solved for die-sinking micro-EDM, the optimized process could prove to be faster and able to machine larger areas with micro-features. In addition, it would be possible to obtain complex 3D cavities with an excellent surface finish. The idea behind the present research is that die-sinking micro EDM could become a cost effective and potentially more accurate alternative to micro EDM milling for complex three dimensional shapes provided that one could model accurately the wear effect on the electrode and the resulting shape modification. Deformation could then be compensated for when designing the electrodes by adding extra volume to the electrode in key locations and therefore reducing the number of electrodes required to achieve the targeted profile.

The inclusion of the issue linked to the flushing of the debris isn't considered here since it is supposed that the problem is too complex to be solved in a fast and meaningful way.

The first step is to build a tool able to accurately and quickly predict the location and intensity of tool wear during a micro-EDM process. Considering the fact that the various thermal models available aren't adaptedwhen applied to micro-EDM, a geometrical solution is to be preferred. Additionally, taking into account the great number of sparks that occur during a complete micro-

EDM process, geometrical methods are well adapted due to their low computational requirements as opposed to finite element methods.

A three-dimensional approach is to be considered since a two-dimensional method does not take into account the influence of craters that do not appear in the same plane.

The second step consists in the development of models issued from experimental data used to train machine learning algorithms. Those models will be used to determine the input parameters for the simulation of unknown cases.

The third step is to use the output provided by the simulation tool inside an iterative loop that will seek to minimize the difference between the desired workpiece and the actual result achieved.

Finally, it is proposed as a fourth step to use the data provided by the optimisation loop to train a neural network that will be able to predict optimal tool shapes from target profiles that haven't been simulated and optimized.

In order to better understand the different elements, Figure 15 presents the project in its entirety. The three different parts are highlighted. Part 1 is in blue, part 2 is in salmon, part 3 is in yellow and part 4 is in purple.

The remainder of the present document is articulated around these four parts.

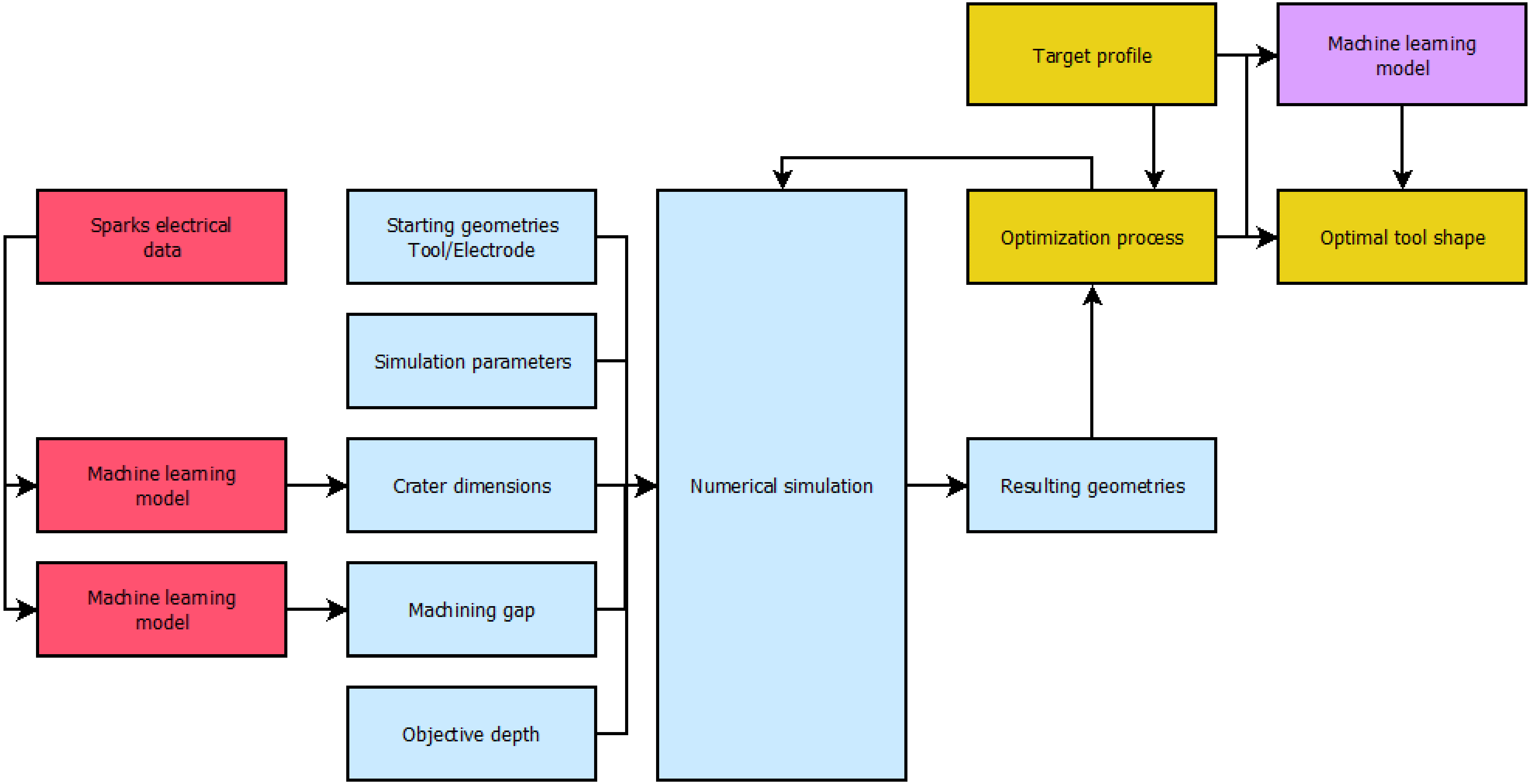

Figure 15: Overview of the proposed work.

# Chapter 3

# A geometrical material removal tool

## 3.1. Introduction

As previously mentioned, one of the main issues that arises during the micro-EDM die-sinking manufacturing process is the tool wear. It is of note that the case considered here is restricted to micro-EDM die-sinking in dielectric oil. The alternative use of deionized water results in Electro-Chemical Machining effects (Campana & Miyazawa, 1999). The present chapter presents two main solutions that have been explored for the numerical simulation of micro-EDM in order to better understand and predict the tool wear phenomenon. The first of those is based on the use of Non-Uniform Rational B-Splines (NURBS) as support geometries for the modelling of the tool and the workpiece while the second uses voxels embedded in an octree data structure to represent the electrodes.

A certain number of solutions were available when considering the models of the electrode. Previous work has focused on the use of z-maps, three-dimensional meshes or two-dimensional cell decomposition. All those methods have their drawbacks whether in terms of representation ability (z-maps can't represent overhangs) or memory usage and general accuracy (any spatial enumeration model). This fact has led to the exploration of alternative solutions for the geometrical representation of the electrodes. NURBS have been chosen for their ability to represent smooth surfaces that present no discontinuity and this characteristic could possibly improve the simulation's accuracy. However several drawbacks that appeared led to the consideration of a second solutions based on voxels embedded in octrees. The voxels method, a purely volumetric solution, has been preferred over other representations such as dexels since the sampling quality for those can be very low for surfaces with normal vectors nearly perpendicular to the sampling direction (Ren, Zhu, & Lee, 2008). It is proposed to address the main issue of voxels, memory usage, through the use of octrees as a containing tree structure.

Both of the solutions have been developed using C#.NET as the main programming language. Visualization was implemented using a C# DirectX wrapper (SharpDX).

Before going into the details of the simulation itself, the first few sections will give some basic insight on the various mathematical notions relevant to NURBS as well as voxels.

The main concepts of the simulation tool will then be described before going into the details of the implementations using NURBS and voxels.

## 3.2. Non-Uniform rational B-Splines

### *3.2.1. Overview*

Since the inception of three dimensional models and supercomputers, the description of complex shapes has been a main problematic. This increasing need has led to the creation of Bezier curves and surfaces in 1962.

However Bezier curves can't exactly describe some specific shapes such as circles. This has led to the development of other mathematical tools including Non-Uniform Rational B-Splines.

In order to ease the comprehension of key elements described in further sections, an overview of the mathematical concepts that NURBS rely upon is provided. A complete and exhaustive presentation is available in (Piegl & Tiller, 1997).

### *3.2.2. B-Spline Basis functions*

Before formally defining NURBS, it is necessary to start with the notion of B-splines basis functions and B-splines. There are several ways to define those basis functions. Considering that the mains cope of our work is to be implemented numerically, a recurrence formula attributed to de Boor, Cox and Manfield (Piegl & Tiller, 1997) is used. A B-Spline basis function is defined over what is known as a knot vector which is a set of non-decreasing values:

$$\mathbf{U} = \{u_0, \dots, u_n\} \; where \; u_i < u_{i+1} \quad for \; i \in [0, \dots, n+p+1] \tag{10}$$

Where $p$ is the polynomial degree of the B-Spline basis function and n is the number of basis functions. The $u_i$ are known as knots. The i<sup>th</sup> B-spline basis function of degree 0 is defined over the parametric domain $u$ as follows:

$$N_{i,0}\ u \ = \begin{cases} 1 \; if \; u_i \leq u < u_{i+1} \\ \quad 0 \text{ otherwise} \end{cases} \tag{11}$$

The i<sup>th</sup> B-Spline basis function of degree p is defined as follows:

$$N_{i,p}\ u\ = \frac{u-u_i}{u_{i+p}-u_i}.N_{i,p-1}\ u\ + \frac{u_{i+p+1}-u}{u_{i+p+1}-u_{i+1}}.N_{i+1,p-1}(u) \qquad (12)$$

It is of note that, in some cases, the quotient 0 over 0 can appear. In that case convention dictates that a value of 0 be attributed to that quotient.

B-Spline basis functions verify the following properties:

Partition of unity : $\sum_{i=0}^{m} N_{i,p}\ u\ = 1$ (P1)

Non-negativity : $\forall\ \ u, i\ , N_{i,p}\ u\ \geq 0$ (P2)

Local support : $\forall u \notin [u_i, u_{i+p+1}],\ N_{i,p}(u) = 0$ (P3)

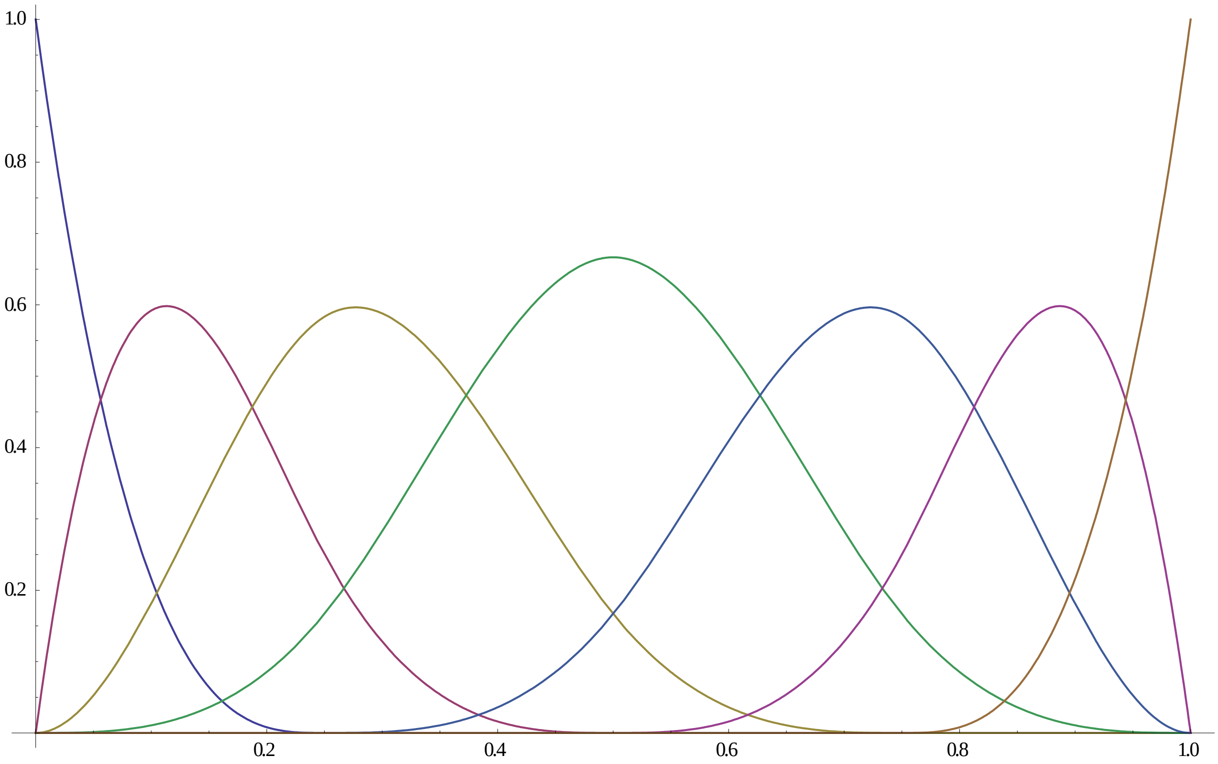

Figure 16: B-Spline basis function over the knot vector {0, 0, 0, 0, 0.25, 0.5, 0.75, 1, 1, 1, 1}.

Figure 16 represents the seven B-Spline basis functions over the knot vector {0,0,0,0,0.25,0.5,0.75,1,1,1,1}. The first and last knots are with multiplicity four meaning that they are repeated four times which indicates that these are the basis functions of degree three. This way of representing knot vectors with the first and last knot vector with multiplicity p+1 is called clamped as opposed to unclamped. In the remainder of this document, all knot vectors will be given in the clamped format.

### *3.2.3. NURBS curves*

A NURBS curve of degree p (or of order p+1) is formally defined as follows:

$$\mathbf{C}_p\ u\ = \frac{\sum_{i=0}^{n} N_{i,p}\ u\ .w_i.\mathbf{P}_i}{\sum_{i=0}^{n} N_{i,p}\ u\ .w_i}\ \text{for}\ \ 0 \le u \le 1 \tag{13}$$

$\{\boldsymbol{P}_i\}$ is the set of control points, $\{w_i\}$ is the set of weights (associated with each control point) and $\{N_{i,p}(u)\}$ is the set of B-Spline basis functions of degree p defined over the knot vector:

$$\mathbf{U} = \{\underbrace{0,\dots,0}_{p+1}, u_{p+1}, \dots, u_{m-p-1}, \underbrace{1,\dots,1}_{p+1}\} \tag{14}$$

All NURBS curve satisfy the relation: $p + 1 = m - n$.

It can be convenient to express $\mathbf{C}_p\ u$ in a different way to outline the fact that each point of the curve is computed as the sum of weighted control points as follows:

$$\mathbf{C}_p\ u\ = \sum_{i=0}^{n} R_{i,p}\ u\ .\mathbf{P}_i \quad \mathit{where}\ R_{i,p}\ u\ = \frac{N_{i,p}.w_i}{\sum_{j=0}^{n} N_{j,p}.w_j} \tag{15}$$

### *3.2.4. NURBS surfaces*

A NURBS surface of degree p in direction u and of degree q in direction v can be defined in the form of:

$$\mathbf{S}_{\mathrm{p,q}}\ u,v\ = \frac{\sum_{i=0}^{n}\sum_{j=0}^{m} N_{i,p}\ u\ N_{j,q}\ v\ w_{i,j}\mathbf{P}_{i,j}}{\sum_{i=0}^{n}\sum_{j=0}^{m} N_{i,p}\ u\ N_{j,q}\ v\ w_{i,j}} \tag{16}$$

$\{\boldsymbol{P}_{i,j}\}$ is the set of control points, $\{w_{i,j}\}$ is the set of weights (associated to each control point) and $\{N_{i,p}(u)\}$ and $\{N_{j,q}(v)\}$ are the set of B-Spline basis functions of degree p and q respectively defined over the following knot vectors:

$$\mathbf{U} = \{\underbrace{0,\dots,0}_{p+1}, u_{p+1},\dots,u_{r-p-1},\underbrace{1,\dots,1}_{p+1}\} \tag{17}$$

$$\mathbf{V} = \{\underbrace{0,\dots,0}_{q+1}, u_{p+1},\dots,u_{s-q-1},\underbrace{1,\dots,1}_{q+1}\} \tag{18}$$

with $r = n + p = 1$ and $s = m + q + 1$

Similarly to Equation (15), $\mathbf{S}(u,v)$ can be written as:

$$\mathbf{S}\ u,v\ = \sum_{i=0}^{n}\sum_{j=0}^{m} R_{i,j}\ u,v\ \mathbf{P}_{i,j} \tag{19}$$

with:

$$R_{i,j}\ u, v\ = \frac{N_{i,p}\ u\ N_{j,q}\ v\ w_{i,j}}{\sum_{k=0}^{n}\sum_{l=0}^{m} N_{k,p}\ u\ N_{l,q}\ v\ w_{k,j}} \tag{20}$$

The main properties of NURBS surfaces are:

Partition of unity : $\forall\ (u,v)\ \in [0,1]^2\ \sum_{i=0}^{n}\sum_{j=0}^{m} R_{i,j}(u,v) = 1$ (P1)

Non-negativity : $\forall\ (u,v,i,j)\ , R_{i,j}(u,v) \geq 0$ (P2)

Local support : $\forall u \notin \left[u_i, u_{i+p+1}\right] \times \left[v_j, v_{j+q+1}\right],\ R_{i,j}(u,v) = 0$ (P3)

## 3.3. Voxels and octrees

### *3.3.1. Voxels*

Voxel stands short for volumetric pixel and, as the name implies, is often described as the three dimensional equivalent of pixels. (Kaufman, Cohen, & Yagel, 1993) In the field of solid modelling, the technique that consists in representing a volume with voxels is known as spatial occupancy enumeration. The solid is typically described as the list of voxels it occupies. In addition to defining the occupancy of a solid, additional values can be affected to each voxel to describe other properties of the solid such as the colour, density, material and others of its real properties.

The source of the data that is used to build volumetric representations is usually sampled from real objects (Computed Tomography, Magnetic Resonance Imaging), issued from simulation (fluid dynamics simulations, meteorology) or existing three dimensional models.

The increase in computer memory has made the use of voxels more attractive as memory usage is its main disadvantage. A volume described by $1024^3$ voxels (more than a billion voxels) would occupy more than a Gigabyte of memory. The same trend was observed in the mid-seventies when raster graphics replaced vector graphics as memory capacity of computers increased.

However, regardless of the resolution used to describe a volumetric object, there will always be an inherent loss of information when using a discrete solution such as voxels. Computations of volumes and distances will be limited to the precision permitted by the voxels' size which is unacceptable when an exact measurement is required. If an exact value isn't required, the approximated computations will however be significantly easier to compute than with surface models.

### *3.3.2. Octrees*

#### 3.3.2.1. Overview

An octree is a hierarchical data structure in which each node (also known as a cell) can have up to eight children. This data structure is most often used to subdivide a three dimensional space into eight octants in a recursive manner. An illustration of an octree can be observed in Figure 17 and its associated tree representation is given in Figure 18.

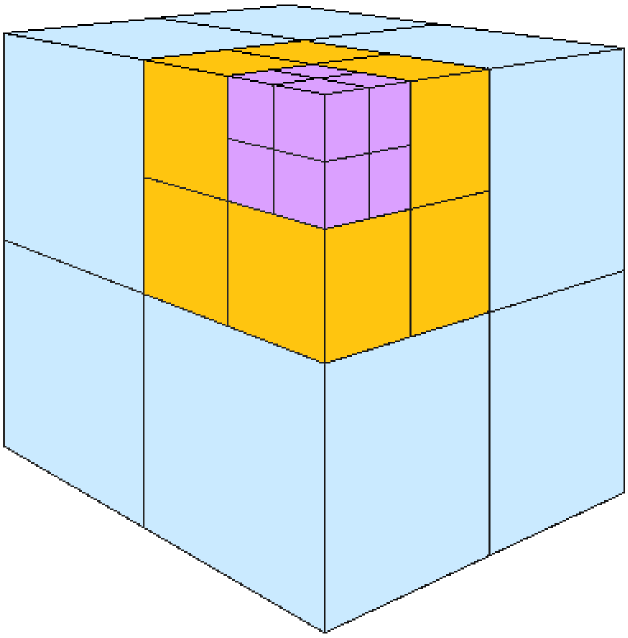

Figure 17: The visual representation of an octree.

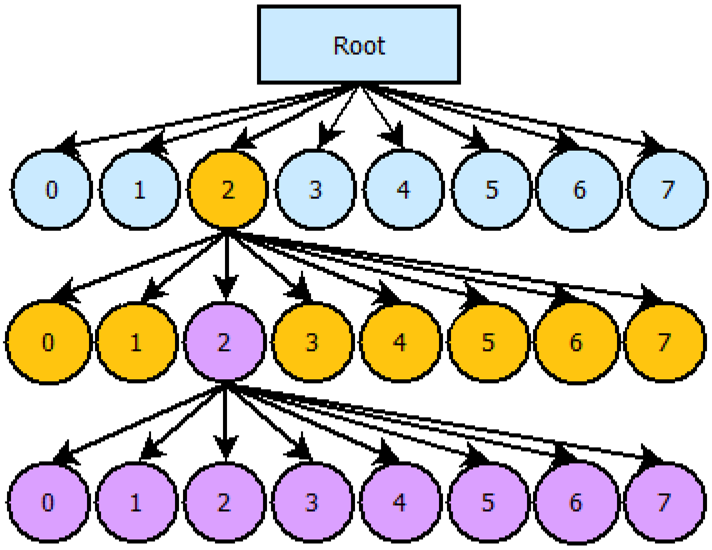

Figure 18: An octree hierarchical structure

Octrees are particularly well adapted to represent a spatial occupancy enumeration into regular hexahedra. They provide with the possibility of condensing large areas of no interest (mostly large sections of Boolean volume data) and therefore reducing memory usage. It is of note that in the case of non-

Boolean volume data (when additional material properties are specified for example), condensation is harder to achieve efficiently.

### 3.3.2.2. Representations

Programmatically speaking, octrees can be defined in various manners (Knoll, 2006), each with their advantages and disadvantages. Two main layouts exist when it comes to implementing octrees. The first is a pointer-based octree that is mostly used when memory consumption isn't deemed an issue and the octree needs to be modified frequently. The second, an index-based octree, is used in the opposite scenario.

In both cases, a node element will always contain a pointer to its children. Additionally, the node will probably contain information about its position either in the form of a $\mathbf{V}_{\mathbf{min}}$ and $\mathbf{V}_{\mathbf{max}}$ vector or a $\mathbf{V}_{\mathbf{center}}$ vector and the node's half-size. Not doing so would require computing each node's position from the root node each time it is required.

#### Full Octrees

A full octree could be considered as a regular three dimensional grid: all leaf nodes have the same size corresponding to a tree depth $t_d$ and the number of leaf nodes is:

$$N_{leavcs} = 8^{t_d} \tag{21}$$

A visual representation is given in Figure 19 in which an octree of dimension 1024 µm was subdivided until all leaf nodes were of a size of 128 µm.

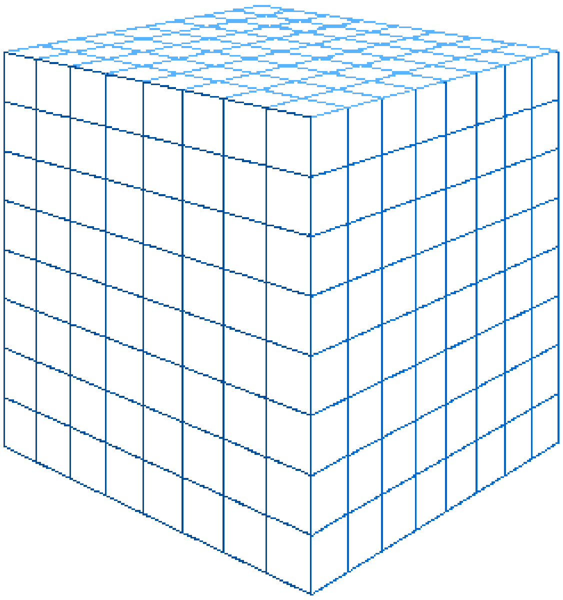

Figure 19: A full octree with a depth level of 3.

The advantage of a full octree lies mainly in its regularity. A node does not have to contain information about its position and merely pointers to its children. Alternatively all nodes can be store in a single array. This type of octree is used in the situation when the volume data is evenly distributed and takes most of the octree's volume. Should that not be the case (the described volume being very sparse), the memory gain in reduced information storage is quickly outstripped by the additional nodes used to describe large, empty sections.

### Pointer-based octrees

A pointer-based octree stores, for each node, a pointer to its children and, possibly, another one to its parent. The particularity lies in the fact that a node containing no children is considered as a leaf while, in the case of a node with more than one but less than eight children, those missing children are empty as seen in Figure 20.

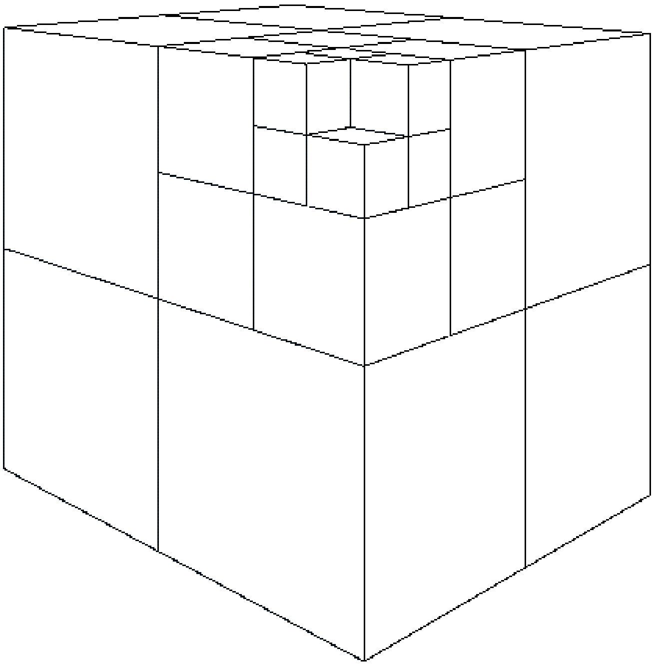

Figure 20: Pointer-based octree with an empty node.

A pointer-based octree can either have eight pointers (one for each children) or only one if the children are stored contiguously in memory. However storing only one pointer makes it impossible to allocate new children on-demand.

### Linear Octrees

The linear octree (Gargantini, 1982) layout consists in affecting to each leaf node a locational code which is a unique index. The locational code is built in such a manner that finding a specific node's parent or children is straightforward. The locational code of a node is based on its parent locational code and its position within it. A possible choice is displayed in Table 4.

Table 4: Octree child nodes locational codes.

| X | Y | Z | Binary locational code | Decimal code |
|---|---|---|---|---|
| - | - | + | 000 | 0 |
| + | - | + | 001 | 1 |
| - | - | - | 010 | 2 |
| + | - | - | 011 | 3 |
| - | + | + | 100 | 4 |
| + | + | + | 101 | 5 |
| - | + | - | 110 | 6 |
| + | + | - | 111 | 7 |

All the leaf nodes' locational codes are sorted in order in a single array.

(Glassner, 1984) proposed a few improvements. For one, the children were numbered between 1 and 8 instead of Gargantini's 0 to 7 since a computer can't make the difference between 00 and 0. Gargantini circumvented this limitation by adding a stop bit equal to 1 to the locational codes. In addition, Glassner proposed to store all eight children contiguously in order to speed up the search for a node. Finally, instead of being stored in a single sorted array, the nodes are found through the use of a hash map.

## 3.4. The simulation tool

### *3.4.1. Global overview*

Regardless of the method of representation, NURBS or voxels, the main principle of the simulation tool remains the same and can be described through Figure 21 while the input/output relationships of the main algorithms can be described through Figure 22 which is a more detailed version of Figure 15 limited to the numerical simulation tool.

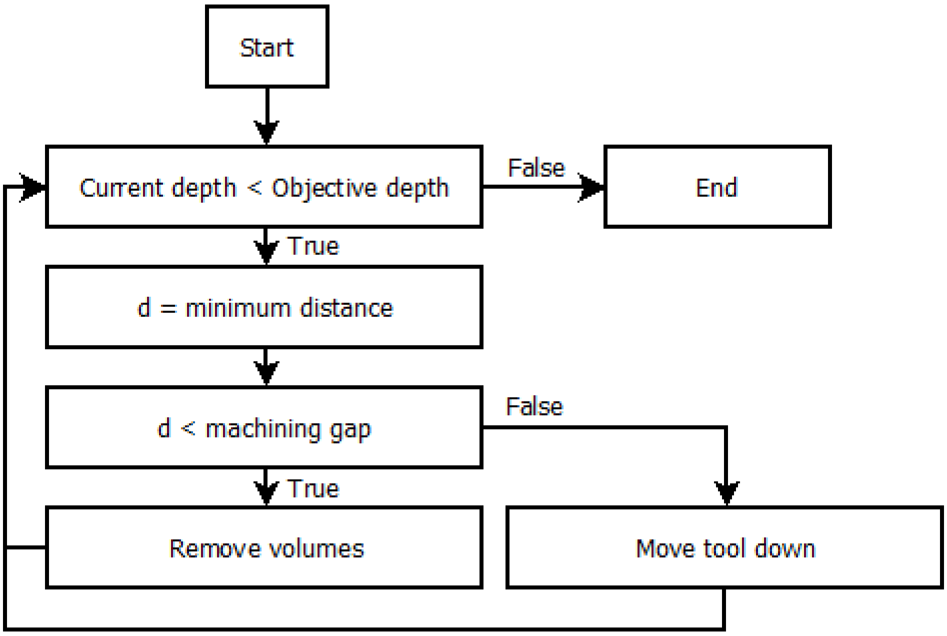

Figure 21: Main diagram of the simulation tool principle.

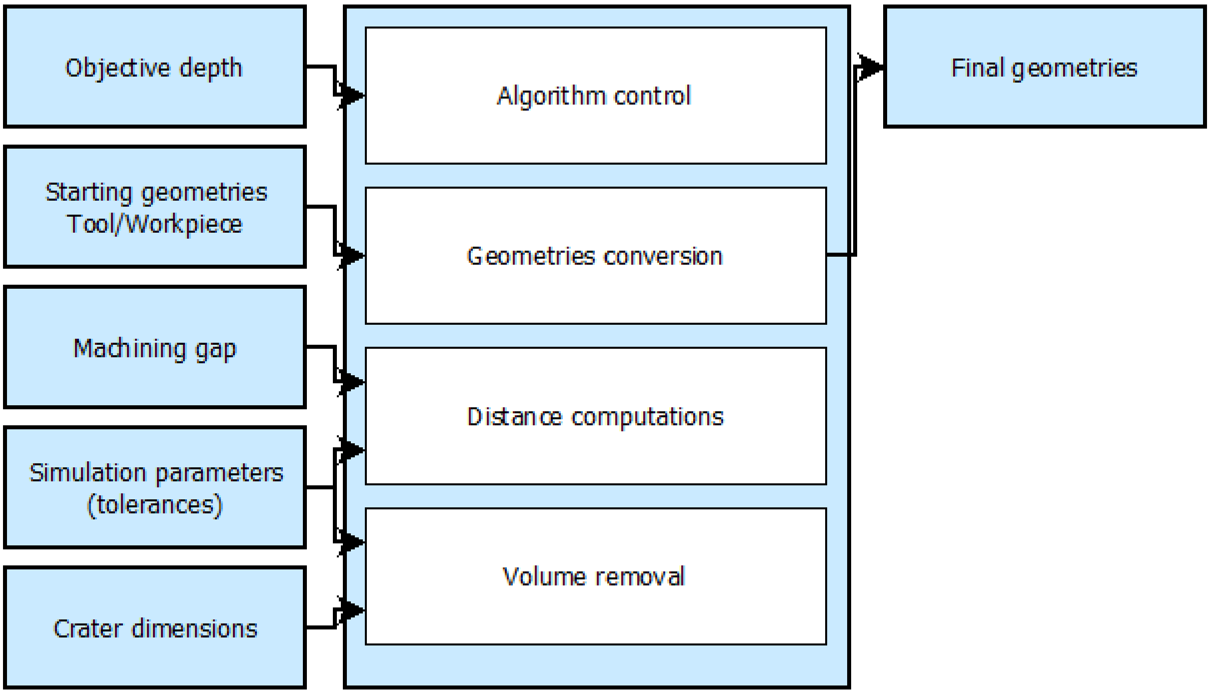

Figure 22: Input/output relationships of the main algorithms.

An iteration of the simulation starts with the comparison of the current depth to the objective depth. If the tool electrode has reached that objective depth, the simulation ends. If not, the smallest distance between both electrodes is found. Should that distance be smaller than the machining gap, material is removed from the geometries to mimic the shape of craters. If that distance is greater than the machining gap, the tool is moved down by a small increment.

A new iteration can then take place.

### *3.4.2. The simulation tool using NURBS*

#### 3.4.2.1. Introduction

In the proposed approach, both the geometry of the tool and the geometry of the workpiece are defined by means of NURBS patches.

To allow the insertion of thousands of craters, the surfaces of the tool $\mathbf{S}_t$ and workpiece $\mathbf{S}_w$ are heavily refined using the Boehm's knot insertion algorithm (Piegl & Tiller, 1997). It is of note that the whole patches are refined before starting the process in order to avoid having to do it after each iteration. As a result the surfaces' control points will be a lot closer to it, hence local control is significantly increased.

At each step of the insertion process the location of each crater (one on each electrode) is determined while identifying the shortest distance between the tool and the workpiece since it is considered that the electrical spark will happen on the less resistive path, i.e. the shortest one.

Minimum distance computations are done using an optimisation method known as particle swarm optimisation (PSO for short) which is a simple numerical optimizer that does not require the use of the gradient of the objective function (Kennedy & Eberhart, 1995). Alternative optimisation methods were applied to the distance computation with less success in terms of computing speed or accuracy (in this case the ability to find the global minimum and not a local one). Among those methods were the Nelder-Mead algorithm (Nelder & Mead, 1965), the differential evolution algorithm (Storn, 1996), the conjugate gradient method, the Newton method, the quasi-Newton method and the simulated annealing algorithm (Kirkpatrick, Gelatt, & Vecchi, 1983).

The minimum distance search parameters related to PSO were determined using meta-optimisation. The possibility of finding a local minimum instead of the global solution has been considered as acceptable provided that the deviation isn't too important. The risk is that repeatedly finding a local minimum instead of the optimal solution leads to the two geometries intersecting. To alleviate this, the algorithm checks regularly for intersection between the two NURBS surfaces. If an intersection is found, the tool is moved up. This situation has been observed as being extremely rare.

A crater is then inserted in each of those locations by moving the surrounding control points. As explained in the literature review, the shape of a crater can be assimilated to a part of sphere. The use of a purely geometrical method and the crater dimensions being input parameters makes it possible to include the re-solidification of melted material within the crater dimensions since those used are empirically determined.

If the computed minimum distance d exceeds the value of the minimum distance required for a spark to appear (known in EDM as the gap distance $M_g$) then the tool is moved down along the z axis with an increment of Δz. Otherwise, if the computed minimum distance is smaller than $M_g$ then the PSO algorithm returns four values $(u_t, v_t)$ and $(u_w, v_w)$ corresponding to the parametric coordinates of the craters' centres respectively on the tool (subscript *t*) and workpiece (subscript *w*). The algorithm then moves the control points located in the surrounding of the craters' centres so that two craters of volumes $V_t^r$ and $V_w^r$ are inserted into the tool and workpiece. The deformation technique is similar to surface warping considered as a geometric deformation technique (Piegl & Tiller, 1997). The process ends when the desired depth $D_g$ is met. The overall algorithm can be described in pseudo-code form as in figure 6. The different steps of the crater insertion process are further detailed in the next subsections.

#### 3.4.2.2. Volume enclosed by a NURBS patch.

In the proposed algorithm, it is mandatory to control the volume $V_e^r$ removed on the electrode *e* (with $e \in \{t,w\}$) at each iteration of the simulation process. To do so, the idea is to compute the difference between the initial volume $V_{e0}$ enclosed by the NURBS patch and the volume at a given iteration $V_e$. Generally speaking, the Green-Ostrogradsky's theorem states that for a vector field F and a region V enclosed by a surface S:

$$\int_V \text{div}\,\mathbf{F}\,d\mathrm{V} = \oint_S \boldsymbol{F}.\boldsymbol{d}\mathbf{S} \qquad (22)$$

In the proposed approach, the surface $\mathbf{S}_e$ to be deformed is defined by a single NURBS patch of degree $p_e$ in u and $q_e$ in v Figure 23a) and defined by its parametric Equation (23):

$$\begin{aligned}\mathbf{S}_{\mathrm{e}}\ u,v\ &= \frac{\sum_{i=0}^{n_e}\sum_{j=0}^{m_e} w_{ij} N_{ip}\ u\ N_{jq}\ v\ P_{ij}}{\sum_{i=0}^{n_e}\sum_{j=0}^{m_e} w_{ij} N_{ip}\ u\ N_{jq}\ v} \\ &= {}^{t}\,[x\ u,v\ ,y\ u,v\ ,z(u,v)]\end{aligned} \tag{23}$$

where $\mathbf{P}_{ij}$ represents one of the $(1 + n_e) \times (1 + m_e)$ control points to be moved, and $w_{\mathrm{ij}}$ the weights associated to each control points to be moved. The weights will be taken equal to 1 in the proposed approach and won't be considered as unknowns of the deformation process.

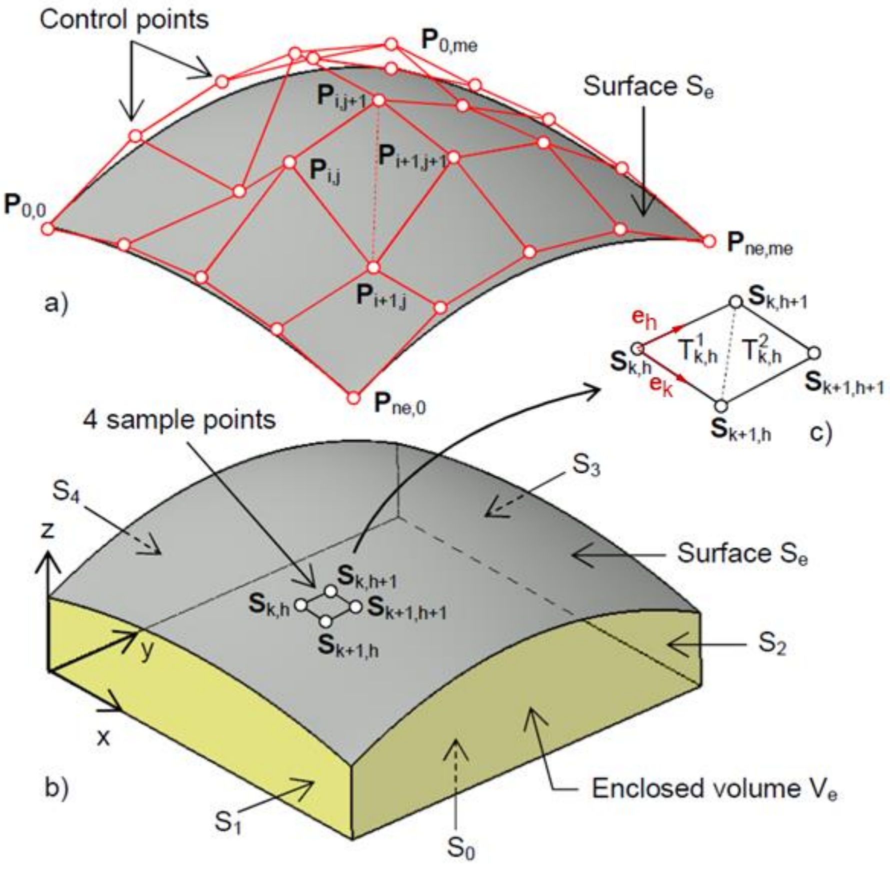

Figure 23: enclosed volume computation.

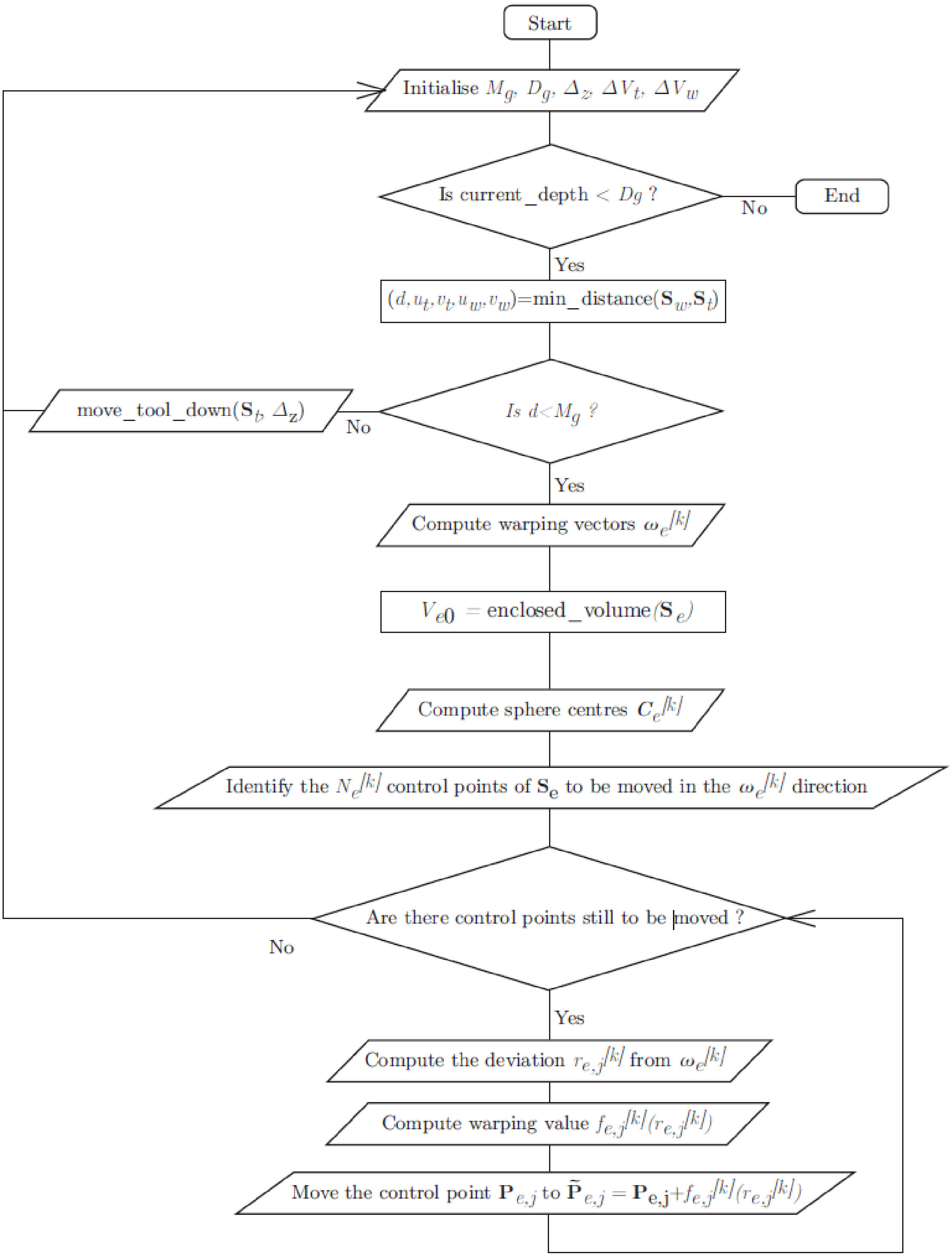

Figure 24: Simulation diagram for the NURBS solution.

The surface $\mathbf{S_e}$ not being a closed surface, the idea is to choose the field $\mathbf{F} = {}^t[0,0,z]$ so that:

$$\oint_S \mathbf{F}.\boldsymbol{d}\mathbf{S} = \int_{\mathbf{S_e}} \mathbf{F}.\boldsymbol{d}\mathbf{S_e} = \int_{\boldsymbol{U_e}} \mathbf{F}.\left(\frac{\partial \boldsymbol{S_e}}{\partial u} \times \frac{\partial \boldsymbol{S_e}}{\partial v}\right) dudv \tag{24}$$

where $U_e$ is the patch's parametric domain. The patch is not trimmed in the simulation tool. Thus the enclosed volume $V_e$ becomes (Figure 23.b):

$$V_e = \int_{U_e} z.\left(\frac{\partial x}{\partial u}\frac{\partial y}{\partial v} - \frac{\partial y}{\partial u}\frac{\partial x}{\partial v}\right) \tag{25}$$

It can then be approximated while discretizing the parametric space $U_e$ with $(N_e^u \times N_e^v)$ sample points. Thus, for a given sample point $\mathbf{S}_{k,h} = \mathbf{S}_e(u_k, v_h)$, and a neighbourhood $[u_k,u_{k+1}]\times[v_h,v_{h+1}]$, the surface $\mathbf{S}_e$ can be approximated locally by a quadrangle which can be decomposed in two triangles $T^1_{k,h}$ and $T^2_{k,h}$ and the enclosed volume becomes (Figure 23.c):

$$V_e = \sum_{k=1}^{N_e^u-1} \sum_{h=1}^{N_e^v-1} \left[V_e(T^1_{k,h} + T^2_{k,h})\right] \tag{26}$$

where the volume $V_e(T^1_{k,h})$ enclosed by $T^1_{k,h}$ can be computed using Equation (25) and a simple parameterization of the triangle:

$$V_e(T^1_{k,h}) = \frac{1}{6}(e^x_k e^y_h - e^y_k e^x_h)(s^z_{k,h} + s^z_{k+1,h} + s^z_{k,h+1}) \tag{27}$$

Here, x, y and z stand for the coordinates of the vectors represented on Figure 23.c. A similar formula applies for the triangle $T^2_{k,h}$.

Table 5: Comparison of speed and accuracy for the sampling-based method.

| **Nb. Points** | **Time (ms)** | **$V_w$ (µm$^3$)** | **$D_b$ (%)** | **$D_f$ (%)** |
|---|---|---|---|---|
| 25 | 24 | 283329 | 15.66 | 100 |
| 50 | 97 | 360872 | 7.42 | 24.74 |
| 100 | 379 | 344769 | 2.63 | 6.33 |
| 200 | 1508 | 334685 | 0.38 | 1.59 |
| 400 | 3397 | 336873 | 0.27 | 0.70 |
| 800 | 24652 | 335950 | 0.00 | 0.09 |

In order to be able to tune the discretization parameters $N_w^u$ and $N_w^v$, several samplings have been performed on a final surface $\mathbf{S}_w$ and the results are reported in Table 5. In this table, $D_b$ is the ratio to the best estimation, and $D_f$ the ratio to the fastest estimation. As expected, doubling the number of sample points in each direction leads to four times more sample points over the entire surface, hence the total computation time is also greater by a factor of four. Overall, it is noticed that acceptable results (those that would be within 5% of the true value of the volume) would require computational time of several hundreds of milliseconds.

Table 6: Comparison between sampling-based (800 points in each direction) and control points-based (1000 points in u and v) methods.

| **Method** | **Time (ms)** | **$V_w$ (µm$^3$)** | **$D_b$ (%)** | **$D_f$ (%)** |
|---|---|---|---|---|
| Sampling | 3397 | 335950 | 100 | 1.79 |
| Control points | 61 | 335137 | 0.24 | 100 |

Even if the simulation tool doesn't need to sample the whole surface but just the portion being deformed, it is still interesting to explore other strategies. An alternative would be to consider that the control points are sufficiently close to the real shape to be used in an accurate calculation of the surface's enclosed volume. In this case, formulas similar to Equations (26) and (27) can be obtained directly from the control points and not from the sampling points anymore (Figure 23.a). A comparison between the sampling-based and control points-based methods is presented in Table 6. From those results, it is clear that the control points-based method is much faster than the sampling approach without, however, significantly reducing the quality of the approximation. Thus, this method has been adopted since the computation of the enclosed volume will be performed hundreds of thousands of times during the µEDM simulation.

### 3.4.2.3. Volume to be removed for each crater

Each electrical spark transfers a certain amount of energy to the tool, the workpiece and the dielectric fluid. Here, it is considered that the amount of energy brought to each element is the same at each spark. Previous research (Wang, Ferraris, Galbiati, Qian, & Reynaerts, 2013) suggests that the energy distribution at low energy levels is uniform. However, this isn't the case at higher levels and could be accounted for in the future. As such, it is desirable to remove the same volumes $V_t^r$ and $V_w^r$ when simulating the insertion of all the craters. These volumes are experimentally obtained by measuring the mean radius $\overline{R_e}$ and mean depth $\overline{D_e}$ of actual craters. Then, considering that the craters are domes, the volumes to be removed $V_e^r$ are computed using the following formula:

$$V_e^r = \frac{\pi \overline{D}_e}{6}\left(3\overline{R}_e^2 + \overline{D}_e^2\right), \qquad e \epsilon \{t, w\} \tag{28}$$

From these volumes and domes, the support spheres can be identified, i.e. the spheres of radii $\mathrm{R_e}$ equal to the dome's radius. As explained, these two radii remain constant for the two surfaces for the crater-by-crater simulation.

#### 3.4.2.4. Craters insertion

Following the flowchart of Figure 24, for a given depth of the tool, if the minimum distance is smaller than the gap distance, the craters insertion process starts. Craters are inserted one by one on each surface $\mathbf{S}_\mathrm{e}$ ($e \in \{t,w\}$) and centred on $\mathbf{S}_\mathrm{e}(u_e,v_e)$. For sake of clarity, the superscript $[k]$ has not been put on the parametric coordinates $u_e$ and $v_e$ even if these values refer to the $k^{\mathrm{th}}$ craters (one on each surface). First, to identify the displacement directions, the two warping unit vectors are computed as follows:

$$\omega_e^{[k]} = sg\ e\ \frac{\mathbf{S}_\mathrm{t}\ u_t, v_t\ \ - \mathbf{S}_w\ u_w, v_w}{\|\mathbf{S}_\mathrm{t}\ u_t, v_t\ \ - \mathbf{S}_w\ u_w, v_w\ \|} \text{ with } sg\ e\ = \begin{cases} 1 \text{ for } e = t \\ -1 \text{ for } e = w \end{cases} \tag{29}$$

Figure 25 represents a two-dimensional version of the process after having found the minimum distance. For sake of clarity, solely the part of the workpiece is represented even if the same strategy applies to the tool. The next step consists in identifying which control points need to be moved in the surrounding of the two points $\mathbf{S}_e(u_e,v_e)$.

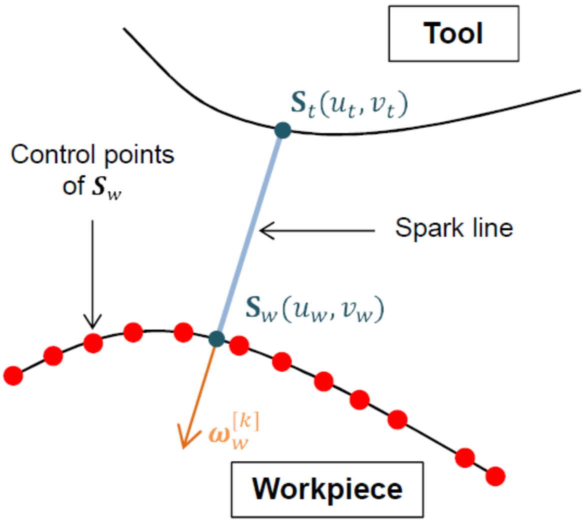

Figure 25: Definition of the warping vector $\omega_w^{[k]}$ for a crater to appear on the workpiece.

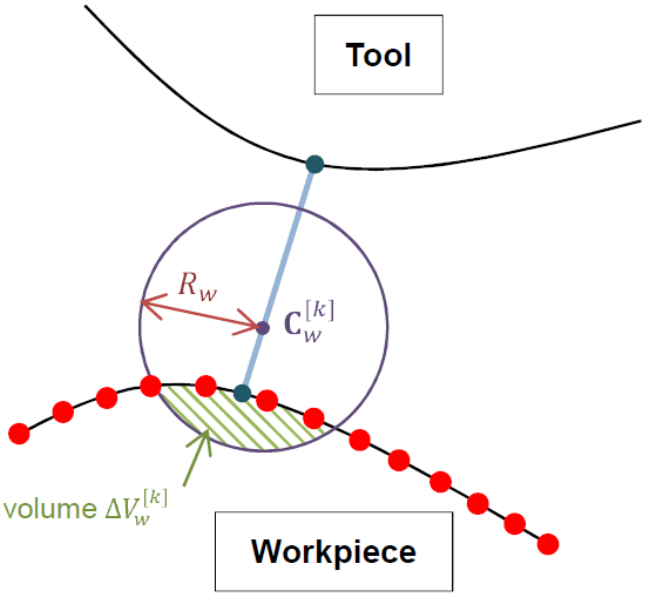

Figure 26: Definition of the support sphere and removed volume ΔVw.

Once the radii of the two spheres identified, the location of the spheres' centres has to be computed (one for the tool and one for the workpiece). As illustrated on Figure 26, the centre of the sphere lies on the spark line. Its exact position depends on the volume $V_e^r$ that needs to be removed. In order to find the location, an iterative dichotomy method (also known as binary search or bisection method) is used. At each step, the surface $\mathbf{S}_\mathbf{e}$ is deformed and the intersecting volume (the hashed part of Figure 26) between the sphere and the surface is computed while using the previously introduced formula ($\Delta V_e^{[k]} = V_e^{[k]} - V_{e0}^{[k]}$). If the volume obtained is smaller than $V_e^r$, the sphere is moved towards the surface, and if it is bigger it is moved away from it. The process carries on until the obtained volume $\Delta V_e^{[k]}$ falls within a specific tolerance $\mathrm{T_v}$. Once the $C_e^{[k]}$ adequate positions are found, it is possible to determine the $N_e^{[k]}$ control points of the two surfaces that need to be moved. This is done by computing for each control point the distance that separates them from the centre of the sphere. If the distance is smaller than the radius of the sphere, the control point is added to the list of points to be displaced. At the end, two lists of control points are obtained.

In order to displace the control points to mimic the shape of a sphere, a reference is needed. Let $\Pi_e^{[k]}$ be the plane that includes the centre of the sphere $\mathbf{C}_e^{[k]}$ and that has $\boldsymbol{\omega}_e^{[k]}$ as normal vector.

Then, the new position of all the control points $\mathbf{P}_{e,j}^{[k]}$ to be moved (e ∈ {t,w} and $j \in \{1 \dots N_e^{[k]}\}$) are computed as follows (Figure 27):

$$\mathbf{P}_{e,j}^{[k]} = \mathbf{P}_{e,j}^{[k]} + f_{e,j}^{[k]}\left(r_{e,j}^{[k]}\right).\,\boldsymbol{\omega}_e^{[k]} \tag{30}$$

with $f_{e,j}^{[k]}\left(r_{e,j}^{[k]}\right) = \sqrt{R_e^2 - r_{e,j}^{[k]2}} - \left[\mathbf{P}_{e,j}^{[k]} - \pi_{e,j}^{[k]}\right].\boldsymbol{\omega}_e^{[k]}$

and $r_{e,j}^{[k]} = \left\|\pi_{e,j}^{[k]} - \mathbf{C}_\mathrm{e}^{[k]}\right\|$,

where $\pi_{e,j}^{[k]}$ is the projection of $\mathbf{P}_{e,j}^{[k]}$ on the plane $\Pi_e^{[k]}$. In this formulation, a unique index j has been used to identify the $\mathrm{j^{th}}$ control point $\mathbf{P}_{e,j}^{[k]}$ to be moved to generate the $\mathrm{k^{th}}$ crater.

This process is repeated iteratively until no more craters can be inserted for the actual depth. Then, the tool is moved down along the z axis with an increment of $\Delta_z$ and the craters insertion process starts again (Figure 24).

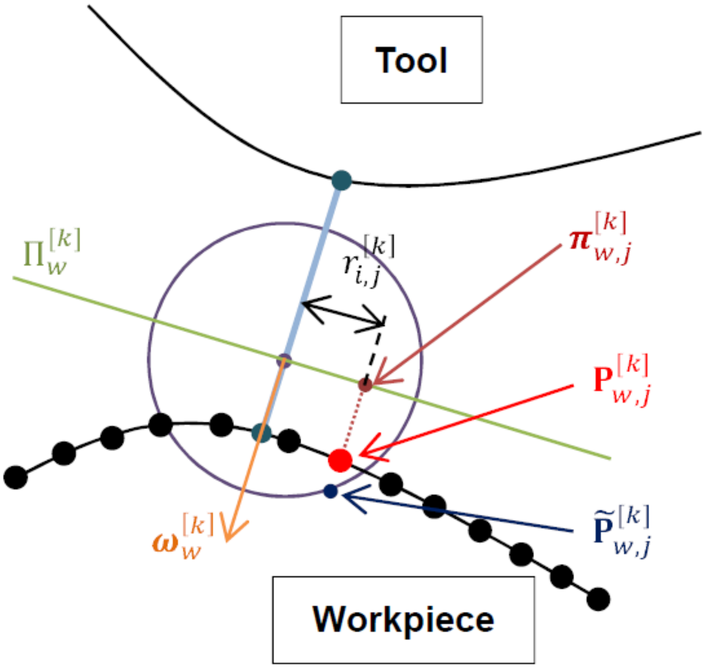

Figure 27: Plane $\Pi_w^{[k]}$ definition and a control point's projection.

### *3.4.3. The simulation tool using voxels*

#### 3.4.3.1. Overview

While the general process can be considered to be exactly the same, the Voxels-based method is opposed to the NURBS one in the sense that it is a truly volumetric approach. This change in the nature itself of the geometrical models lead to a change in the various algorithms and methods that have been implemented for the NURBS solution. Those new algorithms take advantage of the hierarchical nature of octrees in order to speed up the discharge simulation. The two main relevant algorithms are further detailed in the following sections.

#### 3.4.3.2. Minimum distance search

This section deals with the search of the minimal distance between two disjoint octrees. In addition, both of those are axis-aligned. The presented method is based on (Borrman, Schraufstetter, van Treeck, & Rank, 2007) with the addition of some fast exit conditions.

The smallest distance $d$ between two octree nodes can be bounded by two values such as:

$$d_{lower} \leq d \ \leq d_{upper} \tag{31}$$

In the situation where both nodes are leaves (they don't contain any children), Equation (31) becomes:

$$d_{lower} = d = d_{upper} \tag{32}$$

Additionally, in the case where one node is a leaf but the other isn't, the calculation of the maximum distance between them can be modified to take that fact into account and further refine the value of $d_{upper}$.

The search algorithm starts with the two octrees root nodes and, for each non-empty children, compares the minimum and maximum distance of each voxel couple. Those distances are easy to compute since the nodes are axis-aligned.

Node pairs that are still viable candidates for the minimum distance couple are kept and subdivided at the next iteration.

The viability condition is based on a global value, the smallest of upper bounds or supremum $d_{supremum}$. Any couple that has a lower bound distance equal or smaller to that value is kept regardless of the minimum distance. The viability condition is formally written as:

$$d_{lower} \leq d_{supremum} \tag{33}$$

The process goes on until the voxels have been subdivided to a size $s_{res}$, a parameter of the algorithm. Since the algorithm relies on a bounding of the minimal distance, there is no guarantee that, after the number of iterations required to reach $s_{res}$, only a single couple is returned.

Additionally if all couples of candidate nodes are leaves, then, given the way the candidate nodes are culled, it stand to reason that all of those couples have the same $d$. At this stage, the algorithm may be terminated and a pair of nodes can be selected at random without having reached a resolution of $s_{res}$. This is especially useful when the two geometries are flat and parallel.

Two other early stop conditions can be added specifically for the present problem: in this case it doesn't matter whether the smallest distance is found.

Firstly, the returned result must only comply with the condition that it is smaller than the machining gap. If at any iteration of the search, a couple with a $d_{upper} \leq M_g$ than the algorithm can be stopped and that couple returned. A couple with an actually lower $d$ that has been ignored in that way will be used in another iteration of the simulation.

Secondly, if at any iteration of the search, the list of candidate couples doesn't contain any couple with a $d_{lower} \leq M_g$, the process can be stopped and return null. Another matter needs to be handled. Since the algorithm might return a list of couples that aren't necessary leaves (in the case where the algorithm exits after having reached a certain number of iterations), a couple is chosen at random. The algorithm is then re-applied on the selected couple and forced to exit after having found only leaf nodes. Using a Particle Swarm Optimisation Method has been tested but has been found to give worse results.

#### 3.3.3.3. Crater insertion

Once the closest nodes have been identified, the crater insertion method on an octree starts with the root node. The children are tested for intersection with a sphere defined in the same way as with the NURBS method: the support sphere is displaced along the spark line until a tolerance condition on the volume to be removed is met. More specifically, the process uses a root-finding algorithm known as Brent's method. It is a combination of the bisection method, the secant method as well as inverse quadratic interpolation.

Similarly to the distance algorithm, the volume removal algorithm searches the octrees in a top-down manner keeping only nodes that intersect with the sphere and deleting those that are inside. The intersection test is made by finding the smallest distance d between a cube and a point and comparing it to $R_i^2$. The intersection test returns true if:

$$d \leq {R_i}^2 \tag{34}$$

Once again, similarly to NURBS, the use of a purely geometrical method relying on the crater dimensions makes it possible to take into account the melted material re-solidification phenomenon.

#### 3.4.3.4. Voxelisation

An algorithm of interest is the one used for the conversion of .STL (STereoLithography) files into sparse voxel octrees. This is used at the initialization of the simulation method when importing a geometry to be used as the tool. The method implemented and adapted from, sparse solid voxelisation, can be found in details in (Schwarz & Seidel, 2010). Contrary to other voxelisation methods such as 6-separating surface voxelisation, triangle-parallel conservative voxelisation or direct triangle-parallel solid voxelisation, it has the advantage of not determining the state of each single voxel. Those methods proceed to voxelise the three-dimensional mesh through the actual voxelisation before embedding those into an octree. As a result, the memory usage is quite significant.

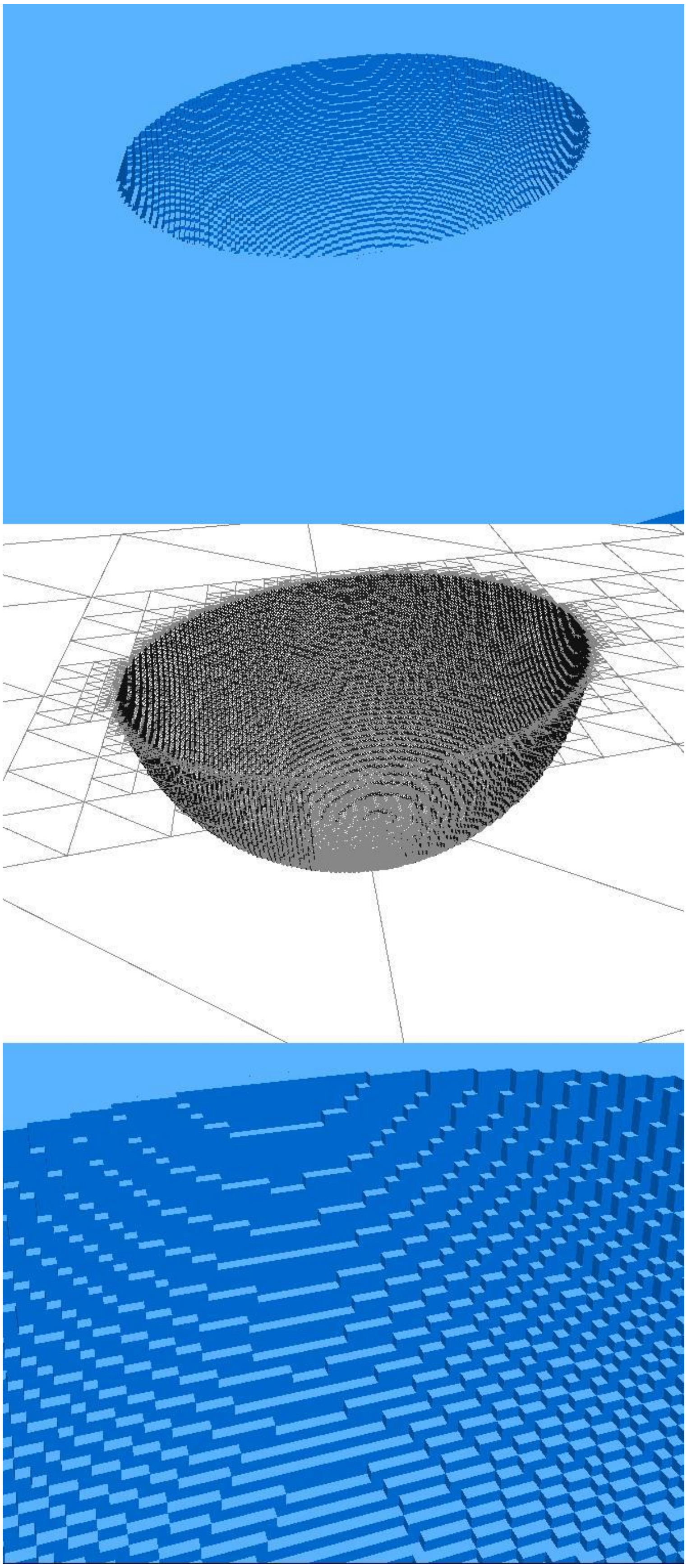

Figure 28: Single crater at a resolution of one voxel per 125 nm. From top to bottom: global view, wireframe view underlining the octree structure, detail of the crater's voxels.

The sparse solid voxelisation proposes to perform the voxelisation process directly into the octree structure. The construction of the octree in the present work differs slightly from (Schwarz & Seidel, 2010) since the octree type used differs but the spirit remains the same.

The first step consists in finding the bounds of the STL file in order to determine the bounding cube that will serve as the root of the voxel model. This is achieved through the search of the minimum and maximum values for each of the vertexes in the three main directions: X, Y and Z.

In the second step, all the triangles of the three-dimensional mesh are classified among the eight octants of the octree's root node. To do so, a triangle-cube intersection test is made between the triangle and each octant. Note that a triangle can be classified into several octants should it intersect with more than one. Each octant that contains at least one triangle is subdivided and is affected eight children.

The previous process is repeated with each octants and the triangles it contains until the octree has reached a set depth level.

The next step consists in deleting all the nodes that are outside of the model and keeping only those on the boundaries or inside the model. The model is based on a propagation process that is depicted in Figure 29.

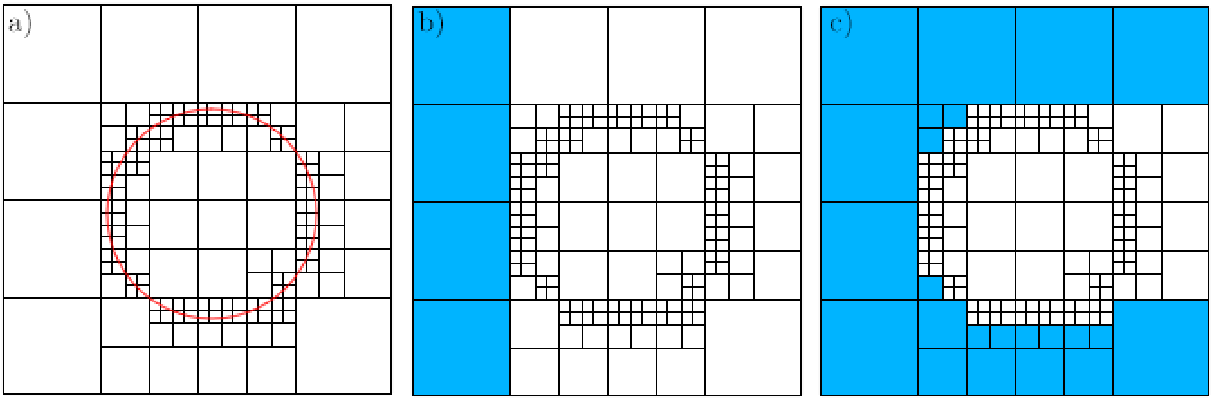

Figure 29: Two-dimensional representation of the voxelisation process.

The process starts by finding all the leaf nodes that don't have a neighbour in the X- direction (Figure 29b) and that have a size greater than the smallest nodes in the octree (the nodes at the boundary of the circle in Figure 29a). The algorithm then searches for all the neighbours of those initial nodes in the X+ direction until the next neighbour is either nothing or a node with the smallest size in the octree. All the nodes in blue are marked for deletion. The process is repeated starting from the nodes that don't have a neighbour in the X+ direction and propagating towards the X- direction to get the missing nodes.

Concave shapes are also handled. Once the algorithm has reached a boundary node, it will start considering that successive larger nodes are inside the volume and not mark them for deletion. Once it reaches another boundary node, the algorithm resumes the marking of larger nodes for deletion. An example of voxelisation is shown in Figure 30.

Figure 30: Voxelized version of the Stanford library model known as Lucy.

## 3.5. Experimental validation

### *3.5.1. Overview*

In order to assess the performances of each method, an experiment was devised in order to measure the shape differences between simulated and experimental results. The used machining parameters are displayed in Table 7.

The experiments were conducted using a Sarix SX-200 micro-EDM machine. Figure 31 shows the machine used and its main components.

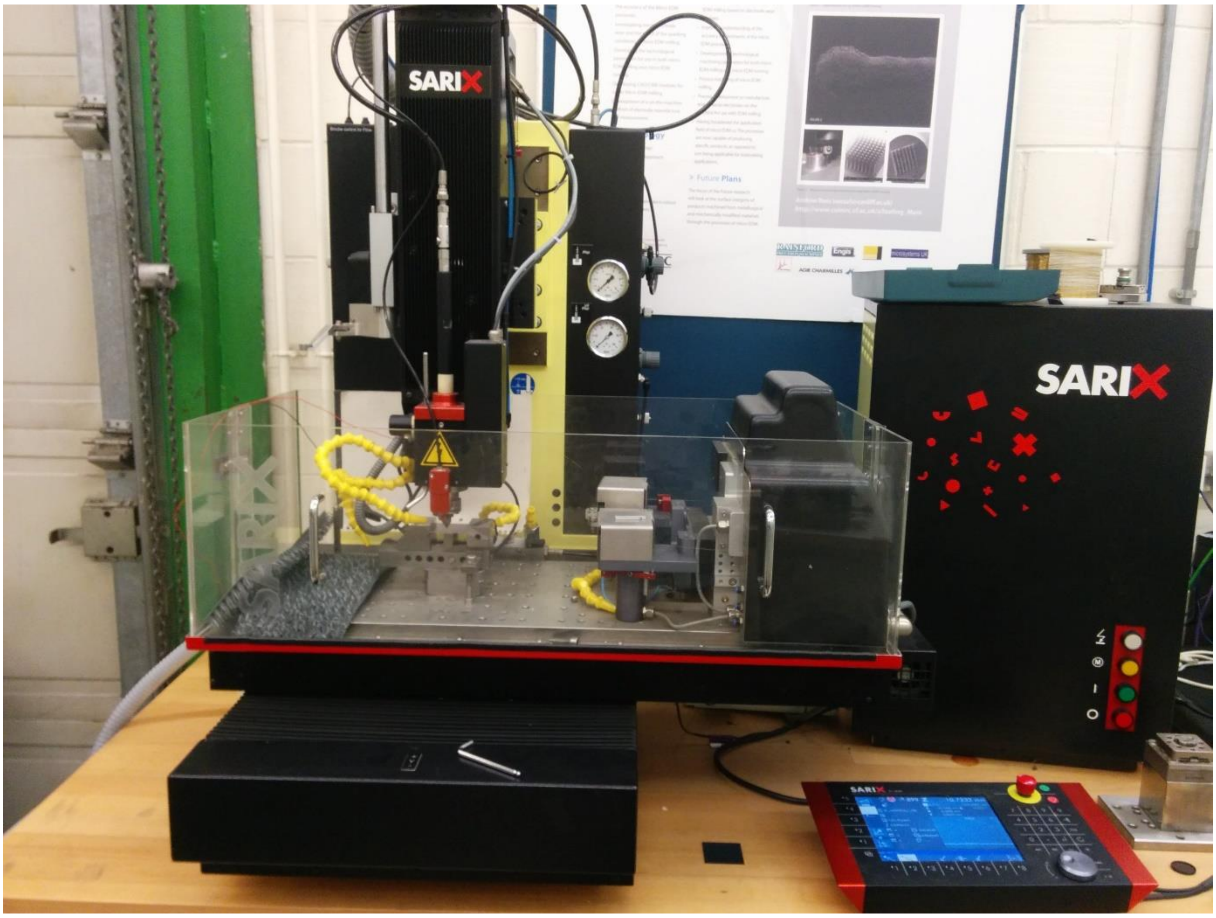

Figure 31: The SARIX SX-200 machine used in the experimental campaigns.

At the core of the machine is the generator that is at the origin of the sparks. The spindle holds the various electrodes. Depending on the type of electrodes used, it can act as a mechanical pencil and automatically feed the electrode. The Ariane unit (a small wire-EDM unit) is used to cut and dress electrodes into various shapes.

The Sarix SX-200 micro-EDM machine was mainly designed for micro-EDM milling. However it can also be used for drilling and die-sinking EDM.

The tools were made of tungsten carbide while aluminium was used for the workpiece. A depth of 100 µm is set for the machining operation. This depth was selected in order to provide a noticeable wear on the tool without completely destroying the features on it.

The tool that was used is of a spherical shape as visible in Figure 32(a) and has been obtained through wire-dressing of a cylindrical electrode of nominal diameter 300 µm. The Ariane wire-dressing unit was used for this operation. The nominal diameter of the sphere obtained is 250 µm.

This tool was measured with the help of a micro-tomographer of a resolution of 1µm (Santini & Guilizzoni, 3D X-ray micro computed tomography on multiphase drop interfaces: From biomimetic to functional applications, 2014) (Santini, Guilizzoni, & Fest-Santini, X-ray computed microtomography for drop shape analysis and contact angle measurement, 2013). The resulting workpiece was exported as a three-dimensional mesh. (Figure 32(c)) The tool was also measured in the same manner after the experiment (Figure 32(b)).

The machining parameters used are given in Table 7.

Table 7: Used machining parameters.

| **Parameter** | **Value** |
|---|---|
| Energy level (index) | 200 |
| Gap voltage (V) | 90 |
| Current (index) | 20 |
| Time on (ms) | 5 |
| Objective depth (µm) | 100 |

The craters were also measured using the 3D meshes and the results are tabulated in Table 8.

Table 8: Experimental average craters dimensions.

| Parameter | Value |
|---|---|
| Workpiece crater diameter (µm) | 13.30 |
| Workpiece crater depth (µm) | 4.42 |
| Tool crater diameter (µm) | 12.40 |
| Tool crater depth (µm) | 4.39 |

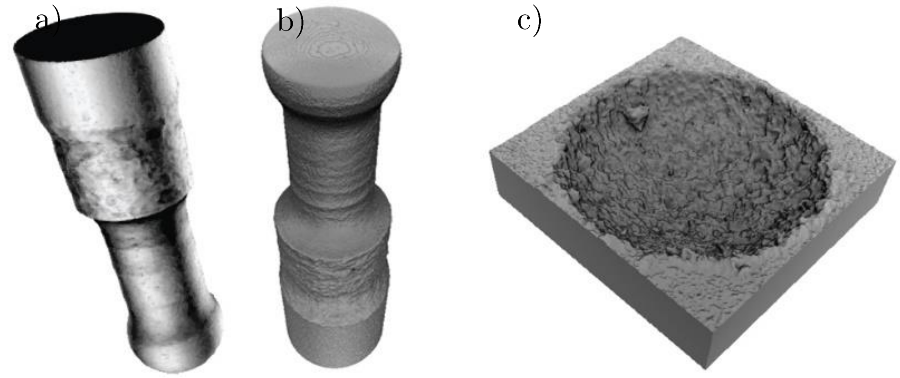

Figure 32: 3-D mesh of the experimental tool. a) before and b) after machining. c) workpiece after machining.

### *3.5.2. The simulations*

The NURBS elements used were a sphere of diameter 250 µm for the tool and a flat square surface with a side length of 500 µm for the workpiece as shown in Figure 32(a).

The voxel tool was created from the micro-tomographer STL files as shown in Figure 32(b) through a process known as voxelisation. The workpiece is a cube of dimension 512 µm. Contrary to what is depicted in the figure, only the tip of the spherical shape was kept in order to reduce the octree's memory footprint. Those two models do represent the same extremity of the tool using a sphere-like shape. The various tolerances used are tabulated in Table 9.

Table 9: Tolerances used in the simulations.

| **Parameter** | **Value** |
|---|---|
| NURBS volume removal (in %) | 1 |
| Voxel volume removal (in %) | 1 |
| Voxel crater resolution (voxels per micron) | 4 |
| Voxel distance precision (µm) | 0.25 |

The NURBS simulation ended after 2040 minutes while the voxels simulation took 126 minutes and is therefore more than 16 times faster. Both simulations were performed on the same desktop computer, an Intel Core i5 4670K at 4.5 GHz with 8 GB of RAM. Figure 34 and Figure 35 display some of the resulting geometries after simulation.

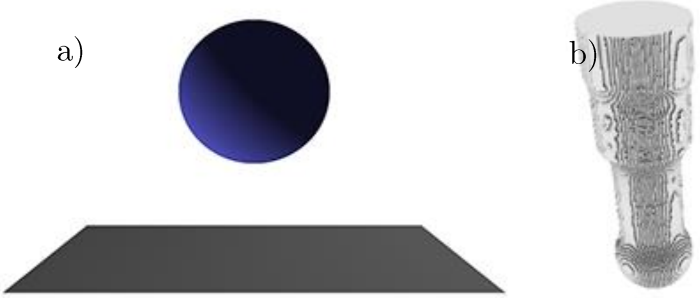

Figure 33: a) NURBS models of the sphere-like tool and the workpiece b) Voxel model of the tool.

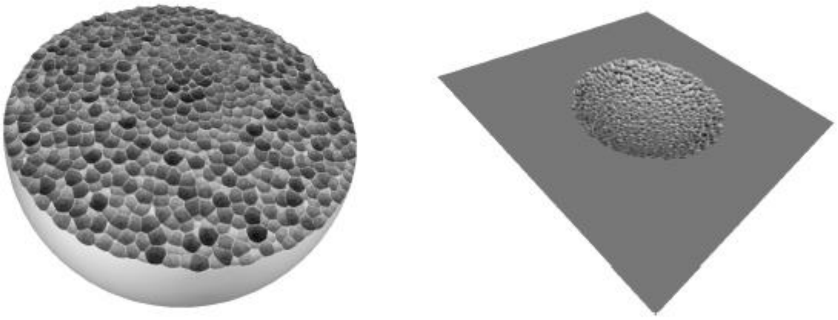

Figure 34: the NURBS surfaces after the simulation of the tool (left) and the workpiece (right).

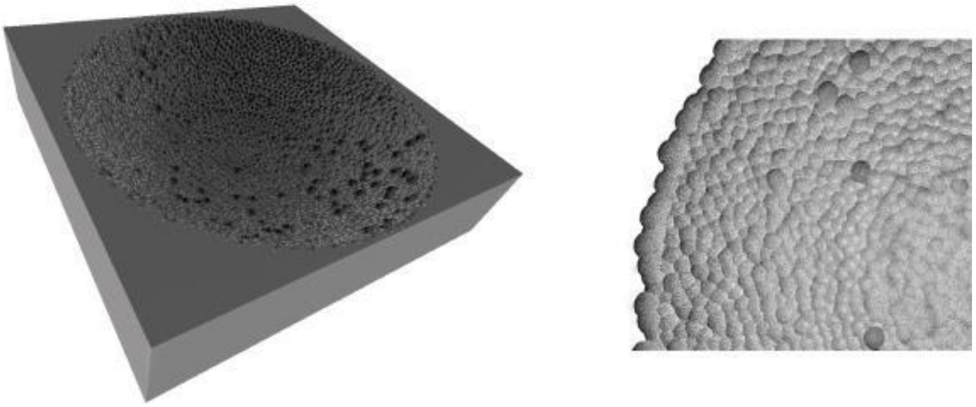

Figure 35: Voxel workpiece after simulation (left) and details of the craters (right).

After the simulation, the resulting models (NURBS and voxels) were compared to the experimental ones with the use of the Hausdorff metric defined in Equation (35) where $X$ and $Y$ are two sets of points and $d(x,y)$ is the Euclidian distance between two points $x$ and $y$. In this case, the $X$ and $Y$ point sets are samples taken over the three-dimensional meshes.

$$d_H\ X,Y\quad max\{\underbrace{sup}_{x\in X}\underbrace{inf}_{y\in Y} d(x,y), \underbrace{sup}_{y\in Y}\underbrace{inf}_{x\in X} d(x,y)\} \tag{35}$$

The Hausdorff metric results are tabulated in Table 10 and are visible in Figure 36. The table gives the minimum, maximum, mean and RMS values of each set of sampled points' Hausdorff distance. Those measurements were made using a software called Meshlab that was previously known as Metro (Cignoni, Rocchini, & Scopigno, 1998).

Table 10: Hausdorff metric results.

| | **NURBS** | | **Voxels** | |
|---|---|---|---|---|
| | **Tool** | **Workpiece** | **Tool** | **Workpiece** |
| $d_H$ min (µm) | 0.000000 | 0.000107 | 0.008184 | 0.000000 |
| $d_H$ max (µm) | 8.629291 | 14.886533 | 2.163380 | 14.917241 |
| $d_H$ mean (µm) | 1.449477 | 3.073571 | 0.858142 | 0.718315 |
| $d_H$ RMS (µm) | 2.521132 | 3.626015 | 0.971600 | 1.682061 |

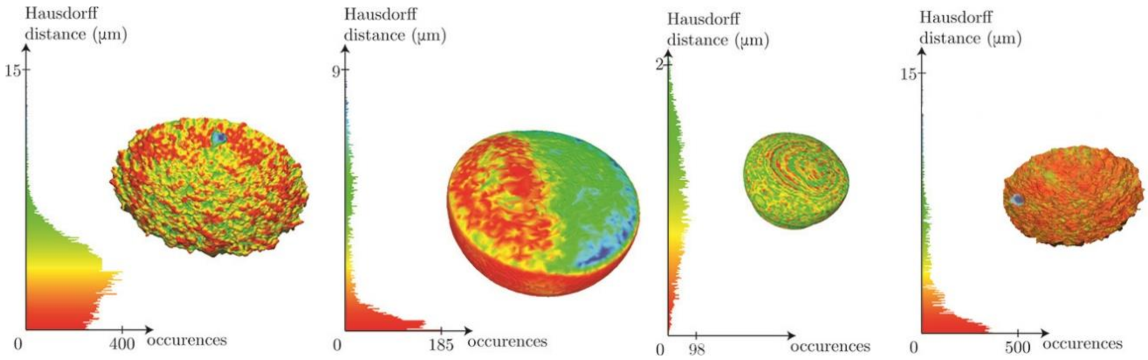

Figure 36: Hausdorff distance maps between experimental and simulated surfaces. From left to right: NURBS workpiece, NURBS tool, Voxels tool, Voxels workpiece.

Figure 36 depicts the maps of the calculated Hausdorff distances. A red colour represents a small difference between the experimental and simulated elements while a blue colour indicates a larger difference.

The values obtained through the NURBS-based simulation and the Voxels-based one are comparable. The NURBS method achieves a 2.52 µm and 3.63 µm Hausdorff RMS distance for the tool and the workpiece, respectively. The Voxels method achieves a 0.97 µm and 1.68 µm Hausdorff RMS distance for the tool and the workpiece, respectively. Those preliminary results alone seem to indicate that the voxels method is slightly superior. However, the main difference lies in the computing time: the voxels method is 16 times faster than the NURBS one. The hierarchical structure provided by Octrees greatly increases the speed of distances calculations and crater insertions.

It is visible on the Hausdorff maps (Figure 36) that the simulation is only precise enough to give a global approximation of the tool shape's evolution after machining. However, considering the stochastic nature of the micro-EDM process, such a result is acceptable and it would be improbable at this stage to expect any simulation to perform any better.

### 3.6. Synthesis

Section 3 has dealt with the presentation of two different simulation methods involving two types of geometries and their related algorithms. Both of them, NURBS and voxels were able to determine the final shapes of the tool and the workpiece to a reasonable degree. A metric called the Hausdorff was used in order to quantify their accuracies and it was concluded that, while both methods achieve similar results, the voxels method is ultimately superior due to its speed. The

NURBS method could be further improved in terms of computational speed through the reduction of tolerances related to the various algorithms (distance search and crater insertion) but that would automatically have an effect on the final geometries and their accuracy.

Another drawback related to NURBS (as well as meshes in general as support geometries for the electrodes) is that they are prone to self-intersection and a reduction in the control point density as the surface is modified. Both of those are detrimental to their use in a simulation tool.

The next section deals with the input parameters of the simulation in the voxels method: the machining gap and the crater dimensions. The previous simulation and its comparison to empirical data has been made using experimental values for those input parameters. The measurement of those values can be tedious in the scope of simulating a great number of machining instances. Chapter 4 will explore the possibilities to build simple predictive models for those input parameters from a dataset built from experiments. The idea is to be able to predict the values to be used in the simulation for machining parameters that haven't been tested before.

# Chapter 4

# Building a database for the efficient choice of simulation parameters

## 4.1. Introduction

While it would be possible to consider the parameters used for the simulation (crater dimensions and therefore volumes, machining gap) on a case by case basis, such an approach would be slow and tedious considering the additional difficulty introduced by the measurement of microscopic craters.

The idea in the present chapter is to study the feasibility of building a non-exhaustive set of data that would link the machining parameters (materials, voltage, current ...) with the obtained results. That result would ideally be the mean shape of the craters average radius and average depth). However the complexity involved in the measurement of craters makes it inconvenient to do so directly.

Considering that fact, what is proposed here is to use the surface roughness as an indicator of the machining's result. The hypothesis being made here is that a certain set of parameters will consistently yield a specific surface roughness that is directly in relation with the shape and dimensions of the craters. On the other hand, simulations will be performed using a variety of simulation parameters and the simulated roughness measured. It would then be possible to link simulation parameters with machining parameters and build a dataset.

The next step will be to build a regression model through the use of artificial intelligence techniques using the collected dataset as a training set. This process is desirable when considering the fact that it will be difficult to conduct an exhaustive campaign to account for all the possible combinations. Different methods will be implemented and tested against a testing set in order to determine which one performs better on this specific problem.

Another parameter to be considered is the machining gap that is also used in the simulation tool. The experimental measurement of that gap is significantly easier. It is proposed to perform 120 experiments with 5 repetitions across the range of machining parameters and train a linear regression model using the data obtained through experimentation. An overview of what is proposed in this section is given Figure 37.

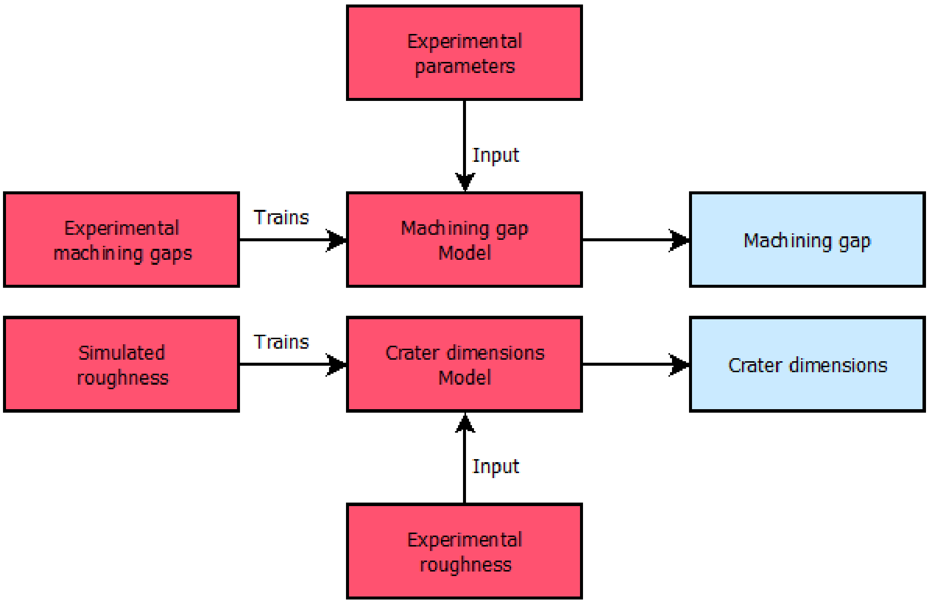

Figure 37: Overview of the relationships between the proposed models (the crater dimensions and the machining gap), their training sets and the inputs to be used.

## 4.2. Roughness

### *4.2.1. Overview*

The roughness campaign revolves around two main steps.

The second step is the collection

n of roughness values issued from the simulation. A certain number of crater dimensions will be used in various simulations and roughness measurements will be made numerically. This is done in order to make a link between the crater dimensions and the resulting roughness in the simulation.

The second is an experimental collection of roughness values. In addition, it is proposed to measure the current and voltage between both electrodes since some machining parameters (most notably energy and current) are unitless index values and aren't representative of the underlying physical concepts.

Once those two steps are performed, it is hypothesized that the knowledge of the experimental roughness will be enough to determine the crater dimensions to be used in the simulation.

### *4.2.2. Simulated roughness*

#### 4.2.2.1. Data generation

The simulated roughness have been performed with a cubic tool of 256x256x256 µm. The dimensions of the workpiece vary depending on the simulation parameters. In order to keep the simulation time under acceptable levels, smaller workpieces have been used when small craters were being considered. The crater resolution was set at 32 voxels per micron. The machining gap was set to 20 µm and a simulated machining performed until a depth of 1 µm was reached. The tool used is significantly bigger than the workpiece in order to make sure that the entirety of the top part of the workpiece is machined. An example of the resulting workpiece is given in Figure 38.

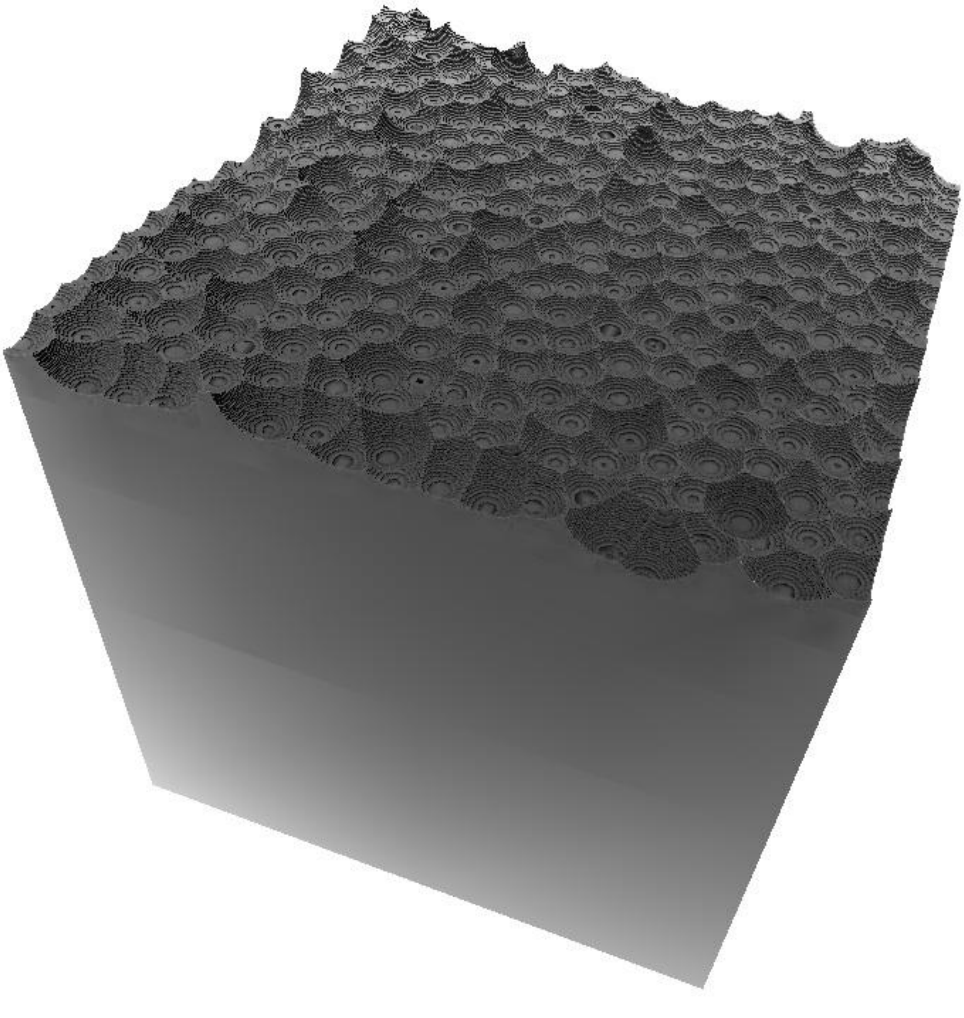

Figure 38: Workpiece after simulation in the context of the roughness campaign. The dimensions of the root node were 16x16x16 µm.

A certain number of crater dimensions were used in the simulation of resulting surface roughness. The crater radii chosen were 0.5, 1, 1.5, 2, 2.5, 3, 3.5 and 4. Each of those values were used with 6 crater depth values found by dividing the crater radius by 1, 1.5, 2, 2.5, 3 and 3.5. Those values were selected in order to cover a wide range of usual values found in micro-EDM. The selected parameters combinations can be found in Table 11. The dimensions of the craters occurring on the tool have no influence on the resulting roughness on the workpiece and therefore aren't specified.

Table 11: Crater dimensions tested for resulting roughness in the simulation.

| **Number** | **Crater radius (µm)** | **Crater depth (µm)** |
|---|---|---|
| 1 | 0.5 | 0.5 |
| 2 | 0.5 | 0.33 |
| 3 | 0.5 | 0.25 |
| 4 | 1 | 1 |
| 5 | 1 | 0.66 |
| 6 | 1 | 0.5 |
| 7 | 1.5 | 1.5 |
| 8 | 1.5 | 1 |
| 9 | 1.5 | 0.75 |
| 10 | 2 | 2 |
| 11 | 2 | 1.33 |
| 12 | 2 | 1 |
| 13 | 2.5 | 2.5 |
| 14 | 2.5 | 1.66 |
| 15 | 2.5 | 1.25 |
| 16 | 3 | 3 |
| 17 | 3 | 2 |
| 18 | 3 | 1.5 |
| 19 | 3.5 | 3.5 |

| **Number** | **Crater radius (µm)** | **Crater depth (µm)** |
|---|---|---|
| 20 | 3.5 | 2.33 |
| 21 | 3.5 | 1.75 |
| 22 | 4 | 4 |
| 23 | 4 | 2.66 |
| 24 | 4 | 2 |
| 25 | 0.5 | 0.2 |
| 26 | 0.5 | 0.17 |
| 27 | 0.5 | 0.16 |
| 28 | 1 | 0.4 |
| 29 | 1 | 0.33 |
| 30 | 1 | 0.29 |
| 31 | 1.5 | 0.6 |
| 32 | 1.5 | 0.5 |
| 33 | 1.5 | 0.43 |
| 34 | 2 | 0.8 |
| 35 | 2 | 0.67 |
| 36 | 2 | 0.57 |
| 37 | 2.5 | 1 |
| 38 | 2.5 | 0.83 |
| 39 | 2.5 | 0.71 |
| 40 | 3 | 1.2 |
| 41 | 3 | 1 |
| 42 | 3 | 0.86 |
| 43 | 3.5 | 1.4 |

| **Number** | **Crater radius (µm)** | **Crater depth (µm)** |
|---|---|---|
| 44 | 3.5 | 1.17 |
| 45 | 3.5 | 1 |
| 46 | 4 | 1.6 |
| 47 | 4 | 1.33 |
| 48 | 4 | 1.14 |

The surface roughness of the 24 resulting octrees was computed by extracting the surface profile from them. This was done by finding all the leaf nodes that possessed a topmost face without any neighbour in the Z+ direction. Those nodes were then converted as clouds of points and saved as a .ply[1] file and an example can be observed in Figure 39.

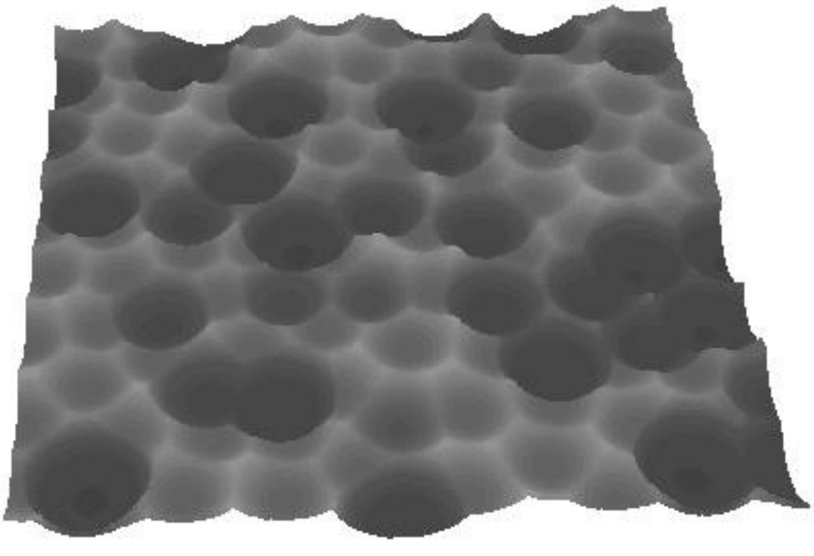

Figure 39: Cloud of points viewed in MeshLab. Profile dimensions: 16x16 µm.

---

[1] Polygon File Format also known as the Stanford Triangle Format. It describes a three-dimensional object as a list of flat polygons.

Each surface is defined by 1000x1000 points for a total of 1 million points. The notation is:

$$\{\mathbf{P}_{i,j}\} \text{ for } \ i,j \ \in [\![1 \dots 1000]\!] \times [\![1 \dots 1000]\!] \tag{36}$$

A small tool was then designed using C#.NET to perform surface area roughness analysis. Different values were computed from the cloud of points after having filtered the low frequency component out (Mitutoyo America Corporation, 2012). A denotes the projected surface of the profile. The altitude $z$ is the distance to the average height of the surface.

**Arithmetic average:**

$$S_a = \frac{1}{A} \iint_A \ |z(x,y)| dxdy \tag{37}$$

**Root mean squared**

$$S_{RMS} = \sqrt{\frac{1}{A} \iint_A \ z \ x,y \ ^2 dxdy} \tag{38}$$

**Maximum valley depth**

$$S_v = \min(z \ x,y \ ) \tag{39}$$

**Maximum peak height**

$$S_p = \max(z \ x,y \ ) \tag{40}$$

**Maximum difference**

$$S_t = S_p - S_v \tag{41}$$

...

**Skewness**

$$S_{sk} = \frac{1}{AS_{RMS}^{3}} \iint_{A} z\ x,y\ ^{3} dxdy \tag{42}$$

**Kurtosis**

$$S_{ku} = \frac{1}{AS_{RMS}^{4}} \iint_{A} z\ x,y\ ^{4} dxdy \tag{43}$$

All the results are given in Table 12. A closer look at the data shows that there might be a linear correlation between the crater depth and $S_p$ or $S_v$. No apparent relationship appears immediately for the crater radius.

Table 12: Simulated roughness results. The values are given with three significant digits to account for the limited precision of experimental data.

| N° | Crater radius (µm) | Crater depth (µm) | Sa (µm) | $S_{RMS}$ (µm) | $S_v$ (µm) | $S_p$ (µm) | $S_t$ (µm) | $S_{sk}$ (µm) | $S_{ku}$ (µm) |
|---|---|---|---|---|---|---|---|---|---|
| 1 | 0.5 | 0.5 | 0.0763 | 0.0929 | -0.175 | 0.262 | 0.438 | 0.162 | 2.47 |
| 2 | 0.5 | 0.33 | 0.0511 | 0.0617 | -0.110 | 0.172 | 0.281 | 0.209 | 2.39 |
| 3 | 0.5 | 0.25 | 0.0771 | 0.0941 | -0.181 | 0.256 | 0.438 | 0.124 | 2.40 |
| 4 | 1 | 1 | 0.143 | 0.178 | -0.368 | 0.570 | 0.938 | 0.433 | 2.85 |
| 5 | 1 | 0.66 | 0.103 | 0.124 | -0.279 | 0.346 | 0.625 | 0.0611 | 2.32 |
| 6 | 1 | 0.5 | 0.0760 | 0.0922 | -0.205 | 0.264 | 0.469 | 0.00190 | 2.37 |
| 7 | 1.5 | 1.5 | 0.283 | 0.328 | -0.740 | 0.698 | 1.44 | -0.444 | 2.13 |
| 8 | 1.5 | 1 | 0.151 | 0.184 | -0.397 | 0.571 | 0.969 | 0.196 | 2.53 |
| 9 | 1.5 | 0.75 | 0.114 | 0.139 | -0.322 | 0.397 | 0.719 | 0.0448 | 2.45 |
| 10 | 2 | 2 | 0.275 | 0.357 | -0.899 | 1.01 | 1.91 | -0.640 | 2.90 |
| 11 | 2 | 1.33 | 0.229 | 0.274 | -0.525 | 0.756 | 1.28 | 0.248 | 2.24 |
| 12 | 2 | 1 | 0.139 | 0.173 | -0.403 | 0.566 | 0.969 | 0.225 | 2.77 |
| 13 | 2.5 | 2.5 | 0.256 | 0.347 | -1.07 | 1.37 | 2.44 | -0.347 | 3.87 |
| 14 | 2.5 | 1.66 | 0.292 | 0.341 | -0.762 | 0.863 | 1.63 | -0.268 | 2.11 |
| 15 | 2.5 | 1.25 | 0.210 | 0.253 | -0.505 | 0.713 | 1.22 | 0.239 | 2.31 |
| 16 | 3 | 3 | 0.269 | 0.354 | -1.22 | 1.66 | 2.88 | 0.229 | 4.33 |
| 17 | 3 | 2 | 0.280 | 0.358 | -0.946 | 1.02 | 1.97 | -0.374 | 2.72 |
| 18 | 3 | 1.5 | 0.260 | 0.308 | -0.665 | 0.804 | 1.47 | -0.0667 | 2.16 |

| N° | Crater radius (µm) | Crater depth (µm) | Sa (µm) | $S_{RMS}$ (µm) | $S_v$ (µm) | $S_p$ (µm) | $S_t$ (µm) | $S_{sk}$ (µm) | $S_{ku}$ (µm) |
|---|---|---|---|---|---|---|---|---|---|
| 19 | 3.5 | 3.5 | 0.289 | 0.374 | -1.13 | 2.09 | 3.22 | 0.673 | 4.24 |
| 20 | 3.5 | 2.33 | 0.247 | 0.325 | -1.05 | 1.20 | 2.25 | -0.181 | 3.54 |
| 21 | 3.5 | 1.75 | 0.289 | 0.378 | -1.04 | 1.18 | 2.22 | -0.411 | 3.14 |
| 22 | 4 | 4 | 0.355 | 0.450 | -1.58 | 2.48 | 3.06 | 1.08 | 4.16 |
| 23 | 4 | 2.66 | 0.329 | 0.429 | -1.02 | 1.60 | 2.63 | 0.00820 | 3.01 |
| 24 | 4 | 2 | 0.317 | 0.383 | -0.837 | 1.10 | 1.94 | -0.137 | 2.33 |
| 25 | 0.5 | 0.2 | 0.0305 | 0.0376 | -0.0594 | 0.0969 | 0.156 | 0.363 | 2.44 |
| 26 | 0.5 | 0.17 | 0.0252 | 0.0303 | -0.0437 | 0.0813 | 0.125 | 0.493 | 2.80 |
| 27 | 0.5 | 0.16 | 0.0208 | 0.0244 | -0.0472 | 0.0778 | 0.125 | 0.738 | 3.53 |
| 28 | 1 | 0.4 | 0.0594 | 0.0716 | -0.114 | 0.198 | 0.313 | 0.263 | 2.37 |
| 29 | 1 | 0.33 | 0.0500 | 0.0601 | -0.107 | 0.175 | 0.281 | 0.127 | 2.34 |
| 30 | 1 | 0.29 | 0.0455 | 0.0551 | -0.114 | 0.136 | 0.250 | -0.112 | 2.38 |
| 31 | 1.5 | 0.6 | 0.0945 | 0.114 | -0.237 | 0.326 | 0.563 | 0.118 | 2.37 |
| 32 | 1.5 | 0.5 | 0.0792 | 0.0967 | -0.213 | 0.255 | 0.469 | 0.0755 | 2.37 |
| 33 | 1.5 | 0.43 | 0.0689 | 0.0837 | -0.151 | 0.224 | 0.375 | 0.145 | 2.40 |
| 34 | 2 | 0.8 | 0.120 | 0.147 | -0.318 | 0.432 | 0.750 | 0.0538 | 2.53 |
| 35 | 2 | 0.67 | 0.109 | 0.131 | -0.274 | 0.351 | 0.625 | 0.0224 | 2.31 |
| 36 | 2 | 0.57 | 0.0859 | 0.106 | -0.220 | 0.311 | 0.531 | 0.124 | 2.46 |
| 37 | 2.5 | 1 | 0.152 | 0.186 | -0.419 | 0.550 | 0.969 | 0.182 | 2.59 |
| 38 | 2.5 | 0.83 | 0.126 | 0.153 | -0.350 | 0.462 | 0.813 | 0.0910 | 2.43 |
| 39 | 2.5 | 0.71 | 0.110 | 0.135 | -0.338 | 0.380 | 0.719 | -0.0374 | 2.48 |
| 40 | 3 | 1.2 | 0.192 | 0.235 | -0.487 | 0.700 | 1.19 | 0.312 | 2.51 |
| 41 | 3 | 1 | 0.150 | 0.183 | -0.444 | 0.556 | 1.00 | 0.157 | 2.53 |
| 42 | 3 | 0.86 | 0.135 | 0.164 | -0.396 | 0.479 | 0.875 | 0.0179 | 2.41 |
| 43 | 3.5 | 1.4 | 0.244 | 0.290 | -0.618 | 0.757 | 1.38 | 0.0337 | 2.12 |
| 44 | 3.5 | 1.17 | 0.179 | 0.222 | -0.432 | 0.724 | 1.16 | 0.356 | 2.67 |
| 45 | 3.5 | 1 | 0.149 | 0.185 | -0.446 | 0.586 | 1.03 | 0.154 | 2.61 |
| 46 | 4 | 1.6 | 0.271 | 0.324 | -0.784 | 0.778 | 1.56 | -0.364 | 2.29 |
| 47 | 4 | 1.33 | 0.228 | 0.274 | -0.567 | 0.777 | 1.34 | 0.192 | 2.26 |
| 48 | 4 | 1.14 | 0.190 | 0.230 | -0.487 | 0.606 | 1.09 | 0.142 | 2.34 |

#### 4.2.2.2. Model construction

Those results were then converted to the .arff file format which is used by WEKA (Short for Waikato Environment for Knowledge Analysis).

WEKA is a framework that offers a certain number of machine learning algorithms out of the box. It features tools for data pre-processing, classification, regression, clustering and much more (Holmes, Donkin, & Witten, 1994). It is written in Java and is open-source which makes it possible to check the implementations of the various algorithms as well as adding new ones.

The WEKA software offers the possibility to quickly display the various attributes into a plot matrix which is very convenient to quickly assess the visible trends. The plot matrix for the crater radius, the crater depth, $S_a$, $S_{RMS}$, $S_v$, $S_p$, $S_t$, $S_{sk}$, $S_{ku}$ is displayed in Figure 40.

As could be expected there is a strong linear correlation between $S_p$ and the crater depth as well as between $S_v$ and the crater depth. The first approach will be to determine a simple linear regression between those parameters that gives:

$$S_p = 0.5836 * C_{depth} - 0.031 \tag{44}$$

$$S_v = 0.4033 * C_{depth} + 0.0202 \tag{45}$$

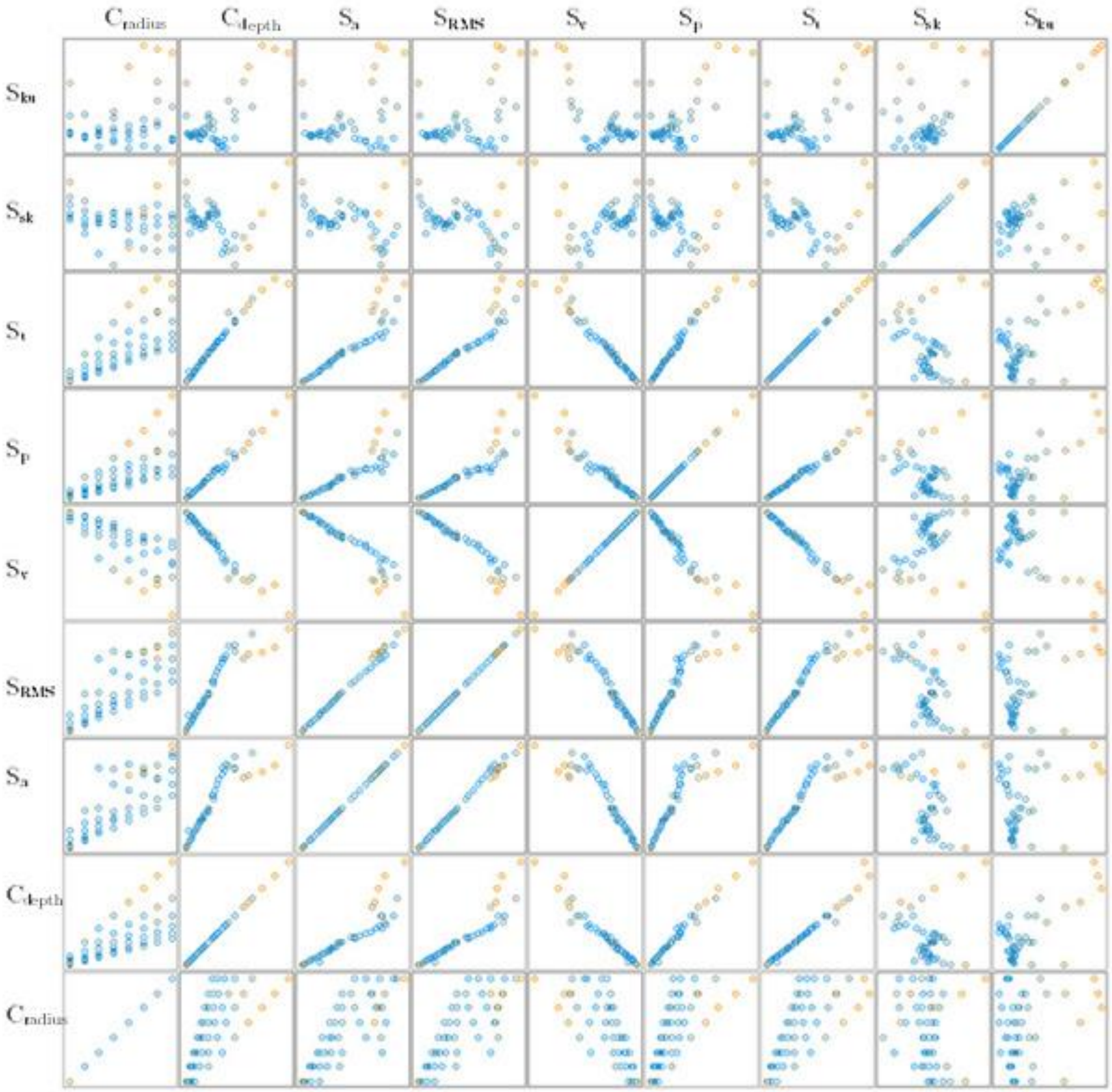

Figure 40: Plot Matrix of the various roughness measures and crater dimensions.

The error measures associated to those models are as follow in Table 13.

The mean absolute error (MAE) for a set of n predictions is:

$$\mathrm{MAE} = \frac{1}{n}\sum_{i=1}^{n}|f_i - y_i| \tag{46}$$

Where $f_i$ is the predicted value and $y_i$ is the actual value.

Using the same notations, the other error measures are:

Table 13: Error measures for the $\mathrm{S_p}$ and $\mathrm{S_v}$ models.

| **Error measure** | **$\mathrm{S_p}$ model** | **$\mathrm{S_v}$ model** |
|---|---|---|
| Correlation coefficient | 0.9901 | 0.9688 |
| Mean absolute error | 0.0455 | 0.0549 |
| Root mean square error | 0.0716 | 0.0889 |
| Relative absolute error (%) | 11.9205 | 18.6202 |
| Root relative squared error (%) | 13.7398 | 24.3491 |

The root mean square error (RMSE):

$$\mathrm{RMSE} = \sqrt{\frac{1}{n}\sum_{i=1}^{n} \; f_i - y_i} \tag{47}$$

The relative absolute error (RAE):

$$\mathrm{RAE} = \frac{\sum_{i=1}^{n} |f_i - y_i|}{\sum_{i=1}^{n} |y_i - \overline{y_\imath}|} \tag{48}$$

Where $\overline{y_\imath}$ is the average of the $y_i$.

The relative squared error (RSE):

$$\mathrm{RSE} = \frac{\sum_{i=1}^{n} \; f_i - y_i \;\; ^{2}}{\sum_{i=1}^{n} \; f_i - \overline{y_\imath} \;\; ^{2}} \tag{49}$$

The models were obtained through manual selection of the relevant attributes and 10-fold cross-validation. The high correlation coefficients as well as the low error measures are to be expected considering that while the simulation process isn't entirely deterministic due to a certain randomness in the computation of the minimum distances, it is minimal when considering the global result.

Considering these previous results and keeping in mind that the final goal is to determine crater dimensions to be used in the simulation tool, the next step will be to verify that it is possible to determine the crater depth from the value of $S_p$, $S_v$ or both at the same time.

Once again, using a simple linear regression yields the following models:

$$C_{depth} = 1.6845 * S_p + 0.0724 \tag{50}$$

$$C_{depth} = 2.3592 * S_v + 0.0103 \tag{51}$$

Using a multi-linear regression model makes it possible to express $C_{depth}$ as a function of $S_p$ and $S_v$ simultaneously:

$$C_{depth} = 0.713 * S_v + 1.20 * S_p + 0.03 \tag{52}$$

Table 14: Error measures for $f(S_p)$, $f(S_v)$ and $f(S_p,S_v)$.

| **Error measure** | **$f(S_p)$ model** | **$f(S_v)$ model** | **$f(S_p,S_v)$ model** |
|---|---|---|---|
| Correlation coefficient | 0.99115 | 0.9695 | 0.9927 |
| Mean absolute error | 0.0803 | 0.1215 | 0.0544 |
| Root mean square error | 0.1203 | 0.2116 | 0.1045 |
| Relative absolute error (%) | 11.296 | 18.0376 | 8.0684 |
| Root relative squared error (%) | 12.9896 | 23.9251 | 11.8164 |

While using the f($S_p$,$S_v$) model to predict the crater depth to be used only provides with a marginally higher correlation coefficient (0.9927 against 0.9903 and 0.9695) when compared with the other two models, all of the various error measures are significantly smaller. Using both $S_p$ and $S_v$ in the prediction of the crater depth to be used provides with a more accurate value.

The knowledge of $S_p$ and $S_v$ is therefore sufficient when searching the crater depth. The t-values of the coefficients and their associated p-values were computed to analyse their statistical significance. Those values are given in Table 15. According to the table, the coefficients for $S_v$ and $S_p$ have a high statistical significance but not for the intercept coefficient which has a higher value than a set threshold of 5%. This indicate that said coefficient might be equal to zero which would make sense since values of zero for $S_v$ and $S_p$ should naturally lead to the absence of craters and therefore to crater depths equal to zero.

Table 15: Standard error, t-values and associated p-values for the crater depth model.

| **Coefficient** | **Value** | **Standard error** | **t-value** | **Pr(>\|t\|)** |
|---|---|---|---|---|
| $S_v$ | 0.713 | 0.131 | 5.42 | 2.25e-6 |
| $S_p$ | 1.20 | 0.0924 | 13.0 | <2e-16 |
| Intercept | 0.03 | 0.0225 | 1.55 | 0.126 |

The rest of this section will focus on finding which parameters can be used to determine a precise value for the crater radius. Since the plot matrix does not provide a clear indication of a specific path to explore, attribute selection is first performed.

Attribute selection (feature selection, variable selection or variable subset selection) is the process of eliminating variables in the problem that are deemed to be irrelevant or redundant with other variables.

The best subset of attributes determined is reduced to $S_a$, the arithmetic average roughness. The result is a linear regression. The error measures are tabulated in Table 16.

$$C_{radius} = 9.6924 * S_a + 0.63 \tag{53}$$

The model's error measures are too high to provide any accurate prediction for the crater radius. An explanation would be that the surface profile roughness parameters are all amplitude parameters.

Table 16: Error measures for the $C_{radius}$ model.

| **Error measure** | **$C_{radius}$ model** |
|---|---|
| Correlation coefficient | 0.7655 |
| Mean absolute error | 0.5832 |
| Root mean square error | 0.7376 |
| Relative absolute error (%) | 56.6402 |
| Root relative squared error (%) | 62.4881 |

Since they all give information related to the amplitude of vertical deviations when compared to the mean line, they are better suited for the prediction of the crater depth rather than the crater radius.

This observation leads to the exploration of other roughness parameters known as spatial parameters. In order to understand some of the parameters further described, the notion of the discrete autocorrelation function (ACF) is explained (Leach, 2013). This function is found by multiplying the considered surface by a duplicate of itself shifted with a displacement vector ($\tau_x$, $\tau_y$). The function issued from this multiplication is then integrated over the considered area and normalized to $S_q$. The ACF is:

$$G(\tau_x, \tau_y) = \frac{\iint_A \; z \; x, y \; z(x - \tau_x, y - \tau_y) dxdy}{\iint_A \; z \; x, y \; ^2 dxdy} \tag{54}$$

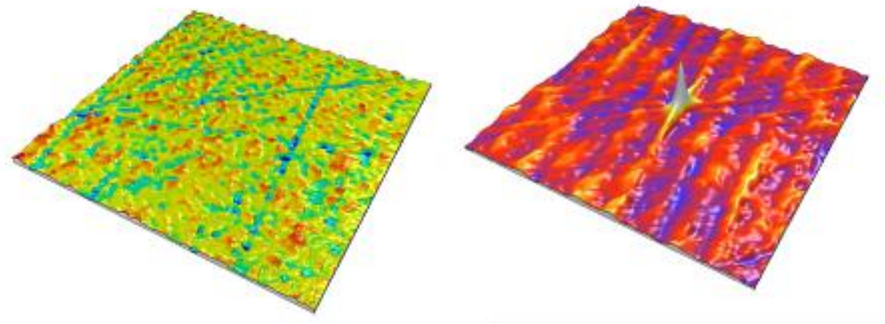

Figure 41: An example surface (left) and the representation of its autocorrelation function (right). Reproduced from (Blateyron, s.d.).

As depicted in Figure 41, a central peak equal to 1 (maximum of autocorrelation) is visible in the centre of the visual representation of the ACF. If the values of $\tau_x$ and $\tau_y$ are equal to 0, then the correlation is at its maximum. Small variations from 0 still yield high correlation values.

In order to compute the $S_{al}$ and $S_{tr}$ parameters, a thresholding of 0.2 is carried out on the ACF which leads to the representation of Figure 42.

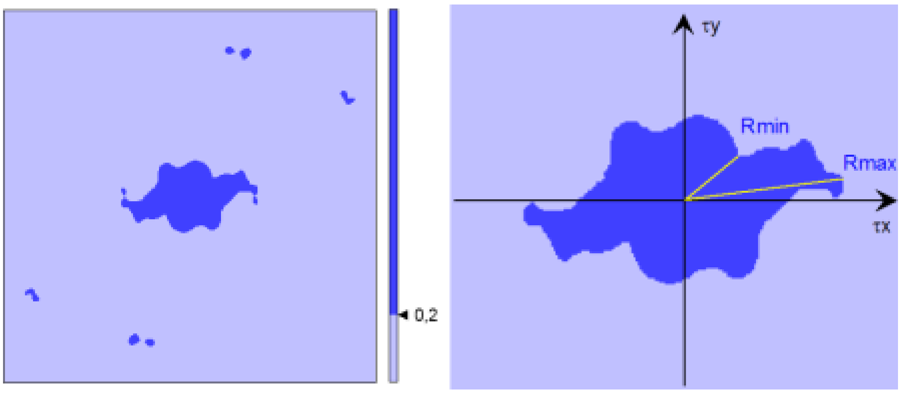

Figure 42: Autocorrelation function with a threshold value of 0.2. Reproduced from (Blateyron, s.d.).

### Fastest decay auto-correlation rate, $S_{al}$ (µm)

The fastest decay auto-correlation rate or auto-correlation length, $S_{al}$, is a measure of the magnitude of the ($\tau_x$, $\tau_y$) vector that minimizes correlation. The direction chosen for the computation of this distance is the one that yields the smallest $S_{al}$ value. Its value is shown in Figure 42 as $R_{min}$.

### Texture aspect ratio of the surface, $S_{tr}$ (no unit)

The texture aspect ratio of the surface, $S_{tr}$ is a measure of the isotropy of the surface's texture. It is the ratio between $S_{al}$, the fastest decay auto-correlation rate and the slowest decay auto-correlation rate (shown as $R_{max}$ in Figure 42).

### Texture direction of the surface, $S_{td}$ (°)

The texture direction of the surface is a measure of the dominant direction of the lay of a surface. It is computed from the Angular Power Spectral Density Function (APSDF) of the surface. The APSDF is determined from the Fourier analysis of the surface through the integration of each sine components as a function of an angle.

Other parameters were considered, the topological characterization of surface motifs (Leach, 2013).

**The mean hills area, $S_{ha}$ (µm²)**

**The mean dales area, $S_{da}$ (µm²)**

**The mean hills volume, $S_{hv}$ (µm³)**

**The mean dales volume, $S_{dv}$ (µm³)**

The surfaces were then analysed again to add those characterizations. The values are tabulated in Table 17.

Table 17: Results for the spatial and topological characterization measures.

| N° | Crater radius | Crater depth | $S_{al}$ (µm) | $S_{tr}$ | $S_{td}$ (°) | $S_{da}$ (µm²) | $S_{ha}$ (µm²) | $S_{dv}$ (µm³) | $S_{hv}$ (µm³) |
|---|---|---|---|---|---|---|---|---|---|
| 1 | 0.5 | 0.5 | 0.328 | 0.869 | 42.3 | 0.628 | 0.402 | 0.014 | 0.0013 |
| 2 | 0.5 | 0.33 | 0.281 | 0.873 | 176 | 0.437 | 0.374 | 0.00609 | 0.000774 |
| 3 | 0.5 | 0.25 | 0.331 | 0.85 | 132 | 0.584 | 0.38 | 0.0101 | 0.00106 |
| 4 | 1 | 1 | 0.613 | 0.874 | 47.5 | 1.92 | 1.81 | 0.0655 | 0.00894 |
| 5 | 1 | 0.66 | 0.593 | 0.804 | 138 | 1.32 | 0.895 | 0.0396 | 0.00135 |
| 6 | 1 | 0.5 | 0.549 | 0.863 | 50.8 | 1.44 | 1.06 | 0.0348 | 0.00201 |
| 7 | 1.5 | 1.5 | 1.14 | 0.877 | 177 | 5.69 | 4.4 | 0.652 | 0.0225 |
| 8 | 1.5 | 1 | 0.896 | 0.874 | 81.3 | 3.87 | 3.55 | 0.187 | 0.0162 |
| 9 | 1.5 | 0.75 | 0.883 | 0.885 | 47.5 | 3.27 | 4.52 | 0.136 | 0.0224 |
| 10 | 2 | 2 | 1.47 | 0.778 | 132 | 9.45 | 7.32 | 1.49 | 0.0592 |
| 11 | 2 | 1.33 | 1.18 | 0.881 | 17 | 7.92 | 7.49 | 0.446 | 0.0409 |
| 12 | 2 | 1 | 1.02 | 0.885 | 102 | 5.35 | 6.82 | 0.33 | 0.0783 |
| 13 | 2.5 | 2.5 | 1.67 | 0.791 | 51 | 10.7 | 10.3 | 1.32 | 0.0965 |
| 14 | 2.5 | 1.66 | 1.75 | 0.802 | 3.75 | 11 | 10.2 | 1.22 | 0.0666 |
| 15 | 2.5 | 1.25 | 1.47 | 0.91 | 86.8 | 9.28 | 9.33 | 0.667 | 0.0587 |
| 16 | 3 | 3 | 1.52 | 0.878 | 12.5 | 15.8 | 12.6 | 2.64 | 0.0822 |
| 17 | 3 | 2 | 1.88 | 0.878 | 51 | 16.8 | 14.6 | 2.58 | 0.12 |
| 18 | 3 | 1.5 | 1.94 | 0.801 | 86 | 14.2 | 15.9 | 1.3 | 0.12 |
| 19 | 3.5 | 3.5 | 1.61 | 0.931 | 56 | 16.7 | 18.4 | 2.77 | 0.312 |

| N° | Crater radius | Crater depth | $S_{al}$ (µm) | $S_{tr}$ | $S_{td}$ (°) | $S_{da}$ (µm$^2$) | $S_{ha}$ (µm$^2$) | $S_{dv}$ (µm$^3$) | $S_{hv}$ (µm$^3$) |
|---|---|---|---|---|---|---|---|---|---|
| 20 | 3.5 | 2.33 | 1.88 | 0.969 | 66.5 | 15.2 | 17.5 | 1.99 | 0.221 |
| 21 | 3.5 | 1.75 | 2.17 | 0.837 | 132 | 21.1 | 16 | 2.83 | 0.13 |
| 22 | 4 | 4 | 1.59 | 0.829 | 148 | 24.2 | 19.4 | 4.86 | 0.25 |
| 23 | 4 | 2.66 | 2.46 | 0.919 | 42.3 | 27.8 | 26.3 | 4.38 | 0.296 |
| 24 | 4 | 2 | 2.46 | 0.892 | 57.8 | 30.8 | 28.3 | 4.23 | 0.247 |
| 25 | 0.5 | 0.2 | 0.235 | 0.838 | 39.5 | 0.353 | 0.475 | 0.00246 | 0.00088 |
| 26 | 0.5 | 0.17 | 0.207 | 0.886 | 47.7 | 0.301 | 0.421 | 0.00191 | 0.000732 |
| 27 | 0.5 | 0.16 | 0.197 | 0.855 | 129 | 0.255 | 0.421 | 0.000519 | 0.000849 |
| 28 | 1 | 0.4 | 0.48 | 0.83 | 123 | 1.3 | 0.889 | 0.0246 | 0.00174 |
| 29 | 1 | 0.33 | 0.47 | 0.784 | 141 | 1.49 | 1.16 | 0.0287 | 0.00205 |
| 30 | 1 | 0.29 | 0.523 | 0.73 | 65 | 1.16 | 1.24 | 0.0129 | 0.00195 |
| 31 | 1.5 | 0.6 | 0.8 | 0.857 | 132 | 2.91 | 1.93 | 0.0938 | 0.0039 |
| 32 | 1.5 | 0.5 | 0.854 | 0.942 | 93 | 2.42 | 2.23 | 0.0676 | 0.00442 |
| 33 | 1.5 | 0.43 | 0.826 | 0.907 | 163 | 3.15 | 2.74 | 0.0751 | 0.00648 |
| 34 | 2 | 0.8 | 1.18 | 0.755 | 155 | 6.41 | 7.31 | 0.257 | 0.0447 |
| 35 | 2 | 0.67 | 1.09 | 0.911 | 171 | 4.96 | 4.04 | 0.197 | 0.00891 |
| 36 | 2 | 0.57 | 1.09 | 0.871 | 8.51 | 4.47 | 2.96 | 0.14 | 0.00513 |
| 37 | 2.5 | 1 | 1.45 | 0.924 | 94 | 8.06 | 9.65 | 0.392 | 0.0568 |
| 38 | 2.5 | 0.83 | 1.42 | 0.928 | 103 | 9 | 9.79 | 0.459 | 0.0346 |
| 39 | 2.5 | 0.71 | 1.39 | 0.949 | 176 | 10.1 | 10.5 | 0.473 | 0.0358 |
| 40 | 3 | 1.2 | 1.78 | 0.931 | 94 | 12.9 | 12.7 | 0.797 | 0.0571 |
| 41 | 3 | 1 | 1.65 | 0.873 | 86.3 | 11.9 | 12 | 0.69 | 0.0506 |
| 42 | 3 | 0.86 | 1.66 | 0.885 | 93.7 | 13.3 | 14.1 | 0.659 | 0.109 |
| 43 | 3.5 | 1.4 | 1.87 | 0.787 | 86.5 | 20.4 | 22.2 | 2.03 | 0.107 |
| 44 | 3.5 | 1.17 | 1.83 | 0.815 | 82.5 | 16.5 | 15.1 | 1.17 | 0.0832 |
| 45 | 3.5 | 1 | 1.8 | 0.91 | 42.2 | 15.7 | 20.9 | 0.956 | 0.17 |
| 46 | 4 | 1.6 | 2.55 | 0.895 | 118 | 23.3 | 24.5 | 2.61 | 0.175 |
| 47 | 4 | 1.33 | 2.26 | 0.886 | 42.2 | 22.7 | 26 | 1.43 | 0.159 |
| 48 | 4 | 1.14 | 2.35 | 0.946 | 86.5 | 20.4 | 23.7 | 1.05 | 0.189 |

A simple linear regression was performed in order to extract a relationship between the crater radius and the spatial/topological parameters. WEKA outputs the following model:

$$\begin{aligned} C_{radius} = {} & 0.8898 * S_{al} + 0.0648 * S_{da} - 0.162 * S_{dv} + 2.4544 * S_{hv} \\ & + 0.4538 \end{aligned} \tag{55}$$

The error measures given in Table 18 give an acceptable correlation coefficients. The relative error measures however, being above 20% indicate that the model isn't likely to perform well with a test set.

Table 18: Error measures for the crater radius model limited to spatial and topological surface parameters.

| **Error measure** | **C$_{\mathbf{radius}}$ model** |
|---|---|
| Correlation coefficient | 0.9647 |
| Mean absolute error | 0.2229 |
| Root mean square error | 0.304 |
| Relative absolute error (%) | 21.6456 |
| Root relative squared error (%) | 25.6194 |

The next logical step is to consider the entirety of the surface roughness characterization parameters. Once again, a linear regression is performed and the output is:

$$\begin{aligned} C_{radius} = a_1 \; * \; C_{depth} + a_2 \; * Ratio \; + \; a_3 \; * \; S_a \; + a_4 * \; S_v \; + \; a_5 \\ * \; S_t \; + a_6 \; * \; S_{sk} \; + a_7 \; * \; S_{ku} \; + \; a_8 \; * \; S_{al} \; + \; a_9 \\ * \; S_{da} \; + \; a_{10} \; * \; S_{dv} \; + \; a_{11} \end{aligned} \quad (56)$$

Where *Ratio* is the ratio between the crater radius and the crater depth. For the sake of clarity, the various coefficients' values, the related standard errors, the t-values and p-values associated to the t-values are given in Table 19.

Table 19: Coefficients computed for the crater radius model.

| **Coefficient** | **Value** | **Std Error** | **t-value** | **Pr(>\|t\|)** |
|---|---|---|---|---|
| $a_1$ | 0.2339 | 0.177 | 1.32 | 0.195 |
| $a_2$ | 0.1543 | 0.044 | 3.48 | 0.001 |
| $a_3$ | -6.6465 | 1.20 | -5.52 | 2.78e-6 |
| $a_4$ | 1.6209 | 0.378 | 4.28 | 1.24e-4 |
| $a_5$ | 0.3371 | 0.216 | 1.56 | 0.127 |
| $a_6$ | 0.5971 | 0.112 | 5.31 | 5.41e-6 |
| $a_7$ | -0.4757 | 0.106 | -4.48 | 6.91e-5 |
| $a_8$ | 1.1758 | 0.159 | 7.36 | 9.38e-9 |
| $a_9$ | 0.0502 | 0.0158 | 3.16 | 0.003 |
| $a_{10}$ | -0.2078 | 0.0685 | -3.03 | 0.004 |
| $a_{11}$ | 0.9443 | 0.275 | 3.434 | 0.001 |

When considering Pr(>|t|) and a threshold value of 5%, coefficients $a_1$ and $a_5$ seem to not be statistically significant and those coefficients could actually be equal to zero.

Table 20: Error measures for the crater radius model using all parameters

| **Error measure** | **$C_{radius}$ model** |
|---|---|
| Correlation coefficient | 0.9929 |
| Mean absolute error | 0.0963 |
| Root mean square error | 0.1367 |
| Relative absolute error (%) | 9.3514 |
| Root relative squared error (%) | 11.5836 |

When considering Pr(>|t|) and a threshold value of 5%, coefficients a1 and a5 seem to not be statistically significant and those coefficients could actually be equal to zero.

Table 20 presents with a significant improvement over the model limited to spatial and topological parameters with error measures that are halved.

#### 4.2.2.3. Test sets

In addition to the validation performed through 10-fold cross validation, a test set was generated using parameters distinct from the 48 combinations used in the training set. Since the validation set is used during the training, it will always output lower error values than an actual test set that the model has never encountered before. This is why a separate test set is important.

Table 21 shows the 12 sets of parameters that were used. The first nine sets of parameters were generated from values within the range of the training set while the last three are outside of it.

The crater depth models were tested against the testing set and provided with the results given in Table 22.

$S_p$ and a combination of $S_p$ and $S_v$ do however perform as expected. Both have similar root mean squared error measures and the third model has a lower mean absolute error. The plot of the predicted values against the actual values for the model base on a combination of $S_p$ and $S_v$ is depicted in Figure 43

Table 21: Parameters used for the generation of the test set.

| **Simulation** | **Crater radius** | **Crater depth** |
|---|---|---|
| T1 | 1.2 | 1.2 |
| T2 | 1.2 | 0.8 |
| T3 | 1.2 | 0.6 |
| T4 | 1.7 | 1.7 |
| T5 | 1.7 | 1.13 |
| T6 | 1.7 | 0.85 |
| T7 | 2.7 | 2.7 |
| T8 | 2.7 | 1.8 |
| T9 | 2.7 | 1.35 |
| T10 | 4.5 | 4.5 |
| T11 | 4.5 | 3 |
| T12 | 4.5 | 2.25 |

Table 22: Error measures with the test sets associated with the crater depth models.

| **Error measure** | **f($S_p$) model** | **f($S_v$) model** | **f($S_p$,$S_v$) model** |
|---|---|---|---|
| Correlation coefficient | 0.9915 | 0.6186 | 0.9943 |
| Mean absolute error | 0.1078 | 0.3409 | 0.0749 |
| Root mean squared error | 0.1618 | 0.8882 | 0.1757 |

Those results show that the model based on $S_v$ does not work well with the test set and should therefore not be considered for further use. The models based on

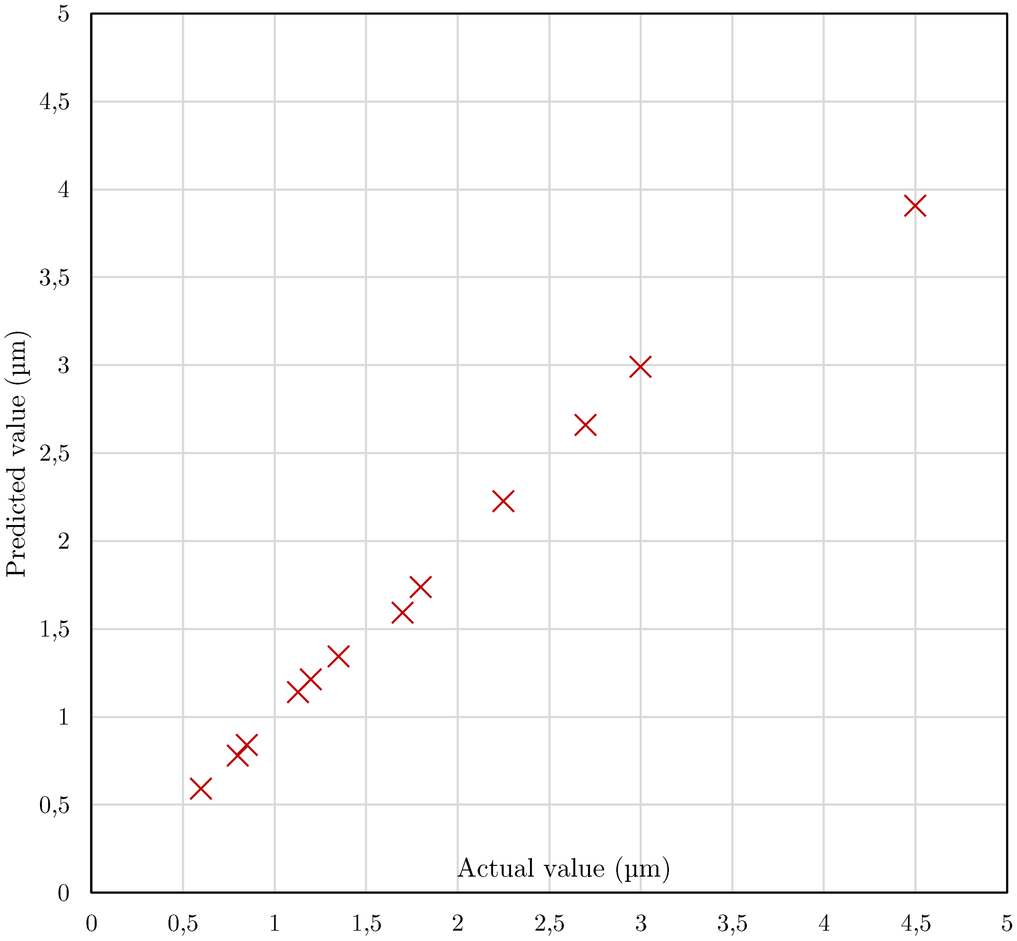

Figure 43: Crater depth model, predicted values against actual values.

Using the same test set, the model for the crater radius is tested in the same manner with results shown in Table 23.

Table 23: Error measures with the test sets associated with the crater radius model.

| **Error measure** | **$C_{radius}$ model** |
|---|---|
| Correlation coefficient | 0.9339 |
| Mean absolute error | 0.2393 |
| Root mean squared error | 0.5151 |

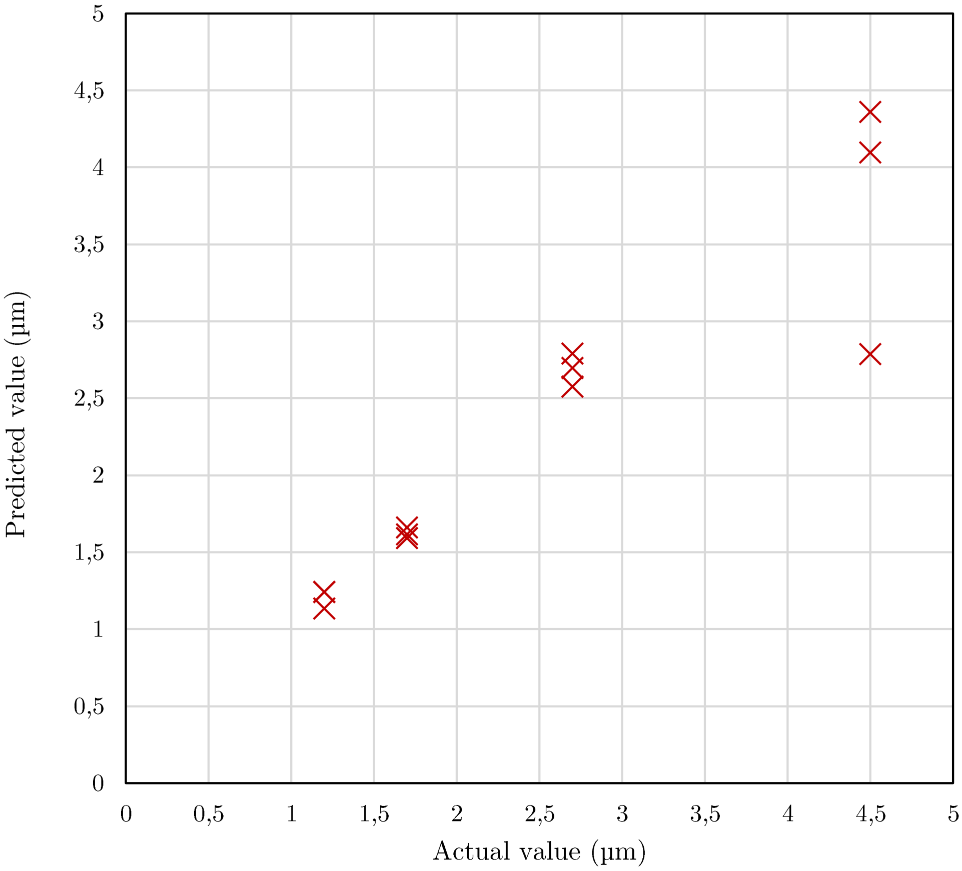

Figure 44: Crater radius model, predicted values against actual values.

While giving acceptable results, the error measures can be considered quite high. A closer look to the predicted values shows that the model (Figure 44) is slightly weaker when working with values for the crater radius that are in the high range. Considering that those values are actually quite large when considering the case of micro-EDM, the dispersion that occurs with large values isn't problematic.

## 4.3. Machining gap

### *4.3.1. Overview*

The other main parameter that is used as an input of the simulation is the machining gap. Here it is considered as the smallest distance at which a spark can occur and is therefore quite determinant on the final result. While the measure of this value isn't as complicated as the crater dimensions, it is nevertheless interesting to explore what can be done to predict such a value.

The concept of direct measurement of electrical data in order to ignore machine-specific parameters is introduced.

### *4.3.2. Electrical data acquisition*

As mentioned previously, the nature of some of the machining parameters make them unreliable to be used when required for further analysis involving regression. The energy level for example is set on the machine as an index value and the same goes for the current.

In order to obtain more precise information from the machining itself, it has been decided to proceed with the acquisition of voltage and current information between the electrodes with the help of a Tektronix digital oscilloscope. The connection between the Sarix SX 200 machine and the oscilloscope was achieved through the use of a current probe for the measurement of the current and two wires connected to both polarities of the machine.

The Tektronix oscilloscope functioning under a Windows operating system, it was possible to use Matlab directly on the oscilloscope without resorting to a connection to a personal computer.

The toolbox did various tasks autonomously. It performed the setting up of the oscilloscope according to the machining parameters used and launched a series of acquisitions during the machining process to obtain electrical discharge data.

The communication with the oscilloscope was performed with the use of a VISA (Virtual Instrument Standard Architecture) object under Matlab associated with a GPIB (General-Purpose Interface Bus) controller.

The main limitation resided in the input buffer. Only a certain quantity of data could be transferred in a certain amount of time. A size of 12 million bytes was chosen as it was deemed to be a good compromise between speed and quantity of data. Every 20 seconds, 0.5 second of discharge data could be captured and transferred to Matlab.

An important point is that the capture of both channels (voltage and current) can only be captured sequentially. In order to ensure the synchronization of both channels, a falling edge trigger was set on the oscilloscope with a holding time of 10 seconds.

Every data patch of 0.5 second contained 12 million points which provided with a sufficient resolution when sampling both waveforms.

The raw data was then converted to a Matlab matrix format (.mat).

### *4.3.3. Electrical data processing*

#### 4.3.3.1 Filtering

Before being able to extract numerical values from the electrical data, it is necessary to perform some filtering in order to remove the noise inherent to electrical circuits such as thermal noise.

This task needs to take into account the fact that the sparks are very short in duration and can be confused as noise by a filtering algorithm. However the frequency bands of the noise and of the sparks are sufficiently different to not pose any significant problem during the filtering process.

Here, the data sample resolution makes it possible to use a simple moving average filter with a window size of 1000 for the current and voltage. Figure 45 shows an example of data before and after filtering. After filtering, power data (P(t)) is created through the multiplication of the filtered current and voltage data.

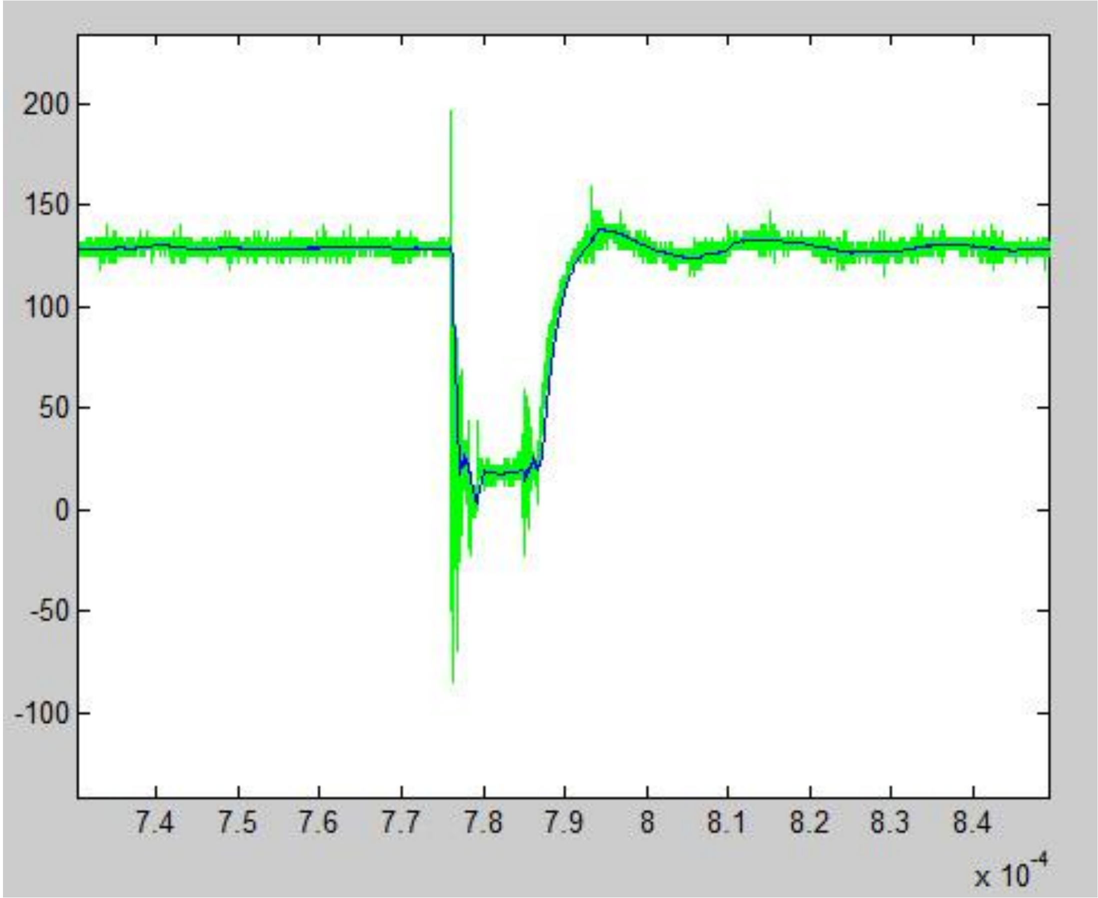

Figure 45: Voltage (in V) against time (in s). Green: unfiltered, blue: filtered.

#### 4.3.3.2 The sparks presence function

The sparks presence function is at the core of the analysis process since the way it is built will be decisive in the computation of all the values extracted from the data. It is a function that decides whether or not a spark is occurring considering the electrical data.

The sparks presence function is as follows:

$$S_p\ t\ = \begin{cases} 0 \text{ if there isn't a spark at } t \\ 1 \text{ if there is a spark at } t \end{cases} \tag{57}$$

In order to build that function, the notion of a spark has to be considered. Observation of the graphs shows that the beginning of spark is characterized by:

- A sudden decrease in the voltage accompanied by:
- An increase in the current.

In the same way it is possible to say that a spark ends when the current is back to a value close to zero.

Taking into account these observations, the beginning of a spark happens:

- When the voltage is below a certain level $V_{threshold}$ and:
- When the current is above a certain level $I_{start}$

A spark ends when:

- A spark is currently on going
- The current is below a certain level $I_{end}$

The choice of these three parameters, $V_{treshold}$, $I_{start}$ and $I_{end}$ is crucial since the sparks presence function needs to return the correct number of sparks. Additionally, it needs to do so while making the sparks detected be comparable between themselves and, therefore, achieve a certain level of consistency. Those parameters need to be chosen such as:

- The correct number of sparks is returned,
- The sparks detected maximize their energy.

Those values are also dependent on the experimental parameters and therefore would be different for each hole that is machined.

A procedure was defined to choose those values with the use of particle swarm optimisation. For each set of parameters that was used in the experimental campaign, a figure was selected and the sparks contained in it counted. With the knowledge of the correct number of sparks and using it as a constraint in the optimisation process, the algorithm was capable of finding the values of $V_{treshold}$, $I_{start}$ and $I_{end}$ that maximized the energy of all sparks. Those values were then used for the remainder of the figures.

### *4.3.4. Experimental campaign*

The machining gap experimental campaign was conducted at the University of Bergamo in Italy with the same machine used in the roughness campaign. The Sarix SX200 machine was once again used and equipped with a similar electrical data acquisition apparatus. The experimental campaign consisted in holes drilled in a steel plate of a thickness of 1 mm. The tools used were cylindrical electrodes made of tungsten carbide. Two diameters were used for those electrodes: 150 and 300 µm. The process parameters used are given in Table 24.

Table 24: Process parameters used in the machining gap campaign.

| **Diameter** | **Energy level (index)** | **Current (index)** | | | **Voltage (V)** | | |
|---|---|---|---|---|---|---|---|
| 300 | 206 | 10 | 35 | 50 | 80 | 110 | 140 |
| | 365 | 40 | 60 | 80 | 80 | 100 | 120 |
| 150 | 206 | 15 | 30 | 50 | 80 | 110 | 140 |
| | 365 | 20 | 40 | 60 | 70 | 95 | 110 |

Those parameters were chosen in consideration of the limitations of the machine and the diameter of the electrode.

Given a number of repetitions of 5 for each set of process parameters, a total of 120 holes were machined while electrical data was collected and processed using the methods described previously.

The diameters of the hole machined were measured with an optical microscope.

The raw data is available in Addendum A.

### *4.3.5. Data analysis*

For all the experiments, electrical data was collected using an oscilloscope. Every five seconds, a sample of 10µm was collected for the voltage and current waveforms. The data was processed in the same was as described previously and average values for the peak current, peak voltage, energy per spark, number of sparks and occurrence of those sparks was computed.

The data file was converted to the .arff format used by WEKA and a simple Linear Regression model was trained with the following results in Table 25.

Table 25: Error measures for the training of a machining gap linear regression model.

| **Coefficient** | **Value** |
|---|---|
| Correlation coefficient | 0.9904 |
| Mean absolute error | 0.0078 |
| Root mean squared error | 0.0108 |
| Relative absolute error | 10.0% |
| Root relative squared error | 13.8% |

The output relationship was:

$$\begin{gathered} D_{top} = 0.001 \ * \ d_{electrode} \ + \\ 0.0005 * I_{peak} \ + \\ 0.0004 * V_{peak} \ + \\ -0.0001 * E_{spark} \ + \\ 0.0528 \end{gathered} \tag{58}$$

## 4.4. Testing the roughness model in the simulation

### *4.4.1. Overview*

Two models have been determined using multi-linear regression algorithms for the machining gap and the crater dimensions. What is proposed in this section is to test the use of the roughness model to determine the correct input parameters of the simulation.

### *4.4.2. Experimental roughness*

#### 4.4.2.1. Overview

The roughness experimental campaign proposes to machine shallow cylindrical features using a range of machining parameters. Those features are obtained through the use of a cylindrical rod made of Tungsten Carbide (W 94, Co 6). The dimensions of said rod are:

- Diameter: 0.290 mm.
- Length: 30 mm.

The workpiece is a small sheet of stainless steel (AISI 420: Fe 86.7, Cr 13, C 0.3). Its dimensions are 50x50x1 mm.

The experimental machining parameters were chosen in order to use a wide range of the machine's capabilities while keeping the machining time under acceptable levels. The chosen parameters are tabulated in Table 26.

A total of 18 parameters combination are used. The machining depth was set to 50 µm. The energy levels chosen are in the higher range of what is possible. However, using low energy levels resulted in extremely long experiments (6 to 7 hours for a single hole).

Table 26: Machining parameters used for the roughness experimental campaign. Unitless parameters are machine indexes.

| **N°** | **Energy (index)** | **I (index)** | **V (V)** | **Freq (kHz)** | $t_{on}$ **(μs)** | **Gap** | **Regulation** | **Polarity** |
|---|---|---|---|---|---|---|---|---|
| 1 | 365 | 40 | 80 | 120 | 5 | 60 | 03_01 | - |
| 2 | 365 | 40 | 100 | 120 | 5 | 60 | 03_01 | - |
| 3 | 365 | 40 | 120 | 120 | 5 | 60 | 03_01 | - |
| 4 | 365 | 60 | 80 | 120 | 5 | 60 | 03_01 | - |
| 5 | 365 | 60 | 100 | 120 | 5 | 60 | 03_01 | - |
| 6 | 365 | 60 | 120 | 120 | 5 | 60 | 03_01 | - |
| 7 | 365 | 80 | 80 | 120 | 5 | 60 | 03_01 | - |
| 8 | 365 | 80 | 100 | 120 | 5 | 60 | 03_01 | - |
| 9 | 365 | 80 | 120 | 120 | 5 | 60 | 03_01 | - |
| 10 | 206 | 10 | 80 | 120 | 5 | 60 | 03_01 | - |
| 11 | 206 | 10 | 110 | 120 | 5 | 60 | 03_01 | - |
| 12 | 206 | 10 | 140 | 120 | 5 | 60 | 03_01 | - |
| 13 | 206 | 35 | 80 | 120 | 5 | 60 | 03_01 | - |
| 14 | 206 | 35 | 110 | 120 | 5 | 60 | 03_01 | - |
| 15 | 206 | 35 | 140 | 120 | 5 | 60 | 03_01 | - |
| 16 | 206 | 50 | 80 | 120 | 5 | 60 | 03_01 | - |
| 17 | 206 | 50 | 110 | 120 | 5 | 60 | 03_01 | - |
| 18 | 206 | 50 | 140 | 120 | 5 | 60 | 03_01 | - |

#### 4.4.2.2. Results

As determined in the simulated roughness section, the values required for use in the model are: $S_a, S_v, S_t, S_{sk}, S_{ku}, S_{al}, S_{da}$ and $S_{dv}$ for the crater radius model and

$S_p$ and $S_v$ for the crater depth model. A Form Talysurf PGI machine was used for the surface profile measurements. This measuring machine is capable of 0.8nm of vertical resolution and the result are given in Table 27. The sign of $S_{sk}$ is indicative of the probability density of the amplitude distribution. A negative skewness means that the measured profile has deep, sharp valleys. On the contrary, a positive skewness is indicative of high, sharp peaks.

Table 27: Experimental roughness measurements to be used with the model for the determination of crater dimensions. Values are given with three significant figures.

| **N°** | $S_a$ **(µm)** | $S_v$ **(µm)** | $S_p$ **(µm)** | $S_t$ **(µm)** | $S_{sk}$ | $S_{ku}$ | $S_{al}$ **(µm)** | $S_{da}$ **(µm$^2$)** | $S_{dv}$ **(µm$^3$)** |
|---|---|---|---|---|---|---|---|---|---|
| 1 | 0.0662 | 0.403 | 0.578 | 0.965 | 0.195 | 2.52 | 0.895 | 3.90 | 0.185 |
| 2 | 0.101 | 0.716 | 0.765 | 1.30 | 0.244 | 2.28 | 1.16 | 8.00 | 0.448 |
| 3 | 0.178 | 0.827 | 0.860 | 1.59 | -0.263 | 2.08 | 1.35 | 10.9 | 1.21 |
| 4 | 0.176 | 0.911 | 0.925 | 1.62 | -0.266 | 2.11 | 1.61 | 10.8 | 1.20 |
| 5 | 0.266 | 1.16 | 1.26 | 1.97 | -0.375 | 2.67 | 1.78 | 16.9 | 2.59 |
| 6 | 0.290 | 1.31 | 1.62 | 2.65 | 0.00840 | 2.97 | 1.96 | 27.9 | 4.44 |
| 7 | 0.290 | 1.19 | 1.33 | 2.29 | 0.179 | 3.59 | 1.81 | 15.5 | 1.98 |
| 8 | 0.299 | 1.32 | 1.62 | 2.66 | 0.00810 | 3.05 | 2.20 | 27.3 | 4.30 |
| 9 | 0.302 | 1.46 | 1.76 | 2.61 | 0.00810 | 2.98 | 2.42 | 27.5 | 4.40 |
| 10 | 0.0314 | 0.112 | 0.171 | 0.293 | 0.217 | 2.40 | 0.136 | 0.464 | 0.00700 |
| 11 | 0.0455 | 0.175 | 0.259 | 0.437 | 0.164 | 2.43 | 0.256 | 0.627 | 0.0140 |
| 12 | 0.0453 | 0.282 | 0.345 | 0.628 | 0.0601 | 2.31 | 0.589 | 1.34 | 0.0395 |
| 13 | 0.0620 | 0.334 | 0.559 | 0.946 | 0.428 | 2.81 | 0.622 | 1.91 | 0.0667 |
| 14 | 0.0756 | 0.753 | 0.591 | 1.42 | 0.196 | 2.12 | 0.942 | 5.66 | 0.202 |
| 15 | 0.175 | 1.06 | 0.967 | 1.62 | -0.270 | 2.12 | 1.70 | 10.9 | 1.24 |
| 16 | 0.139 | 0.763 | 0.850 | 1.28 | 0.248 | 2.25 | 1.26 | 7.78 | 0.449 |

| N° | $S_a$ (µm) | $S_v$ (µm) | $S_p$ (µm) | $S_t$ (µm) | $S_{sk}$ | $S_{ku}$ | $S_{al}$ (µm) | $S_{da}$ (µm²) | $S_{dv}$ (µm³) |
|---|---|---|---|---|---|---|---|---|---|
| 17 | 0.248 | 1.10 | 1.13 | 1.96 | -0.373 | 2.76 | 1.75 | 16.5 | 2.58 |
| 18 | 0.296 | 1.28 | 1.44 | 2.23 | 0.434 | 3.57 | 1.93 | 15.4 | 2.01 |

The values in Table 27 when used with the roughness model give out the following values for the crater dimensions (Table 28).

Table 28: Crater dimensions issued from the roughness model for the experimental values. Values are given with three significant figures.

| N° | Crater depth (µm) | Crater radius (µm) | Ratio |
|---|---|---|---|
| 1 | 1.02 | 1.34 | 1.65 |
| 2 | 1.47 | 2.20 | 1.50 |
| 3 | 1.66 | 1.85 | 1.63 |
| 4 | 1.80 | 2.21 | 1.60 |
| 5 | 2.37 | 3.17 | 1.34 |
| 6 | 2.92 | 3.90 | 1.34 |
| 7 | 2.48 | 3.40 | 1.37 |
| 8 | 2.93 | 3.57 | 1.43 |
| 9 | 3.18 | 4.08 | 1.36 |
| 10 | 0.320 | 2.46 | 1.89 |
| 11 | 0.471 | 2.01 | 1.55 |
| 12 | 0.651 | 1.76 | 1.69 |
| 13 | 0.946 | 1.79 | 1.37 |
| 14 | 1.28 | 1.66 | 1.30 |
| 15 | 1.95 | 2.54 | 1.40 |
| 16 | 1.60 | 2.97 | 1.59 |

| | | | |
|---|---|---|---|
| 17 | 2.18 | 3.36 | 1.38 |
| 18 | 2.67 | 3.61 | 1.35 |

### *4.4.3. The experimental campaign*

Three different tool shapes were designed and made using a wire-EDM machine. The diameter of the wire used was of a nominal diameter of 300 µm. The nominal profiles are given in Figure 46 while a picture of the achieved shape is given Figure 47. Their dimensions are available in Addendum B. For each shape, 16 of them were made for a total of 48. The chosen profiles were designed to be used in a two-dimensional version of the simulation tool in order to speed up the process for the initial development of the method.

The process parameters that were used for the three different shapes are tabulated in Table 29. The objective depth was set to 300 µm and all features were made using the Sarix SX200 machine.

Figure 46: The three shapes used in the validation of the roughness and machining gap models.

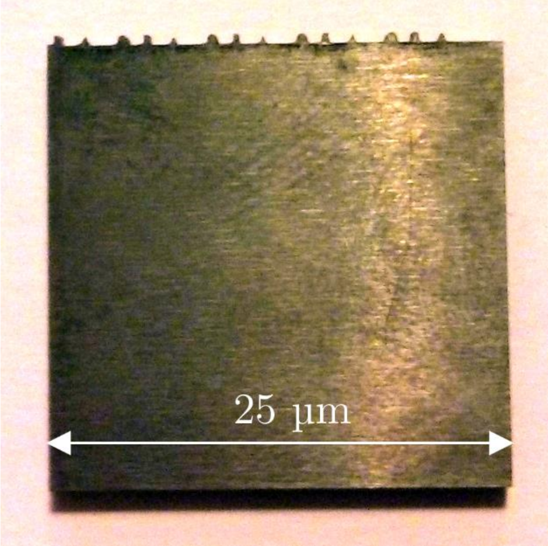

Figure 47: The manufactured shapes.

Considering the likelihood of major differences occurring between the nominal shapes designed and the actual tools, those were measured using a Nikon AZ100 multi-purpose microscope shown in Figure 48.

Figure 48: The Nikon AZ100 multi-purpose microscope.

An example of each of the tool shapes before machining is given in Figure 49 while an example of the tools after machining is given Figure 50, examples of workpieces after machining are given Figure 51.

Figure 49: Tools measured before machining.

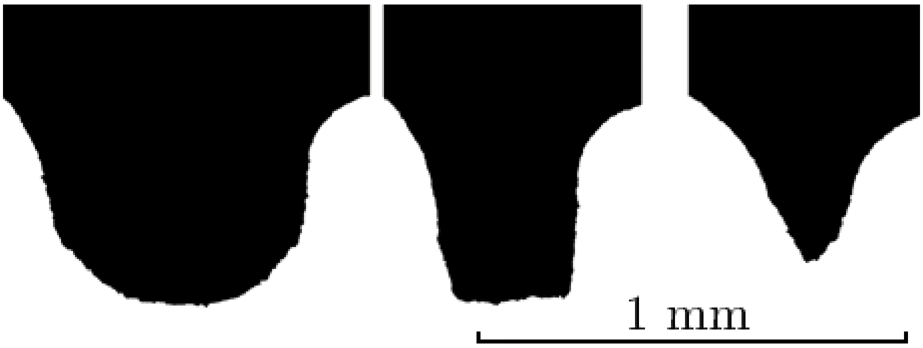

Figure 50: Tools measured after machining.

Figure 51: Workpiece features after machining.

### *4.4.4. The simulations*

#### 4.4.4.1. Overview

Using the values of the crater dimensions determined in the previous section and using the values for the machining gaps accordingly to the machining parameters, simulations for three different tool shapes were made using the machining parameters in Table 29.

Table 29: Parameters used in the simulation of the roughness experimental campaign.

| N° | Energy (index) | I (index) | V (V) | Workpiece crater radius (µm) | Workpiece crater depth (µm) | Gap (µm) | Tool Wear ratio |
|---|---|---|---|---|---|---|---|
| 1 | 365 | 40 | 80 | 1.33 | 1.01 | 43 | 0.50 |
| 2 | 365 | 40 | 100 | 2.19 | 1.46 | 43 | 0.28 |
| 3 | 365 | 40 | 120 | 1.85 | 1.65 | 46 | 0.13 |
| 4 | 365 | 60 | 80 | 2.20 | 1.79 | 45 | 0.39 |
| 5 | 365 | 60 | 100 | 3.17 | 2.37 | 47 | 0.20 |
| 6 | 365 | 60 | 120 | 3.89 | 2.92 | 48 | 0.12 |
| 7 | 365 | 80 | 80 | 3.40 | 2.47 | 55 | 0.20 |
| 8 | 365 | 80 | 100 | 3.57 | 2.93 | 48 | 0.13 |
| 9 | 206 | 10 | 80 | 2.45 | 0.320 | 59 | 0.55 |
| 10 | 206 | 10 | 110 | 2.00 | 0.471 | 70 | 0.54 |
| 11 | 206 | 10 | 140 | 1.76 | 0.651 | 63 | 0.52 |
| 12 | 206 | 35 | 80 | 1.79 | 0.946 | 70 | 0.55 |
| 13 | 206 | 35 | 110 | 1.66 | 1.28 | 65 | 0.54 |
| 14 | 206 | 35 | 140 | 2.53 | 1.95 | 70 | 0.55 |
| 15 | 206 | 50 | 80 | 2.96 | 1.60 | 71 | 0.49 |
| 16 | 206 | 50 | 110 | 3.36 | 2.17 | 64 | 0.45 |

The crater dimensions for the tool were determined using previous knowledge of the tool wear ratio (the ratio between the volume removed on the tool and the volume removed on the workpiece) that is available in Table 29.

The microscope images were converted to pixels in a quadtree structure. An example of such a conversion is given Figure 52.

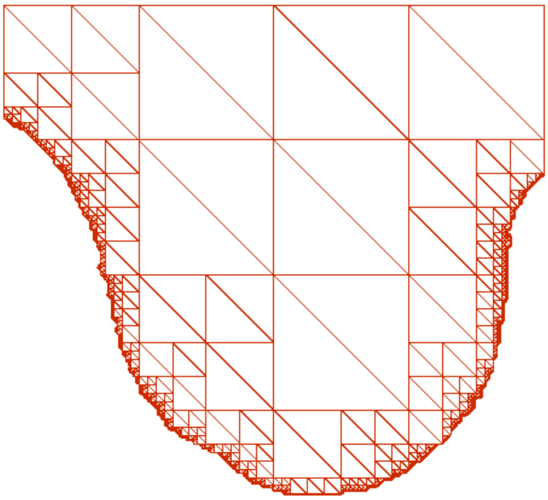

Figure 52: One of the circular tools that have been converted to pixels in a quadtree data structure.

#### 4.4.4.2. Results

The resulting features on the workpiece were then compared to the experimental ones after alignment. An example of a simulated workpiece is available Figure 53 and a comparison is available Figure 54. The differences between the simulated and experimental workpiece are coloured in red and blue. The difference in colour denotes whether or not it is an area that should have been removed (red) or not (blue) in the simulation. The error measure is the sum of those two areas. The area of the red difference is 2361 µm$^2$ and the area of the blue error is 540 µm$^2$

for a total of 2901 µm$^{\mathbf{2}}$. The deviation or error relative to the simulated workpiece area (64412 µm$^{\mathbf{2}}$) is 4.50%.

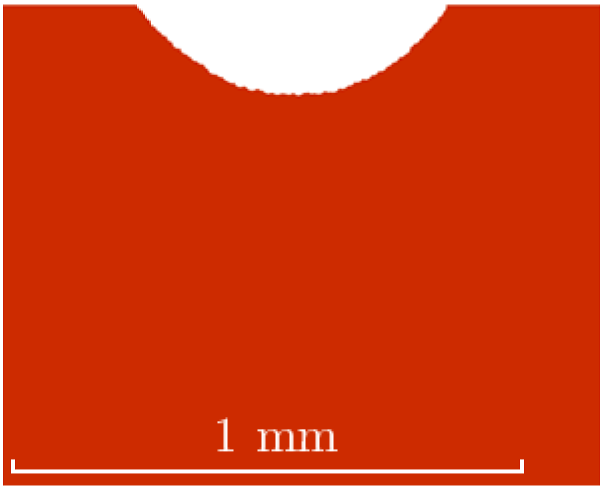

Figure 53: Result on the workpiece for a circular tool shape.

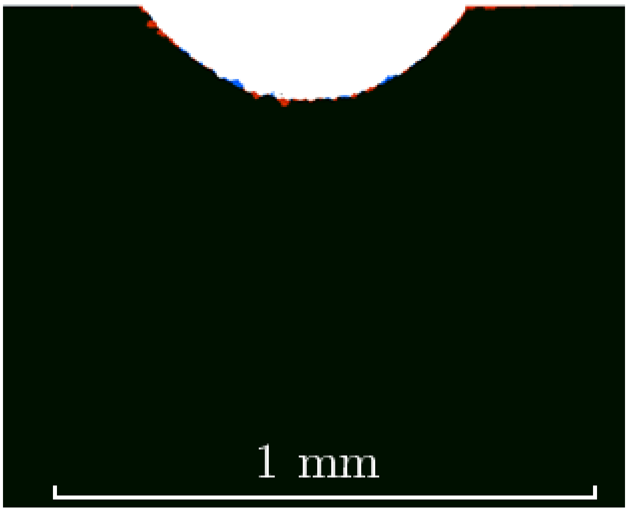

Figure 54: Comparison between simulated and experimental workpiece. In red: volume that should have been removed in the simulation. In blue: volume that shouldn't have been removed in the simulation.

The error measures are tabulated in Table 30 for the circular shapes, Table 31 for the square shapes and Table 32 for the triangular shapes.

Table 30: Error measures of the simulations for the circular shapes.

| **N°** | **Area red (µm²)** | **Area blue (µm²)** | **Total error (µm²)** | **Simulated workpiece area (µm²)** | **Relative error (%)** |
|---|---|---|---|---|---|
| 1 | 2500 | 679 | 3179 | 74347 | 4.28 |
| 2 | 2616 | 722 | 3338 | 78881 | 4.23 |
| 3 | 2865 | 739 | 3604 | 82510 | 4.37 |
| 4 | 2535 | 677 | 3212 | 77797 | 4.13 |
| 5 | 2629 | 725 | 3354 | 81297 | 4.13 |
| 6 | 2833 | 765 | 3598 | 82749 | 4.35 |
| 7 | 2630 | 675 | 3305 | 79594 | 4.15 |
| 8 | 2636 | 722 | 3358 | 84406 | 3.98 |
| 9 | 2361 | 540 | 2901 | 64412 | 4.50 |
| 10 | 2365 | 675 | 3040 | 66470 | 4.57 |
| 11 | 2496 | 695 | 3191 | 70005 | 4.56 |
| 12 | 2409 | 651 | 3060 | 66561 | 4.60 |
| 13 | 2417 | 675 | 3092 | 72000 | 4.29 |
| 14 | 2531 | 718 | 3249 | 75917 | 4.28 |
| 15 | 2582 | 669 | 3251 | 67784 | 4.80 |
| 16 | 2811 | 710 | 3521 | 71594 | 4.92 |

Table 31: Error measures of the simulations for the square shapes.

| N° | Area red (um²) | Area blue (um²) | Total error (um²) | Simulated workpiece area (um²) | Relative error (%) |
|---|---|---|---|---|---|
| 1 | 3913 | 1067 | 4980 | 116252 | 6.70 |
| 2 | 4053 | 1118 | 5171 | 123021 | 6.56 |
| 3 | 4431 | 1139 | 5570 | 128139 | 6.75 |
| 4 | 3922 | 1048 | 4970 | 121016 | 6.39 |
| 5 | 4084 | 1118 | 5202 | 126543 | 6.40 |
| 6 | 4442 | 1207 | 5649 | 129330 | 6.83 |
| 7 | 4095 | 1049 | 5144 | 123915 | 6.46 |
| 8 | 4063 | 1130 | 5193 | 131360 | 6.15 |
| 9 | 3701 | 834 | 4535 | 100179 | 7.04 |
| 10 | 3709 | 1042 | 4751 | 103291 | 7.15 |
| 11 | 3895 | 1088 | 4983 | 108580 | 7.12 |
| 12 | 3762 | 1022 | 4784 | 104275 | 7.19 |
| 13 | 3744 | 1054 | 4798 | 112106 | 6.66 |
| 14 | 3940 | 1105 | 5045 | 117693 | 6.65 |
| 15 | 4031 | 1050 | 5081 | 106420 | 7.50 |
| 16 | 4371 | 1108 | 5479 | 111444 | 7.65 |

Table 32: Error measures of the simulations for the triangular shapes.

| **N°** | **Area red (um$^2$)** | **Area blue (um$^2$)** | **Total error (um$^2$)** | **Simulated workpiece area (um$^2$)** | **Relative error (%)** |
|---|---|---|---|---|---|
| 1 | 1300 | 480 | 1780 | 23389 | 7.61 |
| 2 | 1291 | 474 | 1765 | 23749 | 7.43 |
| 3 | 1477 | 460 | 1937 | 25784 | 7.51 |
| 4 | 1268 | 401 | 1669 | 23513 | 7.10 |
| 5 | 1379 | 465 | 1844 | 25770 | 7.16 |
| 6 | 1427 | 480 | 1907 | 24943 | 7.65 |
| 7 | 1319 | 457 | 1776 | 24103 | 7.37 |
| 8 | 1298 | 437 | 1735 | 25158 | 6.90 |
| 9 | 1228 | 363 | 1591 | 20025 | 7.95 |
| 10 | 1241 | 447 | 1688 | 20687 | 8.16 |
| 11 | 1258 | 411 | 1669 | 21003 | 7.95 |
| 12 | 1221 | 428 | 1649 | 20261 | 8.14 |
| 13 | 1266 | 452 | 1718 | 22698 | 7.57 |
| 14 | 1265 | 431 | 1696 | 22635 | 7.49 |
| 15 | 1265 | 411 | 1676 | 20237 | 8.28 |
| 16 | 1379 | 438 | 1817 | 21194 | 8.57 |

The results tabulated indicate that the simulation tool is able to achieve results at 4 to 9% of the actual result. There are multiple potential sources of error including:

- The inherent stochastics nature of the process.
- The unexpected accumulation of debris.

- The inherent error measure of the model linking roughness values to crater dimensions.

While an error of 4 to 9% is far from optimal, considering all the potential sources of error, the result achieved by the simulation tool is quite honourable and can be confidently used for global approximations of the micro-EDM die-sinking process machining process. Those error values are too high to conclude that the simulation tool can be as accurate as to predict the location of individual craters but this was never the objective. The location and amplitude of the tool wear were, however, correctly predicted to a certain extent. Additionally, lower error values were found for the circular shape. Shapes with sharp corners (rectangle and triangle) have higher relative error values. This was especially true with the triangular shape.

### 4.5. Synthesis

Chapter 4 has explored various option to remove the systematic dependency of the simulation on experimental values for the crater dimensions or the machining gap. It was proposed to use models built on empirical data that are able to predict correct values for the crater dimensions and the machining gap with the knowledge of the machining parameters.

The crater dimensions were based on the measurement of surface roughness values and a good correlation between various parameters was shown. This is supported by the various t-values and their related p-values that indicate that most of the coefficients determined are statistically significant. These findings were to be expected since the roughness measured is related to the simulation that is a mostly deterministic tool. It would be interesting to extend the present work with the use of more advanced machine learning algorithms in order to make the predictions applicable to a wider range.

The machining gap relied on the measurement of electrical data in order to remove the dependency on machine specific parameters. This method should be extended to the roughness models in order to generalize the inputs to be used to any kind of micro-EDM machine. At the present moment the machining gap model hasn't been directly tested with a simulation even though the model's error measures are quite low. It is of note that there is an expected difference between the side wear and the bottom wear of a tool. However, as a first approach, it was supposed that the wear was uniform around the tool when building the model due to the fact that measuring side wear is easier.

The results obtained with the use of those models ranges between 4 to 9% which is marginally worse that what can be observed in the simulation available in Chapter 3 but, considering all the potential sources of error previously mentioned, those results can be deemed satisfactory.

As can be seen in Figure 50, the tools obtained through wire-cutting differ from the original design due to the machining errors that arise. However, since the tools used in the simulation are taken from the actual experimental tools and not their nominal design, the errors due to deviation between theoretical tools and the actual ones are taken into account.

The next section deals with the use of the simulation tool in an iterative loop that has the goal of optimizing the initial tool shape.

# Chapter 5

# Tool shape optimisation

## 5.1. An iterative optimisation process

### *5.1.1. Introduction*

What is proposed in the present section is to develop an iterative simulation process that adjusts the shape of the tool electrode in order to obtain an ultimate shape potentially able to produce in a single step the targeted workpiece or one that is as close as possible.

Although the tool presented in the previous sections deals with three-dimensional simulations, to demonstrate and validate the optimisation concept more efficiently and rapidly it was decided to perform optimisations using the simulation with two-dimensional profiles. However, since all the developed algorithms have been done so taking this fact into account, the method can easily be adapted for use with three-dimensional shapes.

Thus, considering a targeted workpiece profile $W_{target}$ to be produced on a workpiece, each iteration of the optimisation process consists in four main steps that are illustrated in Figure 55 and Figure 56.

- Compute the difference or mismatch $\varepsilon$ between the target workpiece ($W_{target}$) and the previous resulting workpiece profile $W_{result}$. On the first iteration, the $W_{result}$ is an empty workpiece without any features since no machining has been done yet. This means that the first difference ε represents the actual overall target area to be removed (or volume in three dimensions).

- Using the mismatch, the virtual workpiece profile $W_{virtual}$ is created in the first iteration or modified in the others.
- Using the virtual workpiece $W_{virtual}$, a virtual tool profile $T_{virtual}$ is generated, which would produce the selected $W_{virtual}$ if no wear occurred on the tool during the process. At the last iteration of the process, $T_{virtual}$ is considered to be the optimal tool shape.
- An EDM simulation using the $T_{virtual}$ tool on a new workpiece (not machined) is done. The workpiece provided at the end of the simulation, $W_{result}$ is analysed for the next iteration.

The accuracy of the optimisation process, $A\%$, is measured with the following metric:

$$A\% = \frac{A_{W_{target}} - \varepsilon}{A_{W_{target}}} . 100 \tag{59}$$

Where $A_{W_{target}}$ (µm$^2$) is the area of the target workpiece feature and ε is the mismatch area (µm$^2$) previously defined.

The process is repeated until the accuracy no longer improves by more than 0.5%, meaning that the resulting workpiece is as close to the targeted workpiece as can be produced with this process. As a consequence, an optimal tool for the desired workpiece is obtained.

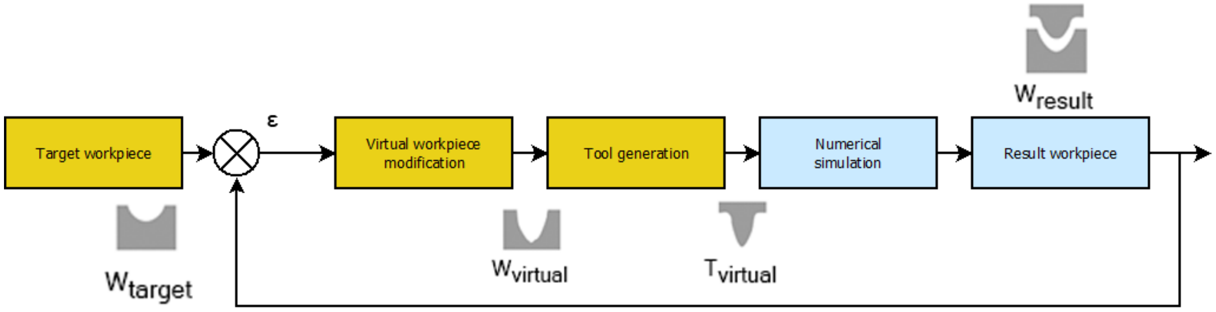

Figure 55 : Iterative optimisation process.

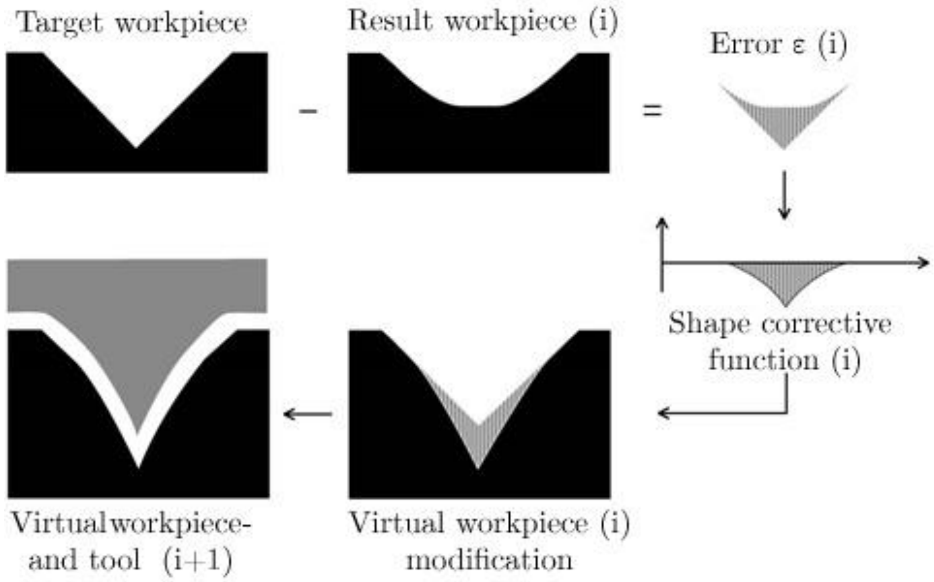

Figure 56: A single iteration of the process.

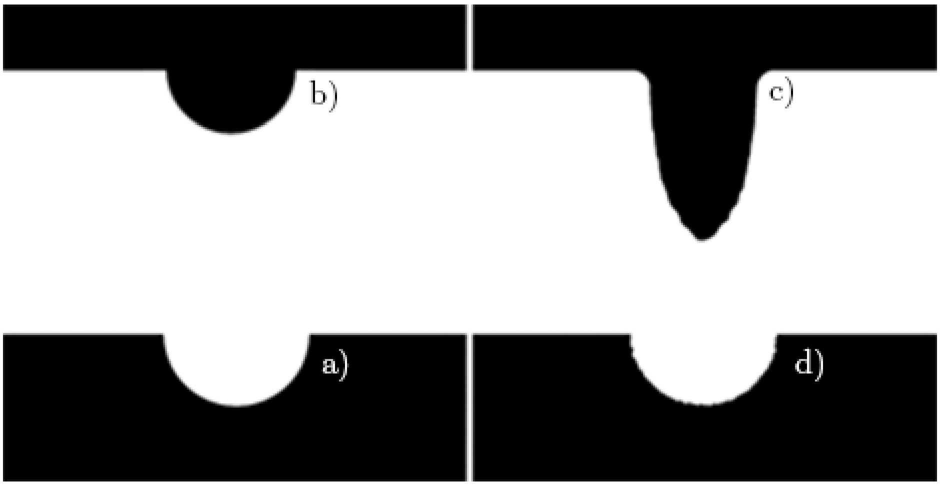

Figure 57: Tool shape optimisation capabilities. Left (top and bottom): the non-optimized tool shape and the target profile. Right (top and bottom): the optimized tool shape and the feature it produces.

An example of the capabilities of the tool shape optimisation process is given in Figure 57. Elements a) and b) represent respectively the targeted workpiece profile $W_{target}$ to be produced on the workpiece and the initial tool shape (the initial tool shape is chosen as the negative of the target profile accounting for the expected machining gap). Elements c and d represent respectively the optimized tool shape (final virtual tool profile $T_{virtual}$) after five iterations and the resulting workpiece (final result workpiece profile $W_{result}$). In this specific example, after four iterations, the final shape of the workpiece (Figure 57.d) is similar to the desired shape (Figure 57.a) with an accuracy of 98.2%.

### ***5.1.2. The target workpiece***

In EDM or micro-EDM, the machining gap (or gap) is the designation for the minimum distance at which it is possible for a spark to occur and therefore the closest distance a potential tool can get before machining the workpiece and, incidentally, itself.

Considering the gap, the target workpiece might include features that could theoretically never be machined since they are too far to trigger sparks. Indeed before sparks can reach these areas, other closer areas would trigger sparks before them. If the tool aims to achieve these areas, it will inevitably damage the rest of the target workpiece profile.

Since the target workpiece profile is the end goal that the tool is trying to achieve, it provides the lead metrics that will influence the optimisation of the tool. Therefore it is important to get rid of misleading information such as these unachievable areas. As a consequence, the target workpiece undergoes processing to remove these areas in order to aim towards a more “realistic target workpiece”.

Target workpiece

Realistic target workpiece

Figure 58: Realistic target workpiece processing.

Figure 58 depicts an example of such unachievable area and the respective realistic target workpiece without it. The technique used to generate the realistic target workpiece is an extension of the tool generation technique described further.

From then on, only the realistic target workpiece is used in all computations. However, for simplicity of reading and comprehension, it will be referred to as the target workpiece $W_{target}$ although it is an inaccurate designation.

### *5.1.3. Virtual workpiece profile and tool generation*

The end goal of the optimisation process is to generate a tool that would best produce the target workpiece, but because of the tool wear phenomena this task is not trivial. Nevertheless, the most intuitive starting point is to try the tool that would produce the target workpiece in a situation in which no tool wear is present and act from there.

This simple idea holds both concepts that lie behind the virtual workpiece. As explained in section previously, the virtual workpiece is an image of the target workpiece as well as a model for the tool.

On one hand, it will first mimic the target workpiece profile and adjust itself from there, making it an image of the target workpiece.

On the other hand, it will generate a tool that would reproduce the virtual workpiece itself if no tool wear occurred, making it a model for the tool.

To keep on with the analogy, in metal casting the pattern is a modified version of the desired piece that is used to shape a mould that would reproduce the pattern itself if no solidification shrinkage occurred.

How the virtual workpiece is an evolving image of the tool will be discussed in the next section regarding virtual workpiece adjustment. The focus will be put on how the virtual workpiece generates a tool that would reproduce the virtual workpiece itself in a case where no tool wear occurred.

The generation of such a tool is a 4-step process:

1. From the virtual workpiece, the coordinates of the surface points are retrieved (Figure 59.a. pinpoints 8 points of the surface with a cross marker)
2. For each of these coordinates, a circle whose radius is equal to the machining gap is drawn (The 8 points' respective circles are displayed in Figure 59.a.)
3. The combination of all the surface circles draws an outer margin. This margin brings out the profile to be used for the conjugate tool. (Figure 59.a. shows this profile in a green dashed line)
4. The tool matching the profile is generated (Figure 59.b. depicts the final tool generated).

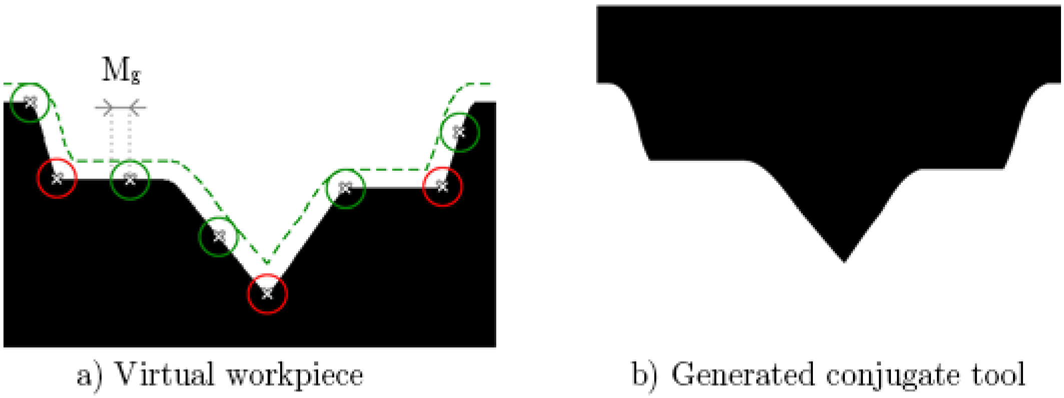

a) Virtual workpiece

b) Generated conjugate tool

Figure 59 : Virtual workpiece and its respective conjugate tool

Using this process, the profile of the tool generated is only influenced by the reachable points of the surface and leaving out the rest. This is illustrated in Figure 59.a) using green circles for influencing points and red circle for noninfluencing points. With that in mind, the tool that would best reproduce the virtual workpiece if no tool wear occurred is obtained.

As mentioned in section 5.1.2, the processing that the target workpiece profile undergoes to remove the unreachable areas is an extension of this technique. The four steps are simply repeated but using the target conjugate tool as a reference this time. This way, the new target workpiece profile generated has a fully reachable surface for a tool that would not wear out, making a version of the target workpiece that can be more reasonably expected. Hence the designation "realistic" target profile.

### 5.1.4. The error measure, ε

The end quality of the tool can only be assessed by analysing on the workpiece side by analysing the resulting workpiece $W_{result}$ in comparison to the target workpiece $W_{target}$.

However, the wear simulation uses a voxel representation embedded in an octree structure that is not convenient for comparison. While Boolean operations between octrees are implementable, it is not straightforward to compare two voxel octrees. As a consequence, another representation is used for this purpose: the matrix representation. Adding up to three possible representations for one entity each with their own purpose:

- Voxel representation for computational efficiency with high resolution during the wear simulation.
- Bitmap representation for user interpretability.
- Matrix representation for comparisons and measurements.

Algorithms were designed to convert one representation to another in a bijective way. It is important to know that the resolution of the simulation is defined by the size of the smallest leaf in the voxel tree in µm/voxel. This smallest leaf is the equivalent of one pixel in the bitmap representation which transpose to one matrix element in the matrix representation as displayed in Figure 62Figure 60. This way the resolution is maintained throughout the conversion process (X µm/voxel = X µm/pixel = X µm/element) and the matrix representation makes measurements convenient.

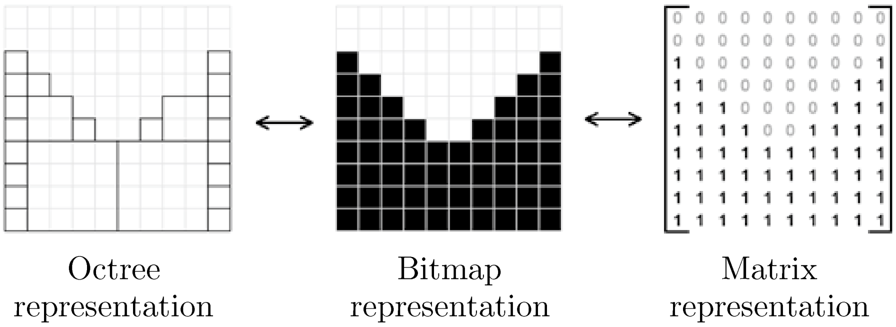

$$\begin{bmatrix} 0&0&0&0&0&0&0&0&0&0\\ 0&0&0&0&0&0&0&0&0&0\\ 1&0&0&0&0&0&0&0&0&1\\ 1&1&0&0&0&0&0&0&1&1\\ 1&1&1&0&0&0&0&1&1&1\\ 1&1&1&1&0&0&1&1&1&1\\ 1&1&1&1&1&1&1&1&1&1\\ 1&1&1&1&1&1&1&1&1&1\\ 1&1&1&1&1&1&1&1&1&1\\ 1&1&1&1&1&1&1&1&1&1 \end{bmatrix}$$

Octree representation ⟷ Bitmap representation ⟷ Matrix representation

Figure 60: Conversion between bitmap image and 2D Boolean matrix.

At the end of each iteration, the voxel representations of the target workpiece $W_{target}$ and the resulting workpiece $W_{result}$ are converted to matrices. The error matrix $\varepsilon$ is then computed by doing the matrix difference between the matrix of the target workpiece $W_{target}$ and the matrix of the resulting workpiece, $W_{result}$. The error measure matrix $\varepsilon$ is the result of a difference operation ($\varepsilon = W_{target} - W_{result}$) as described in Table 33.

Table 33: Table of truth of the 2D matrix difference (X=A-B)

| **A** | **B** | **X** |
|---|---|---|
| 0 | 0 | 0 |
| 0 | 1 | -1 |
| 1 | 0 | 1 |
| 1 | 1 | 0 |

This computation outputs two distinctive areas:

- Positive area: represents the excess of volume removed.
- Negative area: represents the lack of volume removed.

It is important to make this distinction for corrective purpose. Indeed, these areas pinpoint the locations where the tool was under/over effective, as described in Figure 61. With this kind of information, it is possible to modify the virtual workpiece and, consequently, the tool in order to compensate for its lack or excess of material removal. Analytics on the mismatch matrix also give valuable information regarding the advancement of the optimisation process.

### *5.1.5. Optimisation of the virtual workpiece profile*

Based on the assessed difference between the target workpiece profile and the result of an iteration, the optimisation objective is to make modifications on the virtual workpiece profile $W_{virtual}$ so that the virtual tool profile $T_{virtual}$, generated in the next iteration, reduces the difference.

The shape corrective function to apply to the virtual workpiece is computed by taking the vertical summation of each column of the mismatch matrix (Figure 62). The resulting discrete function represents the vertical difference between the objective and the current result. Positive values referring to an excess of removal, and negative values referring to a lack of removal.

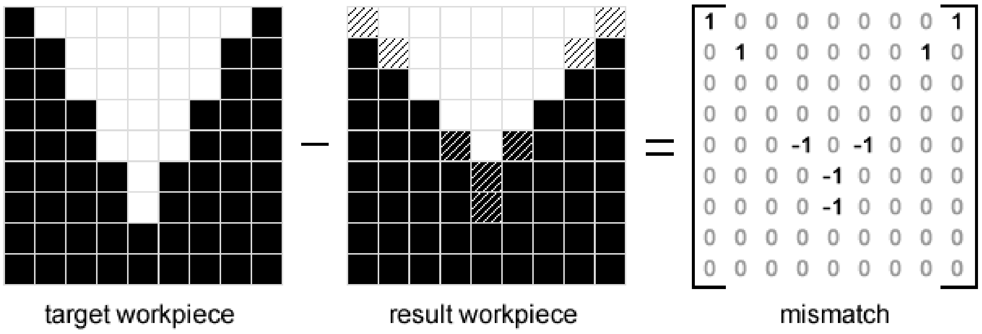

Figure 61: Computation of the mismatch matrix.

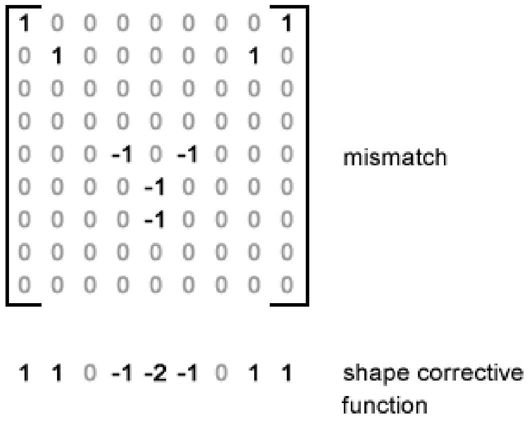

Figure 62: Computation of the shape corrective function.

The shape corrective function is then applied onto the surface of the virtual workpiece, whose shape should evolve to improve the efficiency of the next tool conjugate generated, as described in Figure 56.

Looking to compensate the difference from a vertical point of view is simpler for data processing but also relevant in the context of die-sinking EDM, because the movement of the tool usually is restricted to the vertical axis and thus most interactions happen in this direction.

It should also be mentioned that the shape corrective function is altered by the wear ratio in order to take into account the future expected wear on the tool, and therefore improve the efficiency of each iteration of shape the optimisation process.

In cases of excess of volume to be removed, following approaches developed for drilling and EDM milling, one could suggest that the shape corrective factor obtained for each vertical summation should be altered by the wear ratio.

The wear ratio is defined by the ratio between the wear occurring on the tool electrode and the wear occurring on the workpiece, which for the simulation would be equivalent to the ratio between the Tool Crater Volume and the Workpiece Crater Volume.

### *5.1.6. Experiments and discussion*

In order to demonstrate the viability of the present tool shape optimisation method, three different targeted profiles have been used.

The following parameters were used for all simulations:

- Machining gap: 5 μm
- Tool wear ratio : TWR = 0.5

To achieve a tool wear ratio of 0.5, the volume ratio is defined by the parameters of the craters which apply respectively on the workpiece and the tool as follows:

- Workpiece: crater radius = 3.00μm and crater depth: 2.25μm.
- Tool: crater radius = 2.25 μm and crater depth = 1.50 μm.

The three different target profiles tested are defined as follows:

1. Circle (Figure 64.a): 80 µm radius and 80 µm deep
2. Isosceles triangle (Figure 65.a): 160 µm wide and 80 µm deep
3. Rectangle (Figure 66.a): 160 µm wide and 80 µm deep

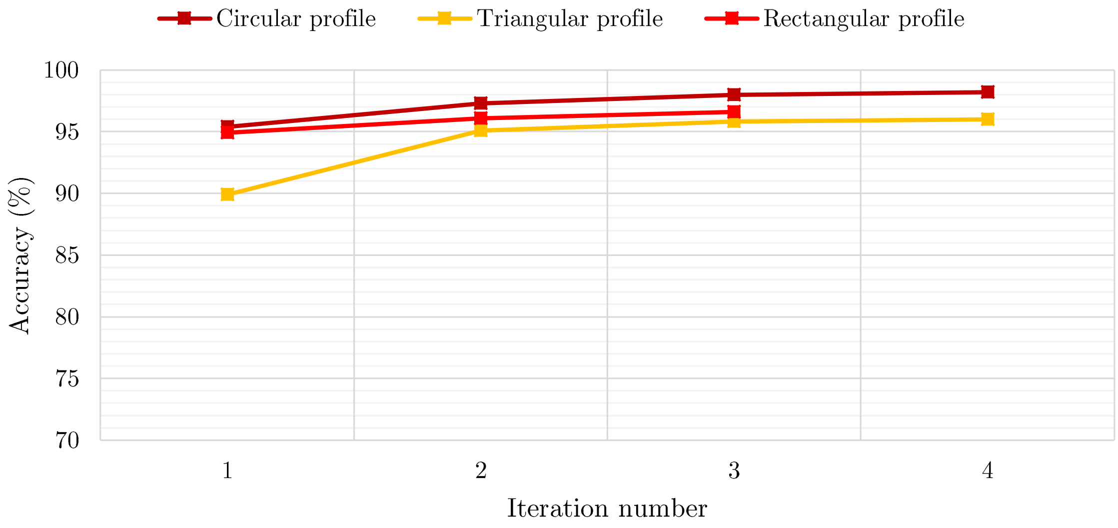

Figure 63: Accuracy of each iteration during the optimisation process for all three target profiles

Figure 63 represents the evolution of the accuracy for each iteration until the process stop. The accuracy is the measure of the overall completeness of the machining in regard to the objective profile. This metric stabilizes after a few iterations for each tests subjects and the process stops when accuracy's progression over one iteration becomes less than 0.5%. It means that the following optimisation iterations will not improve the tool significantly anymore. Therefore, the optimisation process stops and the tool giving the highest accuracy is kept as the optimal tool.

As can be seen in Table 34, in all cases the optimal tool was obtained after 3 to 4 iterations with an accuracy rate of over 96%. This certifies that the optimal tools are very effective given that the remaining mismatch is mostly due to the imperfection of craters in regard to the target geometry as shown in Figure 64.c), Figure 65.c)Figure 66.c).

Table 34: Optimisation process data for all three target profiles.

| | **Iteration number of optimal tool** | **Accuracy of optimal workpiece result (%)** | **Mean duration of optimisation loops (s)** |
|---|---|---|---|
| Circular profile | 4 | 98.2 | 52 |
| Triangular profile | 4 | 96.0 | 41 |
| Rectangular profile | 3 | 96.6 | 66 |

It is important to notice that the cavity of the rectangular target profile is significantly bigger than the others, with the cavity of the triangular profile being the smallest. This means that there will be more material to remove. As a consequence, the duration of each iteration for the optimisation of the rectangular profile are the longest and those of the triangular profile are the shortest.

Figure 64, Figure 65 and Figure 66 represent the important geometries of the optimisation process respectively for the circular profile, the triangular profile and the rectangular profile. Figures a) are the geometries of the target profiles while Figures b) are the geometries of the optimal tools resulting from the optimisation process. Finally, Figures c) show the mismatch area remaining from the machining of the optimal tool.

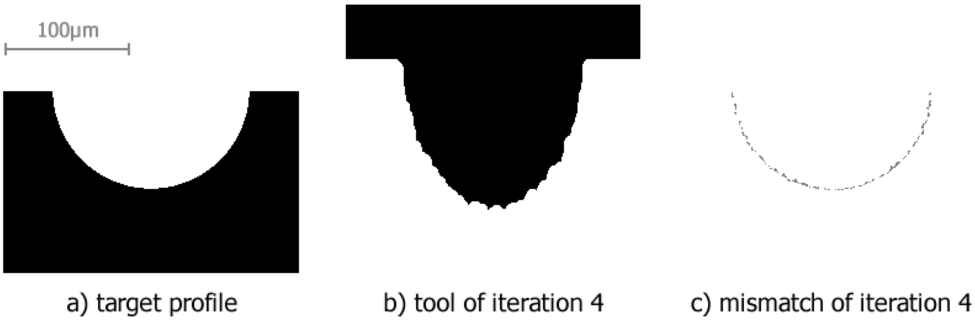

Figure 64: Tool optimisation results for the circular profile.

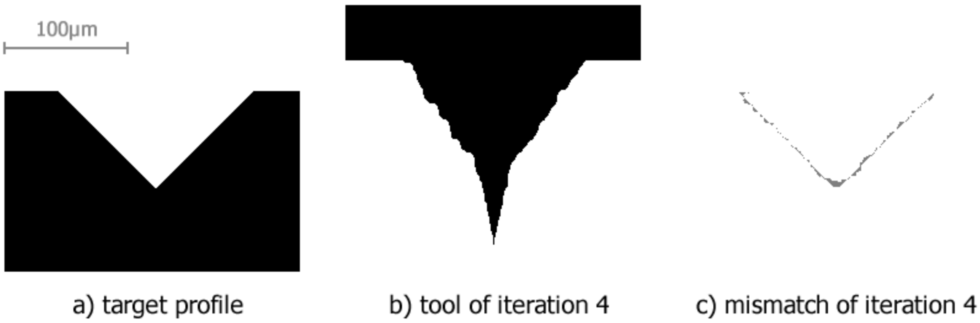

Figure 65: Tool optimisation results for the triangular profile.

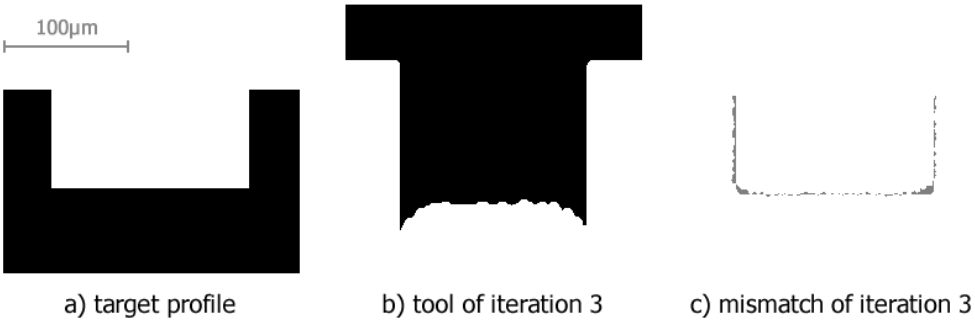

Figure 66: Tool optimisation results for the rectangular profile.

The remaining mismatch on the triangular profile (Figure 65.c) peaks at 5.75 μm around the tip of the isosceles triangle, questioning whether the sharpness objective of the profile is achievable. This highlights the fact that not all target profiles are achievable with the die-sinking EDM process, a fortiori using a single tool.

The final mismatch can be considered as a machinability check metric that indicates to designers if the resulting workpiece will match their dimension tolerances. Consequently, this can be used as a designer's tool to check if the EDM process is adequate for the production of specific new features or, as mentioned previously, in the middle of a manufacturing chain using scans of produced components to check if a re-configurability of the EDM process is required and if it could lead to the desired features' tolerances.

In order to test the limits of the tool shape optimisation method, the same three target profiles underwent the tool optimisation method with three different machining gaps:

- Machining gap: 5 μm, 20 μm and 40 μm

Figure 67, Figure 68, Figure 69 represent the evolution of accuracy during the optimisation process for all three profiles at each machining gap.

What is worth highlighting here is that, except for the circular profile, the machining gap significantly worsens the accuracy of the optimal tool as it gets bigger. This is due to the pointier shapes of the triangular and rectangular profiles. These shapes are more difficult to acquire when the machining gap increases because the vertical compensation applied to the virtual tool is then nullified by the large machining gap as the conjugate tool is generated. As shown in Figure 68, a significant compensation applied to the virtual workpiece does not affect the tool much in return.

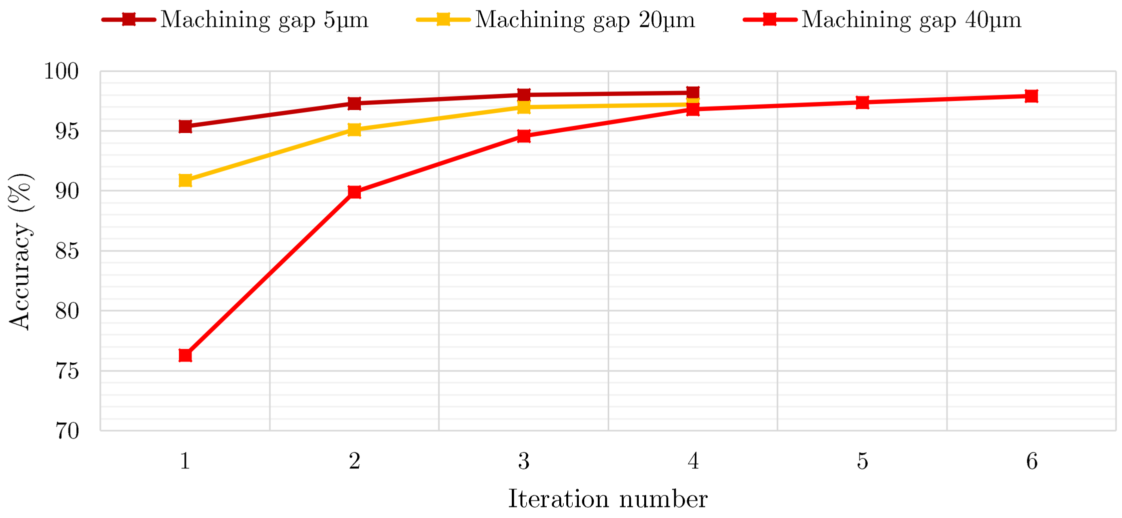

Figure 67 : Evolution of accuracy during the optimisation process of the circular profile for different machining gaps.

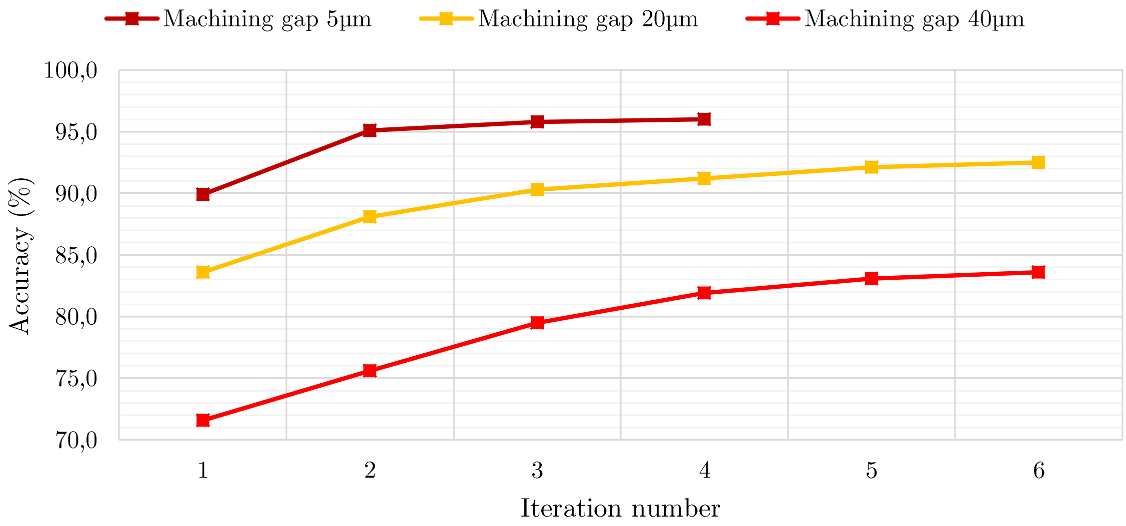

Figure 68 : Evolution of accuracy during the optimisation process of the triangular profile for different machining gaps.

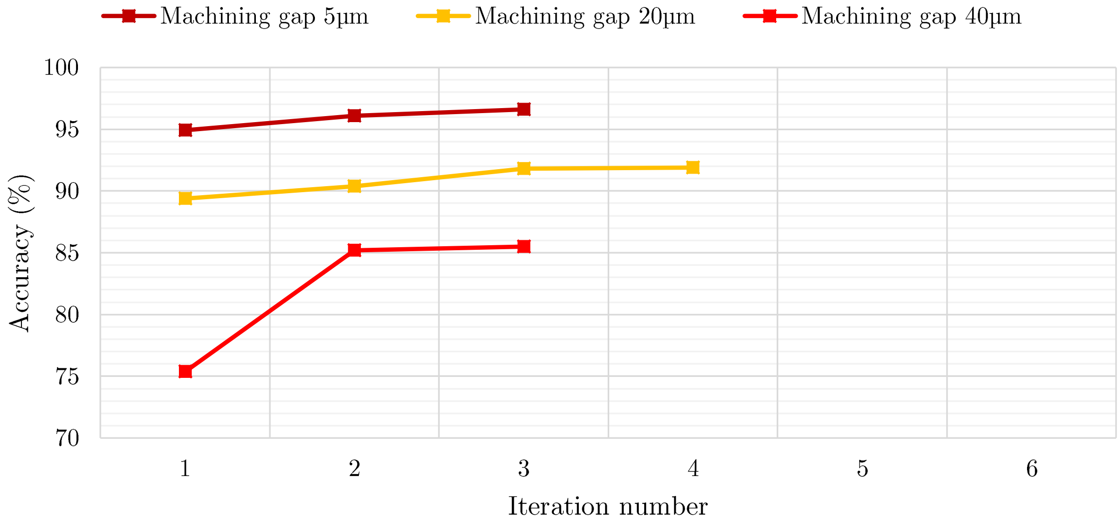

Figure 69 : Evolution of accuracy during the optimisation process of the rectangular profile for different machining gaps.

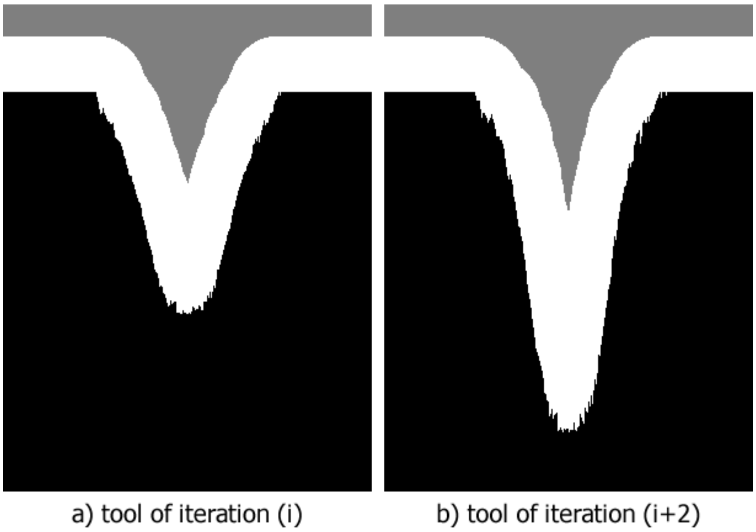
a) tool of iteration (i)
b) tool of iteration (i+2)

Figure 70 : Virtual workpiece and its respective tool at different iterations with a machining gap value of 40 µm.

## 5.2. Generalization using machine learning

### *5.2.1. Introduction*

Following the work presented in the previous section, the feasibility of training an artificial neural network (ANN) is studied here. The objective is to build a predictive algorithm able to output an optimal tool shape from the desired profile and machining parameters.

While the iterative method previously presented works well in providing an optimal tool shape, it has only been implemented in a two-dimensional setting. The three-dimensional version is significantly longer in providing with the optimal tool shape: dozens of hours could be required to perform a single optimisation.

The idea behind using ANN to propose optimal tool shapes is to be able to train it once and for all for a specific set of shapes and parameters and using it in the case of unknown shapes. Figure 71 provides with the overview of the proposed work.

The algorithm will try and maximize its performance P while accomplishing a task T, through learning from experience E.

- Task (T): Predict the optimal virtual workpiece for a target profile.
- Experience (E): A corpus of target profiles with their respective optimal virtual workpieces.
- Performance (P): Prediction accuracy, the relative difference between the predicted virtual workpiece and the actual virtual workpiece obtained through the iterative optimisation, as a percentage.

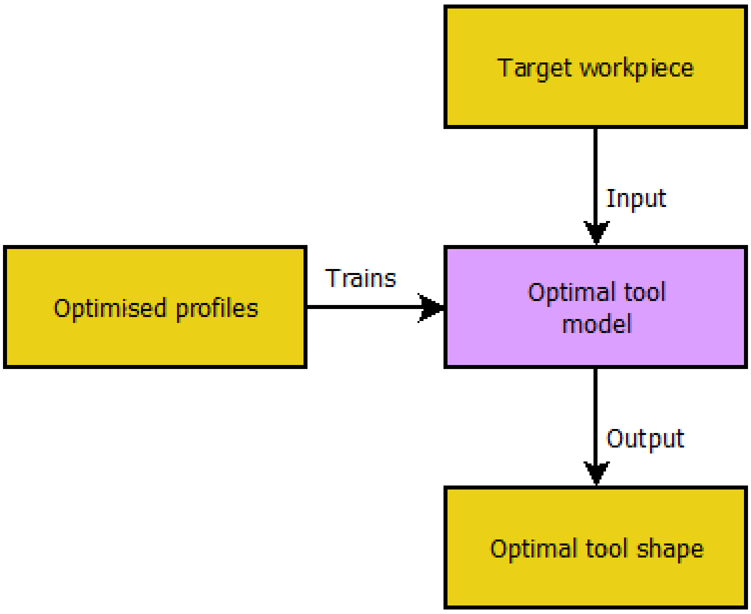

Figure 71: Overview of the relationships between the proposed optimal tool model, its training set, its input and its output.

The first approach is to only consider a specific set of machining parameters and focus on the prediction of optimal tool shapes in the case of a different target workpiece rather than different machining parameters. The reasoning behind it is to first verify that a machine learning method can be used in this simple test case before being extended to a more general environment that would include the machining gap and crater dimensions as input variables for the training of the model.

The machining parameters are therefore constant and their values are tabulated in Table 35.

Table 35: The machining and simulation parameters that are taken as constant during the generation of the data for the machine learning model training.

| **Parameter** | **Value** |
|---|---|
| Machining gap (µm) | 10.0 |
| Workpiece crater radius (µm) | 3.00 |
| Workpiece crater depth (µm) | 2.25 |
| Tool crater radius (µm) | 2.25 |
| Tool crater depth (µm) | 1.50 |
| Resolution (µm/voxel) | 0.5 |

### *5.2.2. Multiplying the training data*

Given the little training set instances available and the requirements when considering the use of a neural network, it is important to look at the problem differently and to redefine the instances the algorithm will train with.

Throughout the optimisation process, modifications regarding virtual workpiece profiles are applied strictly vertically via the Shape Optimisation Function that is based on the mismatch of each iteration. Furthermore, the first mismatch considered is the area of the target profile. This means that the virtual workpiece profile is indirectly a modified version of the target profile. Each point of the target profile can be considered to be individually moved vertically to form the virtual workpiece profile.

Given the point-to-point correlation between the target profile and the virtual workpiece profile, it is possible to redefine the problem: for a given point on the target profile, predict the Y position of the respective point on the virtual workpiece profile. Therefore the predicted optimal virtual workpiece profile is the combination of the predictions of all the points of the optimal workpiece profile from all the points of the target profile.

- Task (T): Predict the position on the optimal virtual workpiece for a point of a target profile.
- Experience (E): A corpus of points from target profiles with their respective counterpart on the optimal virtual workpiece.
- Performance (P): Prediction accuracy, the relative difference between the predicted virtual workpiece position and the actual virtual workpiece position, as a percentage.

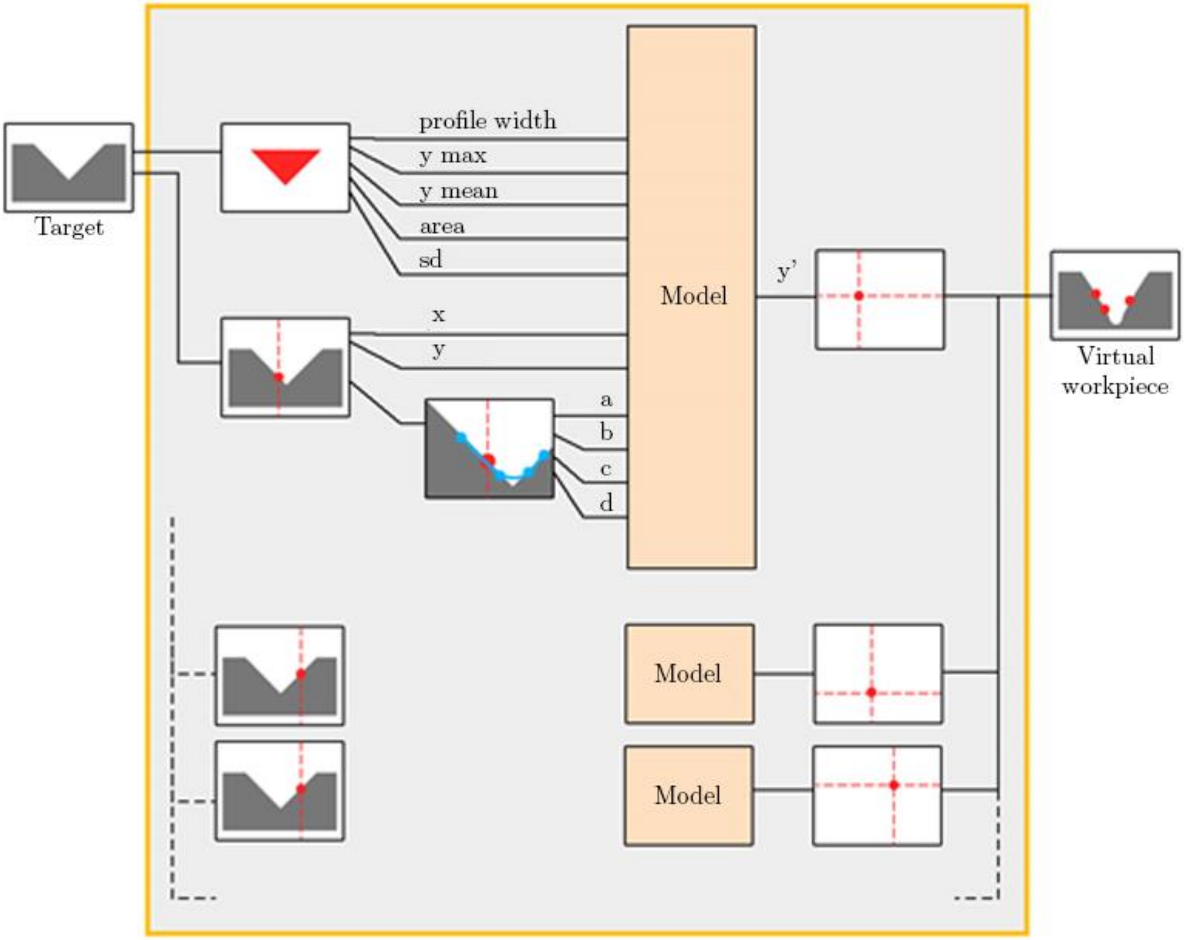

Figure 72: A detailed overview of the machine learning model, its inputs and its output.

Given the maximum sizes of the profiles and the resolution, each test profile will provide up to 600 points as data to work with. With thirty profiles considered (those are displayed in Addendum C), this results in approximatively 18,000 instances to distribute in the following sets:

- The training set (60%): 10,800 instances
- The validation set (20%): 3,600 instances
- The test set (20%): 3,600 instances

### *5.2.3. Feature selection*

Considering that each point is now considered separately from the rest of the profile, every attribute will have as a purpose to give valuable information regarding the environment the given point is in (the whole target profile).

Attributes providing information on the local context (i.e. the point and its surroundings):

- yValue: Y-value of the point on the point on the target workpiece profile (in µm)
- parametricDescription: three of the four parameters describing the third degree Lagrange Interpolating Polynomial (Kudryavtsev & Samarin, 2011) that approximates the neighbourhood of the given point with a window width equal to two machining gaps (Figure 72, in blue). The constant parameter is excluded since the interpolation is centred on the given point, making the constant always equal to 0.

Attributes providing information on the global context (i.e. the target workpiece):

- profileWidth: total width of the target workpiece (in µm)

- profileHeight: total height of the target workpiece (in µm)
- mean: mean Y-value of the target workpiece points (in µm)
- area: total area (or volume in 3D) of the target workpiece (in µm$^2$)
- sd: standard deviation of the Y-values of the target cavity points (in µm)

Attributes providing information on the point relative to the rest of the target cavity:

- xValueRel : X position of the point relative to the rest of the profile (0 being the centre and 1 corresponding to an extremity of the profile)
- yValueRel: Y position of the point relative to the rest of the profile (0 being the base and 1 corresponding to the maximum height of the profile)
- dirToLocalMax: slope towards the closest local maximum
- distToLocalMax: distance to the closest local maximum (in µm)
- equivalents: number of times the target workpiece profile goes through the point's altitude.

Output variable:

- yValuePattern: Y-value of the respective point on the pattern workpiece profile

This results in 14 input attributes and 1 output variable, all of which are continuous real values without any missing data.

### *5.2.4. Model*

#### 5.2.4.1. Model selection

Machine learning has a large variety of models that come with their respective advantages and disadvantages. When it comes to supervised learning for regression models like in our case, there are two types of model that usually perform best: Artificial Neural Networks (ANNs) and Support Vector Machines (SVMs).

It has been decided to use ANNs because they can perform the most complex relationships between inputs and outputs and thus have the potential to give excellent results. However, they are to be used carefully. Indeed, the model complexity of ANNs rises quickly with the number of features, making it slow to train and prone to suffer from multiple local minima. As a consequence, SVMs are usually favoured when dealing with high dimension input vectors. Fortunately, this is not the case presently since only 14 attributes are to be considered.

Furthermore, the simulation tool has been developed in C#. In order to make use of the tool prediction process, it is advantageous that the model can be implemented inside the application itself. However, this language only has a few machine learning frameworks compared to other more computationally oriented languages like Python, R or Matlab. None of these available machine learning frameworks have a good support for SVMs, whereas the C# framework Encog (Heaton, Artificial intelligence for humans, volume 1: Fundamental algorithms, 2013) supports a large variety of neural network algorithms making it possible to optimize the performances of the model with already available features.

As a consequence, ANN has been deemed the most adequate candidate model in this context.

### 5.2.4.2. Model configuration

One of the crucial steps when using ANNs is determining the model's configuration, meaning choosing how many hidden layers and hidden neurons the networks should have. This task is very complex and has a huge impact on the performance of the network. If the hidden structure is too complex, the model will take long to train, will be prone to overfitting and will have a hard time dealing with local minima. If the hidden structure is too simple, the model will not learn the problem (underfitting).

The Incremental Pruning technique (Cassandra, Littman, & Zhang, 1997) was implemented to determine the hidden structure to use. The objective of incremental pruning is to figure out the most promising hidden layer configuration out of a variety of potential configurations.

First, some basic rules of thumb were used to determine the reasonable ranges for the number of hidden layers and their ranges of neurons. Then every network configuration was tested 3 times for 300 iterations, then the five networks giving the best scores were saved. Finally it will only take on the network with the simplest configuration of all for training efficiency as well as overfitting prevention.

The most promising model in this case turned out to be a network with a single hidden layer composed of 14 neurons. Now that the model configuration is set, the network is ready to be trained.

#### 5.2.4.3. Training criteria

The method used for training is the resilient backpropagation algorithm (RPROP) for feedforward ANN. RPROP is one of the best general purpose training methods for neural network and have the advantage of having no parameters to tune (Heaton, Introduction to the math of neural networks, 2011).

In order to reach the minimum error possible, the training method makes use of the cross-validation set. While iterating through the training set and adjusting the weights of the network accordingly to the RPROP method, the algorithm computes the error of the network on the validation set. As long as the validation error keeps improving by a certain amount over multiple iterations, the training goes on. This method ensures that the training continues as long as it is effective even on unseen data while preventing overfitting. Indeed, overfitting occurs when the model starts fitting the training data too well and doesn't generalize well anymore on unseen data (the cross-validation set).

#### 5.2.4.4. Performances

Once it is trained, the model performance can be evaluated with various metrics on the test set. Here are the different metrics to be considered.

- Mean Absolute Error (MAE) gives the mean absolute error of the predicted values.
- Coefficient of determination ($R^2$) indicates how well the model predicts the values.

Table 36: Evaluation metrics for point altitude prediction.

| **Metric** | **Value** |
|---|---|
| $R^2$ | 0.957 |
| MAE (µm) | 3.88 |

The values present in Table 36 mean that, on average, each predicted point of the pattern cavity is 3.88 µm away from its actual position (given by the iterative optimisation process.

Although these error measures provide insight on how well the model can predict the pattern cavity, the end goal is the performance of the resulting tool. In order to evaluate the performance of the predicted tool the accuracy metric described in section 5.1.1, Equation (59), is used. By simulating the micro-EDM machining of the predicted tool and the actual optimised tool, it is possible to compare their accuracy and measure the Mean Absolute Error between them.

Table 37: Evaluation metrics for the predicted tools.

| **Metric** | **Value** |
|---|---|
| Training set accuracy MAE (%) | 2.06 |
| Test set accuracy MAE (%) | 3.06 |

The figures in Table 37 indicate that, on average, the predicted tool for a new target workpiece would be 3.06% less accurate than the actual optimized tool.

Also, it is good to know that, on average, the predicted tool is as accurate as an optimised tool that would be half way through the iterative optimisation process.

In other words, the prediction does half the work of the optimisation process. One way to make use of the prediction model is to start the tool optimisation process with the predicted tool right from the beginning. Doing so will save a considerable amount of time, especially if 3D shapes were to be involved.

### *5.2.5. An extended dataset*

#### 5.2.5.1. Data generation

After having demonstrated the viability of the use of a Multilayer Perceptron algorithm in the successful prediction of optimal tool shapes, it is proposed to extend the method to various combinations of machining parameters.

The previous sections focused on applying machine learning methods for a single set of machining conditions while focusing on varying the target workpiece profiles. The present section will explore the possibility of varying other parameters and studying the change on the method's accuracy.

In order to propose a sufficient amount of data to obtain robust results, a certain number of tool optimisations were performed using a large variety of target profiles, machining gaps and crater dimensions. Those were:

- Target profiles: 30 shapes (shown in addendum C).
- Machining gaps: 4 values (5 µm, 10 µm, 15 µm, 20 µ,).
- Crater dimensions: 45 combinations (Table 38).

The crater dimensions used were generated starting with five values for the workpiece crater radii: 2, 2.5, 3, 3.5 and 4 µm.

Each of those is associated with three crater depth generated from three values called ratios $\gamma$: 1, 1.5 and 2 such as:

$$\gamma = \frac{R_w}{D_w} \tag{60}$$

Where $R_e$ and $D_e$ are respectively the radius and depth of the craters for the tool ($e$=$t$) and the workpiece ($e$=$w$).

The dimensions for the tool crater radii and depth are found using the following system of equations:

$$\begin{cases} \gamma = \dfrac{R_w}{D_w} = \dfrac{R_t}{D_t} \\ \beta = \dfrac{V_t}{V_w} \end{cases} \tag{61}$$

Where $\beta$ is the tool wear ratio which is here the ratio between the volume of the crater of the tool and the area (or volume in the 3D case) of a crater of the workpiece. Values for $\beta$ were chosen as 1.5, 1 and 0.5 to cover both cases related to the polarity of the generator (tool is worn more and tool is worn less). However usual empirical values for $\beta$ in micro-EDM are around 0.15 and 0.25. Higher values were used to quickly obtain noticeable tool wear during the simulation.

Which yields:

$$\begin{cases} R_t = \sqrt{\beta} R_w \\ D_t = \dfrac{\sqrt{\beta} R_w}{\gamma} \end{cases} \tag{62}$$

For information, the three-dimensional equivalent of this system is:

$$\begin{cases} R_t = \sqrt[3]{\beta} R_w \\ D_t = \dfrac{\sqrt[3]{\beta} R_w}{\gamma} \end{cases} \tag{63}$$

Table 38: Crater dimensions combinations used for the generation of the training data.

| | **Workpiece crater** | | **Tool crater** | | | |
|---|---|---|---|---|---|---|
| **N°** | **Radius (µm)** | **Depth (µm)** | **Radius (µm)** | **Depth (µm)** | **Crater ratio** | **TWR** |
| 1 | 2 | 2.00 | 2.44 | 2.44 | 1 | 1.5 |
| 2 | 2 | 2.00 | 2.00 | 2.00 | 1 | 1 |
| 3 | 2 | 2.00 | 1.41 | 1.41 | 1 | 0.5 |
| 4 | 2 | 1.33 | 2.44 | 1.63 | 1.5 | 1.5 |
| 5 | 2 | 1.33 | 2.00 | 1.33 | 1.5 | 1 |
| 6 | 2 | 1.33 | 1.41 | 0.943 | 1.5 | 0.5 |
| 7 | 2 | 1.00 | 2.44 | 1.22 | 2 | 1.5 |
| 8 | 2 | 1.00 | 2.00 | 1.00 | 2 | 1 |
| 9 | 2 | 1.00 | 1.41 | 0.707 | 2 | 0.5 |
| 10 | 2.5 | 2.50 | 3.06 | 3.06 | 1 | 1.5 |
| 11 | 2.5 | 2.50 | 2.50 | 2.50 | 1 | 1 |
| 12 | 2.5 | 2.50 | 1.76 | 1.76 | 1 | 0.5 |
| 13 | 2.5 | 1.66 | 3.06 | 2.04 | 1.5 | 1.5 |
| 14 | 2.5 | 1.66 | 2.50 | 1.66 | 1.5 | 1 |
| 15 | 2.5 | 1.66 | 1.76 | 1.17 | 1.5 | 0.5 |
| 16 | 2.5 | 1.25 | 3.06 | 1.53 | 2 | 1.5 |
| 17 | 2.5 | 1.25 | 2.50 | 1.25 | 2 | 1 |
| 18 | 2.5 | 1.25 | 1.76 | 0.884 | 2 | 0.5 |
| 19 | 3 | 3.00 | 3.67 | 3.67 | 1 | 1.5 |
| 20 | 3 | 3.00 | 3.00 | 3.00 | 1 | 1 |

|  | Workpiece crater |  | Tool crater |  |  |  |
|---|---|---|---|---|---|---|
| N° | Radius (µm) | Depth (µm) | Radius (µm) | Depth (µm) | Crater ratio | TWR |
| 21 | 3 | 3.00 | 2.12 | 2.12 | 1 | 0.5 |
| 22 | 3 | 2.00 | 3.67 | 2.44 | 1.5 | 1.5 |
| 23 | 3 | 2.00 | 3.00 | 2.00 | 1.5 | 1 |
| 24 | 3 | 2.00 | 2.12 | 1.41 | 1.5 | 0.5 |
| 25 | 3 | 1.50 | 3.67 | 1.83 | 2 | 1.5 |
| 26 | 3 | 1.50 | 3.00 | 1.50 | 2 | 1 |
| 27 | 3 | 1.50 | 2.12 | 1.06 | 2 | 0.5 |
| 28 | 3.5 | 3.50 | 4.28 | 4.28 | 1 | 1.5 |
| 29 | 3.5 | 3.50 | 3.50 | 3.50 | 1 | 1 |
| 30 | 3.5 | 3.50 | 2.47 | 2.47 | 1 | 0.5 |
| 31 | 3.5 | 2.33 | 4.28 | 2.85 | 1.5 | 1.5 |
| 32 | 3.5 | 2.33 | 3.50 | 2.33 | 1.5 | 1 |
| 33 | 3.5 | 2.33 | 2.47 | 1.65 | 1.5 | 0.5 |
| 34 | 3.5 | 1.75 | 4.28 | 2.14 | 2 | 1.5 |
| 35 | 3.5 | 1.75 | 3.50 | 1.75 | 2 | 1 |
| 36 | 3.5 | 1.75 | 2.47 | 1.23 | 2 | 0.5 |
| 37 | 4 | 4.00 | 4.89 | 4.89 | 1 | 1.5 |
| 38 | 4 | 4.00 | 4.00 | 4.00 | 1 | 1 |
| 39 | 4 | 4.00 | 2.82 | 2.82 | 1 | 0.5 |
| 40 | 4 | 2.67 | 4.89 | 3.26 | 1.5 | 1.5 |
| 41 | 4 | 2.67 | 4.00 | 2.66 | 1.5 | 1 |
| 42 | 4 | 2.67 | 2.82 | 1.88 | 1.5 | 0.5 |
| 43 | 4 | 2.00 | 4.89 | 2.44 | 2 | 1.5 |
| 44 | 4 | 2.00 | 4.00 | 2.00 | 2 | 1 |
| 45 | 4 | 2.00 | 2.82 | 1.41 | 2 | 0.5 |

Those 45 combinations, associated with the 4 machining gap values and 30 different shapes lead to a total number of optimisations of 5,800. Those were accomplished in under 12 days using two different computers running the optimisations concurrently.

#### 5.2.5.2. Training the model

Similarly to what has been described in sections 5.2.1 through 5.2.4, the model has been similarly generated and trained. The available data was divided into:

- A training set (60%): 3,480 optimisations (approximatively 1 million instances).
- A cross-validation set (20%): 1,160 optimisations (approximatively 350,000 instances).
- Test set (20%): 1,160 optimisations (approximatively 350,000 instances).

Once again an Artificial Neural Network was trained using the resilient backpropagation algorithm described previously. The main difference here is the addition of a few input variables: the machining gap and the crater dimensions. As a result the input parameters have a count of 19 for one output parameter.

#### 5.2.5.3. The test set

Once the training of the model achieved, it is submitted to the test set. A first result yields the following metrics (Table 39)

Table 39: Evaluation metrics for point altitude prediction for the extended dataset.

| **Metric** | **Value** |
|---|---|
| $R^2$ | 0.931 |
| MAE (µm) | 4.02 |

As could be expected, those error values are greater than in the case of the limited test set (A $R^2$ of 0.931 against 0.957 and a mean absolute error of 4.02 µm against 3.88 µm).

Once again what is actually of interest is to compare the performances of a tool generated through the iterative process against one generated by the ANN model. Due to the huge size of the test set, not all of the tools generated by the ANN could be tested individually against their iterative counterparts. A selection of 20 of them was made across a broad range of parameters. Those are tabulated in Table 40.

Table 40: Test set optimisations used for direct comparison of the achieved workpiece results.

| **N°** | **Shape N°** | **Machining gap (µm)** | $\beta$ | $\gamma$ | $R_w$ **(µm)** |
|---|---|---|---|---|---|
| 1 | 9 | 20 | 0.5 | 1 | 2 |
| 2 | 6 | 15 | 0.5 | 2 | 3.5 |
| 3 | 4 | 10 | 1.5 | 1.5 | 3.5 |
| 4 | 29 | 15 | 0.5 | 1.5 | 2 |
| 5 | 24 | 5 | 1 | 1.5 | 4 |
| 6 | 2 | 10 | 1.5 | 1.5 | 2.5 |
| 7 | 19 | 5 | 0.5 | 1 | 3 |
| 8 | 14 | 10 | 0.5 | 2 | 4 |
| 9 | 18 | 15 | 0.5 | 1 | 3.5 |
| 10 | 12 | 10 | 0.5 | 2 | 2.5 |
| 11 | 10 | 5 | 0.5 | 2 | 3.5 |
| 12 | 1 | 5 | 1.5 | 2 | 2.5 |
| 13 | 16 | 20 | 1.5 | 1 | 2.5 |

| **N°** | **Shape N°** | **Machining gap (µm)** | $\beta$ | $\gamma$ | $R_w$ **(µm)** |
|---|---|---|---|---|---|
| 14 | 17 | 10 | 1.5 | 2 | 4 |
| 15 | 13 | 20 | 1 | 1.5 | 3.5 |
| 16 | 15 | 5 | 0.5 | 2 | 3 |
| 17 | 2 | 15 | 0.5 | 1 | 4 |
| 18 | 20 | 20 | 1 | 1.5 | 2 |
| 19 | 22 | 5 | 0.5 | 2 | 2.5 |
| 20 | 27 | 15 | 1.5 | 2 | 4 |

The various accuracies of the two methods (iterative and machine learning) are given in Table 41 and the mean, variance and standard deviation of the differences are given in Table 42.

Once again, the accuracy of the method based on machine learning is worse than of the iterative one. However, considering the much larger range in terms of number of parameters, these result are quite acceptable. In order to provide with a visual representation of those errors, an example of optimisation using the iterative method and its equivalent with the machine learning method are depicted in Figure 73.

Table 41: Comparison of the accuracies of the machine learning method and the iterative method.

| N° | Accuracy Machine Learning (%) | Accuracy Iterative (%) | Difference (%) |
|---|---|---|---|
| 1 | 45.5 | 54.2 | 8.63 |
| 2 | 34.0 | 40.4 | 6.32 |
| 3 | 16.9 | 23.7 | 6.81 |
| 4 | 37.9 | 44.4 | 6.51 |
| 5 | 57.5 | 60.3 | 2.81 |
| 6 | 82.4 | 85.4 | 3.08 |
| 7 | 66.5 | 73.6 | 7.09 |
| 8 | 47.8 | 52.2 | 4.42 |
| 9 | 62.9 | 67.6 | 4.71 |
| 10 | 46.2 | 52.4 | 6.16 |
| 11 | 48.3 | 57.8 | 9.49 |
| 12 | 74.3 | 82.0 | 7.68 |
| 13 | 17.1 | 24.9 | 7.83 |
| 14 | 32.8 | 34.5 | 1.62 |
| 15 | 63.3 | 69.9 | 6.62 |
| 16 | 35.7 | 43.3 | 7.61 |
| 17 | 65.5 | 67.2 | 1.74 |
| 18 | 27.0 | 33.0 | 5.94 |
| 19 | 21.6 | 26.1 | 4.52 |
| 20 | 59.1 | 64.8 | 5.62 |

Table 42: Statistical properties of the accuracy differences between the machine learning and iterative methods for the twenty optimisations chosen.

| **Measure** | **Value** |
|---|---|
| Mean | 5.76 |
| Variance | 4.60 |
| Standard deviation | 2.14 |

Target workpiece

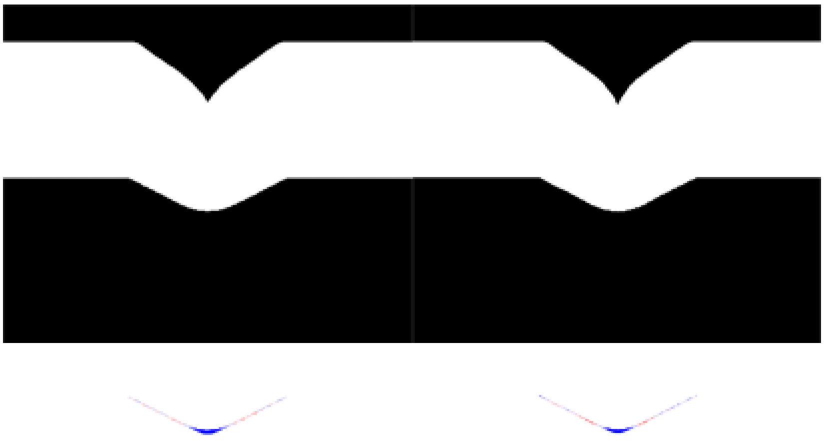

Machine learning method

Iterative method

Figure 73: Visual side-by-side comparison of the machine learning method and the iterative method for test optimisation number 9.

## 5.3. Synthesis

Chapter five dealt with two distinct elements. The first was the development of a tool optimisation process based on an iterative loop method. Comparing the differences between the target profile and the actual profile obtained, the algorithm modified the tool used iteratively until a satisfactory error measure was achieved.

In addition to converging quite rapidly, the algorithm was found to be quite efficient achieving high accuracy values (in the range of 95%). Shapes with sharp angles perform slightly less than shapes without but still constitute a good approximation of an optimal tool. If needed, a second tool could be designed to act as a finishing tool to remove any residual material remaining.

This method was developed with the idea that it would be implemented in three dimensions. However, considering the length of a single 3D simulation, around 2 hours for a 100 µm deep machining, a single optimisation process that could take 4, 5 or more iterations could be potentially lengthy.

From this emerged the idea to train a neural network using the optimized profiles from the iterative tool in order to limit the number of optimisations to be done and instead use a predictive neural network model that would be able to output directly an optimal tool shape.

A wide variety of shapes, crater dimensions and machining gaps were used to train a neural network. This network was tested against the iterative method and, while slightly inferior, it offers comparable results nearly instantaneously (in a few seconds). It is of note that the values used for the tool wear ratio weren't specific to the usual micro-EDM empirical values and that future works might want to refocus on values around 0.15 for β.

As of now, the optimization of the tool is deeply linked to the simulation since it is at the basis of the iterative optimization method. As a result, the performance of the optimized tool shapes in reality is dependent on the ability of the simulation tool to accurately predict a machining process.

Experimental validation needs to be conducted for optimized tool shapes using a broad range of parameters and shapes. The validation would be based on the measure of the deviation of resulting shapes between the simulation using the optimal tool and the experiment using the same optimized tool.

# Chapter 6

# Synthesis, conclusions and perspectives

## 6.1. Introduction

The present chapter acts as the conclusion of the thesis, it focuses on underlining the main contributions of the research that has been made. It also provides with suggestions towards future work.

## 6.2. Conclusions

After having studied the various variant of micro-EDM in existence, a gap in knowledge in die-sinking micro-EDM has been identified. Other variants could be considered significantly more mature. Proven methods exist in micro-EDM milling and micro-EDM drilling to counteract the negative effects linked to the phenomenon known as tool wear. Few attempts have been made in the context of die-sinking micro-EDM in comparison.

Die-sinking micro-EDM has some inherent advantages such as its ability to machine complex 3D geometries and an excellent surface finish, greater than in micro-EDM milling.

If a complete, precise and fast optimisation tool could be developed, this specific process might gain in competitiveness against other variants of micro-EDM.

This constatation is at the basis of the present work.

The complexities and, sometimes, inadequacies of physics-based models make them hard to implement when often hundreds of thousands of iterations are needed for a complete simulation. A geometrical approach in line with previous works has been preferred to the more complex and computationally intensive physics-based simulations.

However the various geometrical options explored in the literature have some drawbacks that make it worthwhile to explore alternative options.

The first part of the thesis presented a geometrical approach towards the numerical simulation of the die-sinking micro-EDM process. Two new methods were presented: a simulation tool based on NURBS and another one based on voxels embedded in a tree data structure (Octrees).

Both of the methods share the same underlying concept: an iterative, crater-by-crater, process that uses conditions based on the machining gap and the objective depth to perform the simulated machining. While the implementation of the various functions were different due to the opposed nature of the geometrical models (surfacic versus volumetric), the idea behind them remains identical.

A first approach at experimental validation has shown that these simple geometrical implementations are sufficient to provide an accurate estimate of the results obtained on the workpiece and, more importantly here, the wear on the tool.

It was shown that, while both methods performed well when limiting considerations to accuracy, the voxels method is significantly faster and the focus was shifted on it.

As opposed to previous methods developed in the past, the voxels-based method has been made memory-efficient through the incorporation into an octree data structure. This enables fast computations that take advantage of the hierarchical structure for quick convergence to a solution. Additionally the savings in terms of memory led to the possibility of using a high resolution for the discretisation of the various volumes into voxels. A resolution of four voxels per micron was used previously but can be easily increased.

Further validation of the voxels method has shown that it remained accurate for a broad range of machining parameters using as its inputs the crater dimensions extracted from experimental roughness data using a linear regression model built with simulation data and machine learning methods.

The fact that numerous different micro-EDM machines are in existence is quite a problem when trying to optimise a process in a general way. While most of the work has relied on a specific machine, the simulation tool takes as input the dimensions of the craters and the expected machining gap therefore limiting its dependency on a single, specific machine.

The relationship between the machining gap and the current and voltage between the two electrodes during the machining process has been studied in an effort to develop models applicable to any kind of machine.

Additionally, efforts were made to develop relationships between the roughness of a feature obtained by micro-EDM and the crater dimensions. Two relationships, one for the crater radius and another for the crater depth were obtained with data from the simulation. The use of those relationships to choose the input values of the simulation of experimental conditions has given simulated shapes that deviate by 4 to 9% with the experimental shapes. These error measures are sufficiently low to consider that the simulation gives a good global approximation of the final shape when using the crater dimension models as inputs.

The third part of the thesis focused on the optimisation of the tool shape itself. The results issued from the simulation tool were used in an iterative optimisation loop that would modify the shape of the tool in order to minimize the gap between the target profile and the profile actually obtained.

The method developed proved to be converging rapidly around an optimal tool shape in a few iterations (usually less than five) and for a broad range of shapes.

The fourth part of the thesis developed the idea that the optimisation process could be used to train a multilayer perceptron neural network in order to directly obtain optimal tool shapes for profiles that are unknown to it. This idea stems from the fact that the optimisation tool was developed in a two-dimensional setting in order to ease the development time-wise. While great attention has been put on the fact that all the functions developed needed to be easily used in a three-dimensional situation, it is likely that a single optimisation loop would take a significant amount of time. If only the training of a neural network had to be done, that would save a significant amount of time when considering new and unknown shapes.

The neural network model developed proved more than adequate at prediction optimal tool shapes. While the remaining gaps between desired and achieved profiles are higher than those predicted by the optimisation tool, they provide with a very good first guess at the optimal tool shape.

## 6.3. Future works

Concerning the simulation tool, in its present state, it does not account for the presence of debris and the flow direction of the dielectric. While it would certainly increase the computation time of a complete simulation, the results obtained when taking the presence of debris and their eventual re-solidification would be of interest.

It is noteworthy that the simulation tool could be adapted to other machining process that involve material removal or addition. Processes such as micro-laser manufacturing or any kind of additive manufacturing are likely candidates.

Processes involving the rotation of the spindle would require some re-writing of the distance search function since it is simplified to the case of axis-aligned bounding boxes.

The simulation tool could potentially adapted to micro-EDM die-sinking in deionized water if the Electro-Chemical effects were taken into account.

It is of note that the volumetric nature of voxels could be put to advantage by using this geometrical representation to store values related to the properties or state of the material in use.

While the model built for the linking of roughness parameters and crater dimensions should perform with similar performance with different materials, some improvements could be made.

First, the case of materials with anisotropic properties hasn't been considered, it is possible that the overall shape of craters could differ in this specific situation.

Secondly, the model has been limited to craters of small dimensions, an extended campaign could be undertaken to retrieve more data points in the case of large craters and a new model involving both (small and large) crater dimensions could then be built.

Efforts should also be made towards the generalisation of the inputs of the simulation tool. All the development linked to experimental data has been made on a specific machine. Other experiments in order to collect additional data should be performed with different types of machine.

A model based on electrical data was developed for the machining gap, it would be interesting to perform the same campaign on another machine and build the same model in order to verify that looking at the electrical data between two electrodes is enough the ignore what type of machine is being used.

The optimisation process has been developed using a two-dimensional version of the simulation tool for practical purposes. However all the methods that have been designed have been done so while keeping in mind their eventual transposition into three dimensions.

A few solutions could be implemented in order to improve the rate of convergence of the tool through the exaggeration of the material added or removed during the process.

Finally, the machine learning processes applied for the building of an optimisation model would also benefit from many potential improvements. Meta-optimisation of the various parameters used when building the neural network certainly is among them.

# Addendum A

# Raw and processed data from the machining gap experimental campaign

The index symbol denotes a parameters that is a machining index and has no real unit. Values replaced by the "?" symbol couldn't be measured due to a lack of spark electrical information. Those missing values were handled by WEKA.

| **Diameter (um)** | **Energy (Index)** | **I (Index)** | **V (V)** | **Hole Diameter (mm)** | **Peak Current (A)** | **Peak Voltage (V)** | **Energy per spark (µJ)** |
|---|---|---|---|---|---|---|---|
| 150 | 206 | 15 | 80 | 0.203 | 1.36 | 7.64 | 22.3 |
| 150 | 365 | 20 | 95 | 0.212 | 1.40 | 16.9 | 10.6 |
| 150 | 206 | 15 | 110 | 0.210 | 4.60 | 16.9 | 57.5 |
| 150 | 365 | 40 | 95 | 0.228 | 1.65 | 24.5 | 20.1 |
| 150 | 206 | 15 | 140 | 0.205 | 4.42 | 23.5 | 111 |
| 150 | 365 | 20 | 70 | 0.209 | ? | ? | ? |
| 150 | 206 | 30 | 80 | 0.208 | 0.629 | 12.6 | 30.7 |
| 150 | 365 | 60 | 70 | 0.220 | ? | ? | ? |
| 150 | 206 | 30 | 110 | 0.200 | 13.4 | 20.9 | 107 |
| 150 | 365 | 60 | 70 | 0.216 | ? | ? | ? |
| 150 | 206 | 30 | 140 | 0.215 | 5.76 | 29.0 | 74.7 |
| 150 | 365 | 40 | 110 | 0.214 | 1.81 | 28.6 | 65.8 |
| 150 | 206 | 50 | 80 | 0.197 | 2.70 | 16.0 | 82.0 |
| 150 | 365 | 60 | 95 | 0.220 | 1.71 | 30.1 | 21.6 |

| Diameter (um) | Energy (Index) | I (Index) | V (V) | Hole Diameter (mm) | Peak Current (A) | Peak Voltage (V) | Energy per spark (µJ) |
|---|---|---|---|---|---|---|---|
| 150 | 206 | 50 | 110 | 0.224 | 6.34 | 24.2 | 71.0 |
| 150 | 365 | 40 | 110 | 0.216 | 1.77 | 29.7 | 24.0 |
| 150 | 206 | 50 | 140 | 0.220 | 6.12 | 30.6 | 83.3 |
| 150 | 365 | 40 | 110 | 0.218 | 1.71 | 28.1 | 22.3 |
| 150 | 365 | 40 | 110 | 0.218 | 1.92 | 25.6 | 22.7 |
| 150 | 206 | 15 | 80 | 0.208 | 0.783 | 7.54 | 29.1 |
| 150 | 206 | 15 | 110 | 0.207 | 3.26 | 16.0 | 52.7 |
| 150 | 365 | 20 | 70 | 0.203 | ? | ? | ? |
| 150 | 206 | 15 | 140 | 0.211 | 3.17 | 22.6 | 64.0 |
| 150 | 365 | 60 | 110 | 0.217 | 1.82 | 28.5 | 26.8 |
| 150 | 365 | 60 | 95 | 0.223 | 1.62 | 30.1 | 20.1 |
| 150 | 206 | 30 | 80 | 0.210 | 0.510 | 12.7 | 25.9 |
| 150 | 365 | 40 | 70 | 0.211 | ? | ? | ? |
| 150 | 206 | 30 | 110 | 0.208 | 5.24 | 21.3 | 61.8 |
| 150 | 206 | 30 | 140 | 0.211 | 5.41 | 29.1 | 72.5 |
| 150 | 365 | 20 | 95 | 0.213 | 1.51 | 17.8 | 10.8 |
| 150 | 365 | 20 | 95 | 0.210 | 1.49 | 16.3 | 12.5 |
| 150 | 206 | 50 | 80 | 0.203 | 4.28 | 18.8 | 51.8 |
| 150 | 365 | 60 | 70 | 0.222 | ? | ? | ? |
| 150 | 206 | 50 | 110 | 0.216 | 5.70 | 26.3 | 66.7 |
| 150 | 365 | 60 | 70 | 0.221 | ? | ? | ? |
| 150 | 206 | 50 | 140 | 0.210 | 7.25 | 33.0 | 84.1 |
| 150 | 206 | 15 | 80 | 0.218 | 3.84 | 6.77 | 12.4 |
| 150 | 365 | 60 | 110 | 0.227 | 1.88 | 32.9 | 36.3 |

| Diameter (um) | Energy (Index) | I (Index) | V (V) | Hole Diameter (mm) | Peak Current (A) | Peak Voltage (V) | Energy per spark (µJ) |
|---|---|---|---|---|---|---|---|
| 150 | 365 | 20 | 110 | 0.218 | 1.60 | 17.8 | 12.9 |
| 150 | 206 | 15 | 110 | 0.204 | 3.01 | 14.3 | 75.2 |
| 150 | 206 | 15 | 140 | 0.213 | 4.42 | 23.6 | 77.6 |
| 150 | 365 | 60 | 110 | 0.221 | 1.80 | 31.6 | 164 |
| 150 | 206 | 30 | 80 | 0.208 | 0.900 | 12.6 | 30.7 |
| 150 | 365 | 20 | 110 | 0.214 | 1.58 | 16.3 | 12.6 |
| 150 | 206 | 30 | 110 | 0.210 | 3.60 | 21.5 | 53.7 |
| 150 | 365 | 20 | 70 | 0.208 | ? | ? | ? |
| 150 | 365 | 40 | 70 | 0.211 | 1.04 | 8.12 | 4.49 |
| 150 | 206 | 30 | 140 | 0.203 | 6.19 | 28.9 | 132 |
| 150 | 206 | 50 | 80 | 0.208 | 0.00518 | 18.9 | 35.1 |
| 150 | 365 | 40 | 70 | 0.211 | ? | ? | ? |
| 150 | 206 | 50 | 110 | 0.214 | 6.62 | 23.5 | 70.7 |
| 150 | 365 | 40 | 95 | 0.220 | 1.67 | 22.5 | 18.5 |
| 150 | 365 | 60 | 95 | 0.219 | 1.55 | 30.7 | 20.4 |
| 150 | 206 | 50 | 140 | 0.200 | 12.1 | 33.3 | 108 |
| 150 | 365 | 20 | 110 | 0.214 | 1.60 | 15.9 | 13.0 |
| 150 | 206 | 15 | 80 | 0.225 | 3.44 | 7.32 | 32.8 |
| 150 | 206 | 15 | 110 | 0.211 | 1.47 | 17.0 | 41.4 |
| 150 | 365 | 60 | 95 | 0.221 | 1.66 | 29.8 | 24.6 |
| 150 | 365 | 40 | 95 | 0.220 | 1.65 | 24.8 | 16.8 |
| 150 | 206 | 15 | 140 | 0.214 | 4.35 | 23.9 | 65.3 |
| 150 | 206 | 30 | 80 | 0.211 | 0.950 | 13.1 | 31.4 |
| 150 | 365 | 40 | 110 | 0.218 | 1.77 | 30.8 | 21.4 |

| **Diameter (um)** | **Energy (Index)** | **I (Index)** | **V (V)** | **Hole Diameter (mm)** | **Peak Current (A)** | **Peak Voltage (V)** | **Energy per spark (µJ)** |
|---|---|---|---|---|---|---|---|
| 150 | 206 | 30 | 110 | 0.199 | 13.1 | 20.4 | 109 |
| 150 | 365 | 60 | 110 | 0.229 | 1.84 | 38.7 | 39.0 |
| 150 | 365 | 20 | 95 | 0.212 | 1.41 | 18.1 | 11.5 |
| 150 | 206 | 30 | 140 | 0.215 | 7.07 | 30.0 | 82.0 |
| 150 | 365 | 20 | 70 | 0.210 | ? | ? | ? |
| 150 | 206 | 50 | 80 | 0.216 | 2.00 | 18.0 | 36.7 |
| 150 | 365 | 60 | 110 | 0.228 | 1.84 | 26.3 | 25.0 |
| 150 | 206 | 50 | 110 | 0.211 | 6.34 | 24.2 | 71.0 |
| 150 | 365 | 20 | 110 | 0.216 | 1.59 | 17.3 | 12.8 |
| 150 | 206 | 50 | 140 | 0.207 | 10.7 | 35.1 | 96.8 |
| 150 | 365 | 40 | 70 | 0.210 | ? | ? | ? |
| 150 | 206 | 15 | 80 | 0.208 | 7.76 | 7.32 | 67.3 |
| 150 | 365 | 20 | 95 | 0.213 | 1.45 | 15.4 | 11.0 |
| 150 | 206 | 15 | 110 | 0.215 | 2.72 | 15.7 | 45.4 |
| 150 | 365 | 40 | 95 | 0.217 | 1.68 | 27.4 | 17.8 |
| 150 | 206 | 15 | 140 | 0.211 | 5.75 | 24.5 | 70.5 |
| 150 | 206 | 30 | 80 | 0.213 | 1.51 | 12.0 | 34.8 |
| 150 | 365 | 60 | 95 | 0.219 | 1.65 | 29.8 | 25.4 |
| 150 | 365 | 20 | 70 | 0.203 | ? | ? | ? |
| 150 | 206 | 30 | 110 | 0.209 | 10.3 | 18.8 | 89.4 |
| 150 | 365 | 40 | 95 | 0.223 | 1.70 | 23.5 | 16.5 |
| 150 | 206 | 30 | 140 | 0.211 | 6.52 | 27.5 | 78.9 |
| 150 | 365 | 40 | 70 | 0.212 | ? | ? | ? |
| 150 | 206 | 50 | 80 | 0.207 | 4.52 | 18.4 | 52.6 |

| Diameter (um) | Energy (Index) | I (Index) | V (V) | Hole Diameter (mm) | Peak Current (A) | Peak Voltage (V) | Energy per spark (µJ) |
|---|---|---|---|---|---|---|---|
| 150 | 365 | 20 | 110 | 0.213 | 1.56 | 16.8 | 12.0 |
| 150 | 206 | 50 | 110 | 0.204 | 6.71 | 22.9 | 75.6 |
| 150 | 365 | 60 | 70 | 0.218 | 1.45 | 14.6 | 12.5 |
| 150 | 206 | 50 | 140 | 0.216 | 7.00 | 34.8 | 82.7 |
| 300 | 365 | 60 | 120 | 0.355 | 3.15 | 48.8 | 110 |
| 300 | 206 | 50 | 140 | 0.371 | 15.0 | 44.3 | 170 |
| 300 | 206 | 10 | 80 | 0.359 | 2.03 | 18.3 | 111 |
| 300 | 365 | 60 | 80 | 0.348 | 1.07 | 24.1 | 76.4 |
| 300 | 206 | 10 | 80 | 0.363 | 3.42 | 19.0 | 90.9 |
| 300 | 365 | 40 | 100 | 0.346 | 0.926 | 22.8 | 76.9 |
| 300 | 365 | 80 | 120 | 0.365 | 4.90 | 48.0 | 117 |
| 300 | 206 | 32 | 110 | 0.368 | 18.5 | 34.6 | 179 |
| 300 | 365 | 80 | 80 | 0.355 | 1.25 | 32.9 | 80.6 |
| 300 | 206 | 10 | 140 | 0.363 | 11.1 | 33.2 | 152 |
| 300 | 365 | 60 | 120 | 0.350 | 3.55 | 43.7 | 104 |
| 300 | 206 | 32 | 140 | 0.372 | 9.65 | 39.5 | 141 |
| 300 | 365 | 60 | 80 | 0.347 | 0.928 | 22.7 | 74.2 |
| 300 | 206 | 10 | 110 | 0.370 | 11.5 | 24.5 | 134 |
| 300 | 206 | 50 | 80 | 0.373 | 6.38 | 29.5 | 106 |
| 300 | 365 | 60 | 120 | 0.348 | 3.45 | 38.5 | 105 |
| 300 | 206 | 10 | 140 | 0.363 | 5.60 | 33.7 | 120 |
| 300 | 365 | 40 | 120 | 0.349 | 2.31 | 39.2 | 105 |
| 300 | 365 | 40 | 80 | 0.343 | 1.89 | 17.6 | 61.0 |
| 300 | 206 | 32 | 110 | 0.372 | 27.8 | 34.3 | 210 |

| Diameter (um) | Energy (Index) | I (Index) | V (V) | Hole Diameter (mm) | Peak Current (A) | Peak Voltage (V) | Energy per spark (μJ) |
|---|---|---|---|---|---|---|---|
| 300 | 365 | 80 | 80 | 0.355 | 0.437 | 36.3 | 86.6 |
| 300 | 206 | 10 | 110 | 0.370 | 11.4 | 27.5 | 137 |
| 300 | 206 | 32 | 110 | 0.367 | 10.9 | 33.9 | 132 |
| 300 | 365 | 80 | 100 | 0.348 | 1.78 | 43.6 | 104 |
| 300 | 365 | 40 | 80 | 0.344 | 2.04 | 17.8 | 60.1 |
| 300 | 206 | 50 | 80 | 0.371 | 18.7 | 31.3 | 166 |
| 300 | 365 | 80 | 100 | 0.349 | 1.43 | 40.3 | 113 |
| 300 | 206 | 32 | 140 | 0.371 | 15.9 | 37.3 | 166 |
| 300 | 206 | 32 | 80 | 0.373 | 3.73 | 26.1 | 90.4 |
| 300 | 365 | 80 | 120 | 0.355 | 6.55 | 48.0 | 113 |
| 300 | 365 | 80 | 120 | 0.355 | 3.52 | 48.0 | 145 |
| 300 | 206 | 50 | 110 | 0.371 | 13.9 | 37.4 | 162 |
| 300 | 365 | 40 | 80 | 0.345 | 0.863 | 13.5 | 62.5 |
| 300 | 206 | 32 | 80 | 0.367 | 5.10 | 26.1 | 99.6 |
| 300 | 365 | 40 | 100 | 0.343 | 0.999 | 26.7 | 83.5 |
| 300 | 206 | 32 | 80 | 0.367 | 1.79 | 26.3 | 83.7 |
| 300 | 206 | 10 | 140 | 0.371 | 9.40 | 32.2 | 138 |
| 300 | 365 | 80 | 100 | 0.353 | 1.42 | 40.9 | 97.6 |
| 300 | 206 | 10 | 110 | 0.379 | 11.9 | 26.8 | 143 |
| 300 | 365 | 60 | 100 | 0.387 | 2.57 | 38.3 | 87.7 |
| 300 | 206 | 50 | 110 | 0.364 | 10.2 | 38.4 | 138 |
| 300 | 365 | 60 | 80 | 0.345 | 0.760 | 31.4 | 71.6 |
| 300 | 365 | 40 | 120 | 0.346 | 2.32 | 32.7 | 94.9 |
| 300 | 206 | 32 | 80 | 0.375 | 5.17 | 26.0 | 165 |

| Diameter (um) | Energy (Index) | I (Index) | V (V) | Hole Diameter (mm) | Peak Current (A) | Peak Voltage (V) | Energy per spark (µJ) |
|---|---|---|---|---|---|---|---|
| 300 | 365 | 40 | 100 | 0.347 | 0.735 | 30.3 | 76.4 |
| 300 | 206 | 10 | 140 | 0.370 | 12.0 | 30.3 | 157 |
| 300 | 365 | 80 | 80 | 0.390 | 1.91 | 36.6 | 82.0 |
| 300 | 206 | 32 | 140 | 0.370 | 12.1 | 40.5 | 149 |
| 300 | 206 | 32 | 140 | 0.371 | 19.6 | 40.8 | 185 |
| 300 | 365 | 60 | 120 | 0.362 | 1.63 | 49.6 | 125 |
| 300 | 365 | 80 | 100 | 0.366 | 1.17 | 41.9 | 108 |
| 300 | 206 | 10 | 110 | 0.375 | 7.83 | 27.7 | 117 |
| 300 | 206 | 10 | 110 | 0.372 | 9.75 | 26.6 | 134 |
| 300 | 365 | 40 | 80 | 0.354 | 2.42 | 18.5 | 59.5 |
| 300 | 365 | 40 | 80 | 0.347 | 2.16 | 12.0 | 60.8 |
| 300 | 206 | 50 | 80 | 0.368 | 24.7 | 28.8 | 208 |
| 300 | 206 | 50 | 110 | 0.370 | 16.3 | 39.3 | 167 |
| 300 | 365 | 80 | 120 | 0.394 | 3.29 | 46.1 | 141 |
| 300 | 206 | 50 | 140 | 0.363 | 14.5 | 43.8 | 171 |
| 300 | 365 | 60 | 100 | 0.393 | 0.449 | 39.9 | 85.4 |
| 300 | 365 | 60 | 80 | 0.378 | 1.40 | 27.5 | 74.1 |
| 300 | 206 | 10 | 80 | 0.375 | 2.37 | 18.6 | 85.7 |
| 300 | 206 | 50 | 140 | 0.365 | 19.0 | 44.3 | 180 |
| 300 | 365 | 80 | 120 | 0.399 | 4.79 | 49.9 | 115 |
| 300 | 365 | 60 | 100 | 0.381 | 1.50 | 36.4 | 85.0 |
| 300 | 206 | 10 | 80 | 0.366 | 1.01 | 18.0 | 76.1 |
| 300 | 206 | 50 | 80 | 0.371 | 15.3 | 29.8 | 153 |
| 300 | 365 | 80 | 80 | 0.378 | 3.39 | 31.5 | 82.6 |

| **Diameter (um)** | **Energy (Index)** | **I (Index)** | **V (V)** | **Hole Diameter (mm)** | **Peak Current (A)** | **Peak Voltage (V)** | **Energy per spark (µJ)** |
|---|---|---|---|---|---|---|---|
| 300 | 365 | 40 | 100 | 0.385 | 1.52 | 29.4 | 87.4 |
| 300 | 206 | 50 | 110 | 0.376 | 8.26 | 38.8 | 129 |
| 300 | 206 | 10 | 140 | 0.363 | 5.46 | 31.5 | 117 |
| 300 | 365 | 60 | 80 | 0.385 | 1.04 | 23.9 | 73.6 |
| 300 | 206 | 32 | 110 | 0.365 | 30.6 | 34.3 | 224 |
| 300 | 365 | 80 | 80 | 0.391 | 1.93 | 36.8 | 75.6 |
| 300 | 206 | 32 | 80 | 0.370 | 10.1 | 26.1 | 127 |
| 300 | 365 | 60 | 100 | 0.390 | 1.55 | 32.0 | 86.3 |
| 300 | 365 | 60 | 120 | 0.354 | 1.51 | 41.8 | 126 |
| 300 | 206 | 50 | 140 | 0.368 | 11.6 | 44.9 | 158 |
| 300 | 365 | 40 | 120 | 0.378 | 2.20 | 34.0 | 93.0 |
| 300 | 206 | 32 | 110 | 0.368 | 20.2 | 34.3 | 194 |
| 300 | 365 | 40 | 120 | 0.376 | 1.89 | 36.6 | 101 |
| 300 | 206 | 50 | 140 | 0.366 | 14.9 | 44.3 | 171 |
| 300 | 206 | 50 | 110 | 0.374 | 6.64 | 40.0 | 118 |
| 300 | 365 | 80 | 100 | 0.383 | 1.29 | 42.8 | 116 |
| 300 | 206 | 50 | 80 | 0.372 | 11.4 | 29.8 | 134 |
| 300 | 365 | 40 | 100 | 0.381 | 0.452 | 24.5 | 79.9 |
| 300 | 206 | 32 | 140 | 0.371 | 10.9 | 39.5 | 149 |
| 300 | 365 | 60 | 100 | 0.384 | 1.69 | 32.8 | 82.8 |
| 300 | 365 | 40 | 120 | 0.383 | 2.84 | 31.8 | 95.3 |
| 300 | 206 | 10 | 80 | 0.371 | 1.30 | 17.7 | 64.6 |

# Addendum B

# Dimensions of the shapes made for the validation of the roughness and machining gap models

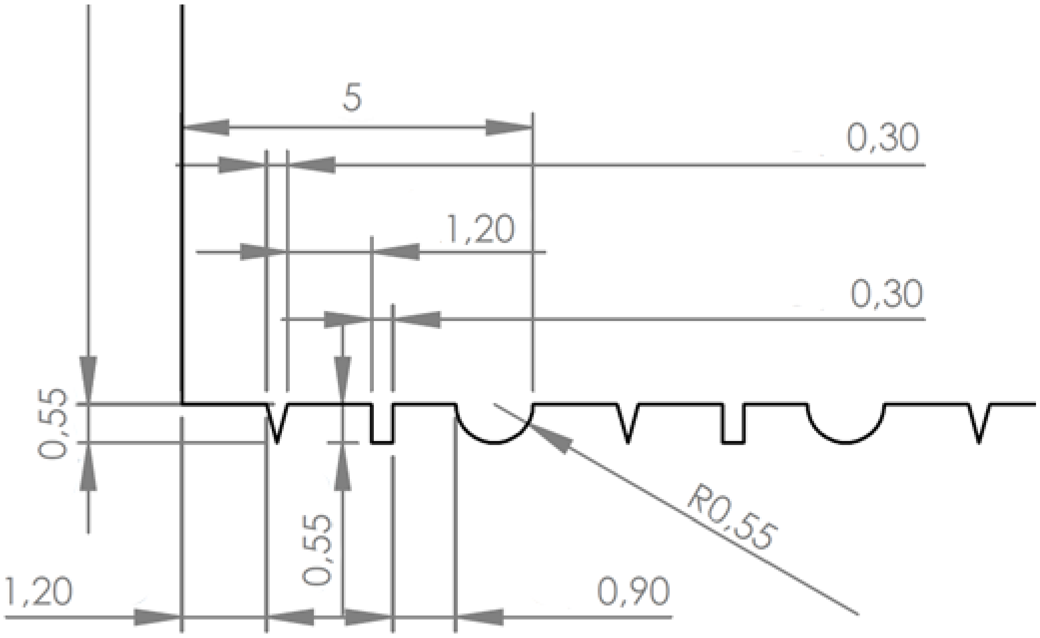

Figure 74: Dimensions of the shapes made for the validation of the roughness and machining gap models

# Addendum C

# Target workpiece profiles used in the training of the Neural Network

Those are the workpiece profiles that were used to train the neural network in section 5.2. The side dimension is 1024 µm for all shapes.

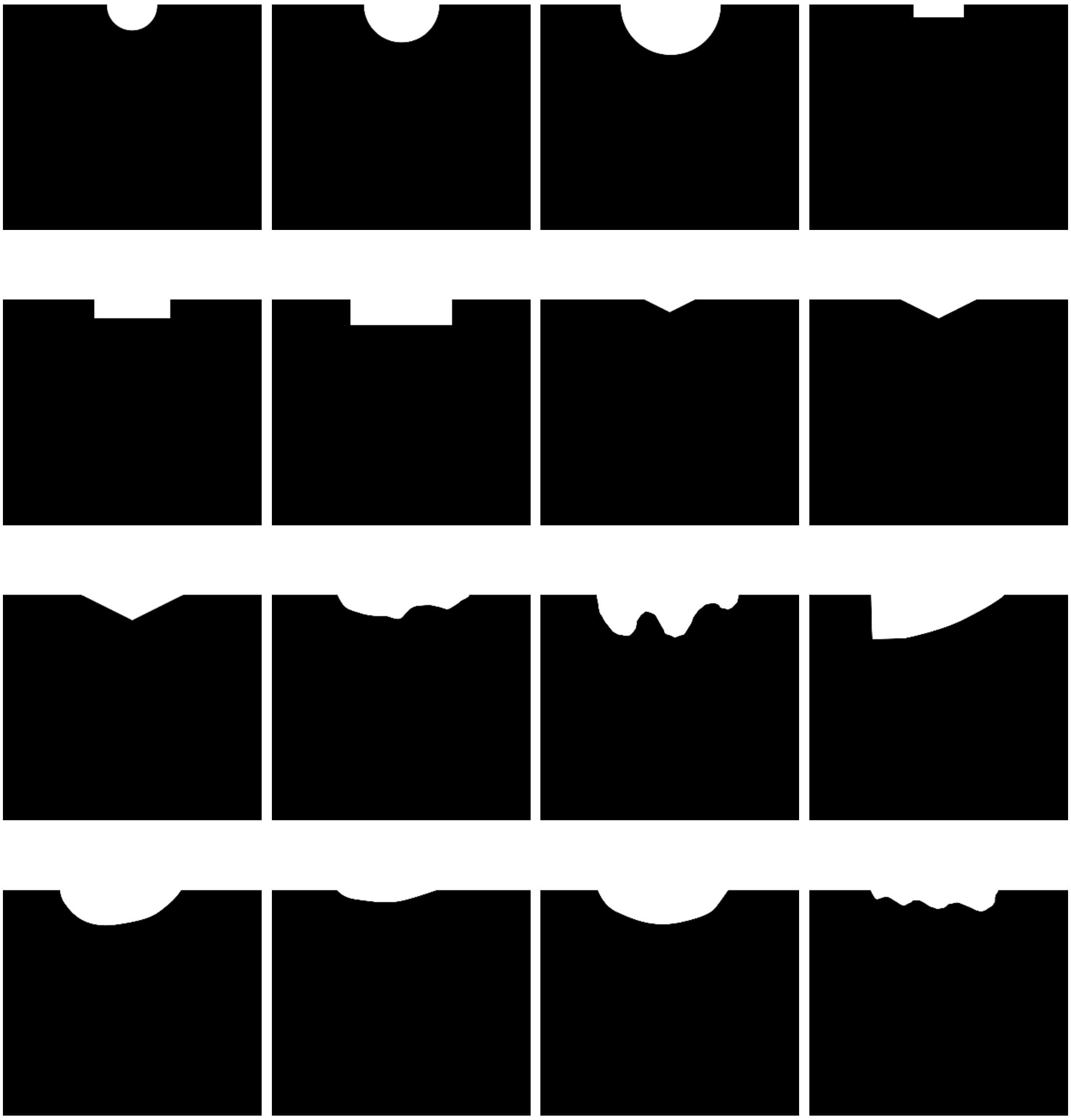

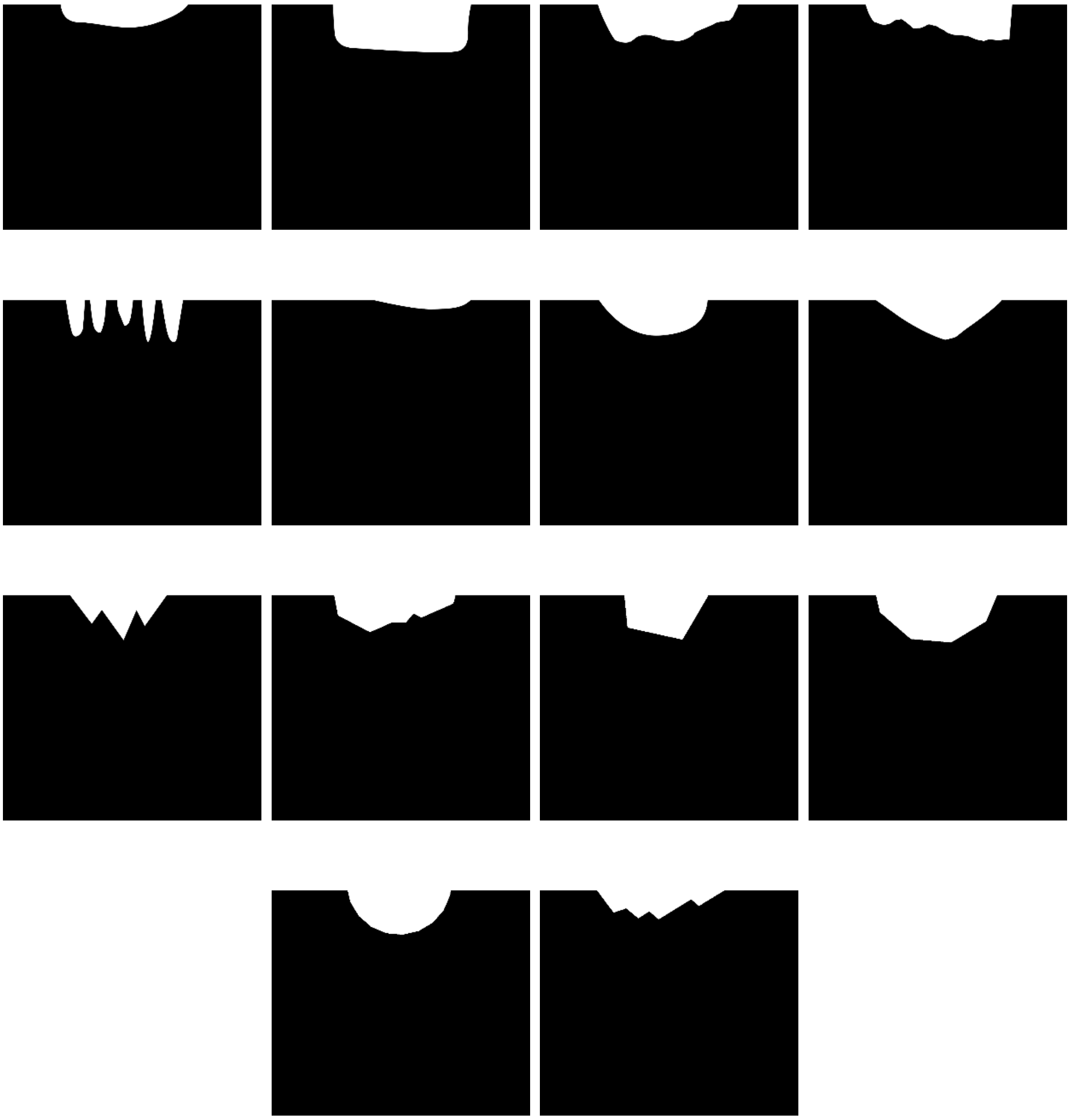

Figure 75: The thirty shapes used in the training of the Neural Network aimed at shape optimisation.

# References

Alting, L., Kimura, F., Hansen, H., & Bissacco, G. (2003). Micro engineering. *CIRP Annals - Manufacturing Technology, 52*(2), 635-657.

Arbizu, I., & Pérez, C. (n.d.). *History and foundations of EDM: the least conventional of the machining.* Retrieved April 24, 2013, from http://www.interempresas.net/MetalWorking/Articles/12068-The-least-conventional-of-the-machining.html

Beck, J. (1981). Transient temperatures in a semi-infinite cylinder heated by a disk heat source. *International Journal of Heat and Mass Transfer, 24*(10), 1631-1640.

Beck, J. (1981). Transient temperatures in a semi-infinite cylinder heated by a disk heat source. *International Journal of Heat and Mass Transfer, 24*(10), 1631-1640.

Bigot, S., Ivanov, A., & Popov, K. (2005). A study of the micro EDM electrode wear. *4M 2005 - First International Conference on Multi-Material Micro Manufacture*, (pp. 355-358). Retrieved February 27, 2014, from 4M Association website: http://www.4m-association.org/content/Electro-Discharge-Machining-0

Blateyron, F. (n.d.). *Surface texture - Areal field parameters.* Retrieved May 1, 2015, from http://www.digitalsurf.com/en/guidearealfieldparameters.html

Bleys, P., Kruth, J.-P., Lauwers, B., Zryd, A., Delpretti, R., & Tricarico, C. (2002). Real-time tool wear compensation in milling EDM. *CIRP Annals - Manufacturing Technology, 51*(1), 157-160.

Borrman, A., Schraufstetter, S., van Treeck, C., & Rank, E. (2007). An iterative, octree-based algorithm for distance computation between polyhedra with complex surfaces. *Proceedings of the International ASCE Workshop on Computing in Civil Engineering.*

Campana, S., & Miyazawa, S. (1999). Micro EDM and ECM in DI water. *Proceedings of the Annual Meeting of American Society of Precision Engineering (ASPE).*

Cassandra, A., Littman, M., & Zhang, N. (1997). Incremental pruning: a simple, fast, exact method for partially observable Markov decision processes. *Proceedings of the Thirteenth Annual Conference on Uncertainty in Artificial Intelligence (UAI-97)*, (pp. 54-61).

Cignoni, P., Rocchini, C., & Scopigno, R. (1998). Metro: Measuring error in simplified surfaces. *Computer Graphics Forum, 17*(2), 167-174.

Das, S., Klotz, M., & Klocke, F. (2003). EDM simulation: Finite element-based calculation of deformation, microstructure and residual stresses. *Journal of Material Processing Technology.*

Descoeudres, A., Hollenstein, G., Walder, G., & Perez, R. (2005). Time-resolved imaging and spatially resolved spectroscopy of electrical discharge machining plasma. *Journal of Applied Physics, 38*, 4066-4073.

DiBitonto, D., Eubank, P., Patel, M., & Barrufet, M. (1989). Theoretical models of the electrical discharge machining process I: A simple cathode erosion model. *Journal of Applied Physics, 66*, 4095-4103.

DiBitonto, D., Eubank, P., Patel, M., & Barrufet, M. (1989). Theoretical models of the electrical discharge machining process II: The anode erosion model. *Journal of Applied Physics, 66*, 4104-4111.

Dimov, S., Brousseau, E., Minev, R., & Bigot, S. (2012). Micro- and nano-manufacturing: Challenges and opportunities. *Proceedings of IMechE Part C: Journal of Mechanical Engineering Science, 226*, 3-15.

Feynman, R. (1960). There's plenty of room at the bottom. *Engineering and Science, 23*(5), 22-36.

Gargantini, I. (1982). Linear octtrees for fast processing of three-dimensional objects. *Computer Graphics and Image Processing, 20*(4), 365-374.

Geiger, M. e. (2001). Microforming. *Annals of the CIRP*, 50(2):445-462.

Glassner, A. S. (1984). Space subdivision for fast ray-tracing. *IEEE Compute Graphics and Applications, 4*(10), 15-22.

Guitrau, E. (1997). *The EDM handbook.* Carl Hanser Verlag GmbH & Co.

Han, F., Cheng, G., Feng, Z., & Isago, S. (2008). Thermo-mechanical analysis and optimal tension control of micro wire electrode. *International Journal of Machine Tools and Manufacture, 48*(7-8), 922-931.

Han, F., Yamada, Y., Kawakami, T., & Kunieda, M. (2006). Experimental attempts of sub-micrometer order size of machining using micro-EDM. *Precision Engineering, 30*, 123-131.

Heaton, J. (2011). *Introduction to the math of neural networks.* Heaton Research, Inc.

Heaton, J. (2013). *Artificial intelligence for humans, volume 1: Fundamental algorithms.* CreateSpace Independent Publishing Platform.

Heo, S., Jeong, Y., Min, B.-K., & Lee, S. (2009). Virtual EDM simulator: Three-dimensional geometric simulation of micro-EDM processes. *International Journal of Machine Tool & Manufacture, 49*, 1029-134.

Ho, K., & Newman, S. (2003). State of the art electrical discharge machining (EDM). *International Journal of Machine Tools and Manufacture, 43*, 1287-1300.

Ho, K., Newman, S., Rahimifard, S., & Allen, R. (2004). State of the art wire electrical discharge machining. *International Journal of Machine Tools and Manufacture, 44*, 1247-1259.

Holmes, G., Donkin, A., & Witten, I. (1994). WEKA: A machine learning workbench. *Proceedings of the Second Australia and New Zealand Conference on Intelligent Information Systems.* Brisbane.

Izquierdo, B., Sanchez, J., Plaza, S., & Ortega, N. (2009). A numerical model of the EDM process considering the effect of multiple discharges. *International Journal of Machine Tools and Manufacture, 49*, 220-229.

Jaham, M. P. (2013). Micro-electrical discharge machining. In J. P. Davim, *Nontraditional machining processes.*

Jahan, M. P., Rahman, M., & Wong, Y. S. (2011). A review on the conventional and micro-electro discharge machining of tungsten carbide. *International Journal of Machine Tools & Manufacture*, 837–858.

Jameson, E. C. (2001). *Electrical Discharge Machining.* Society of Manufacturing Engineers.

Karafuji H, M. T. (1968). Micro-EDM of cemented carbide alloys. *Japanese Society of Electrical Machining Engineers, 2*(3), 1-16.

Katz, Z., & Tibbles, C. (2005). Analysis of micro-scale EDM process. *International Journal of Advanced Manufacturing Technology, 25*(9-10), 923-928.

Kaufman, A., Cohen, D., & Yagel, R. (1993). *Volume Graphics.*

Kennedy, J., & Eberhart, R. (1995). Particle swarm optimization. *Proceedings of IEEE International Conference on Neural Networks IV*, (pp. 1942-1948).

Kinoshita, N., Fukui, M., & Gamo, G. (1982). Control of wire-EDM prevent electrode forom breaking. *Annals of the CIRP, 31*(1), 111-114.

Kirkpatrick, S., Gelatt, C., & Vecchi, M. (1983). Optimization by simulated annealing. *Science, 220*(4598), 671-680.

Klocke, F., Lung, D., Thomaidis, D., & Antonoglou, G. (2004). Using ultra thin electrodes to produce micro-parts with wire-EDM. *Journal of Materials Processing Technology, 149*(1-3), 579-584.

Knoll, A. (2006). A survey of octree volume rendering methods. *Proceedings of 1st IRTG Workshop.*

Knowles, M., Rutterford, G., Karnakis, D., Dobrev, T., Petkov, P., & Dimov, S. (2006). Laser micro-milling of ceramics, dielectrics and metals using nanosecond and picosecond lasers. *Proceedings of the Second International Conference on Multi-Material Micro Manufacture*, (pp. 131-134).

Kojima, A., Natsu, W., & Kunieda, M. (2007). Observation of arc plasma xxpansion and delayed growth of discharge crater in EDM. *Proceedings of the 15th International Symposyum on Electromachining*, (pp. 1-4).

Kudryavtsev, L., & Samarin, M. (2011). *Lagrange interpolation formula.* Retrieved April 6, 2015, from Encyclopedia of Mathematics: http://www.encyclopediaofmath.org/index.php?title=Lagrange_interpolation_formula&oldid=17497

Kunieda, M., Kaneko, Y., & Natsu, W. (2012). Reverse simulation of sinking EDM applicable to large curvatures. *Precision Engineering, 36*(2), 238-243.

Kunieda, M., Kowaguchi, W., & Takita, T. (1999). Reverse simulation of die-sinking EDM. *CIRP Annals - Manufacturing Technology, 48*(1), 115-118.

Kunieda, M., Lauwers, B., Rajurkar, K., & Schumacher, B. (2005). Advancing EDM through fundamental insight into the process. *Annals of the CIRP, 54*(2), 64:87.

Kuo, C., Chen, S., Wu, Y., Yan, T., & Masuzawa, T. (1997). Study on 3D micro edm. *Proceedings of the Annual Assembly of Japan Society of Electrical Machining Engineers*, (pp. 111-114).

Lazarenko, B., & Lazarenko, N. (1944). Electrical erosion of metals (in Russian). 27.

Leach, R. (2013). *Characterisation of areal surface texture.* Springer.

Livshiz, A. L. (1957). *Electroerosive machining metals (in Russian).*

Mahendran, S., Devarajan, R., Nagarajan, T., & Majdi, A. (2010). A review of micro-EDM. *Proceedings of the International MultiConference of Engineers and Computer Scientists Vol. II, IMECS.* Hong Kong.

Maradia, U., Boccadoro, M., Stirnimann, J., Beltrami, I., Kuster, F., & Wegener, K. (2012). Die-sink EDM in meso-micro machining. *Procedia CIRP 1*, (pp. 166-171).

Maradia, U., Scuderi, M., Knaak, R., Boccadoro, M., Beltrami, I., & Stirnimann, J. (2013). Super-finished surfaces using meso-micro EDM. *Proceedings of the Seventeenth CIRP Conference on Electro Physical and Chemical Machining (ISEM)*, (pp. 157-162).

Masuzawa, T. (2000). State of the art of micromachining. *Annals of the CIRP, 49*(2), 473-488.

McGeough, J., Leu, M., Rajurkar, J., De Silva, A., & Liu, Q. (2001). Electroforming process and application to micro/macro manufacturing. *Annals of the CIRP, 50*(2), 499-514.

Menz, W. e. (2002). Non-conventional technologies for fabrication of micro-systems. *Proceedings of the 3rd Euspen International Conference*, 3-6.

Ministero de Ciencia e Innovaciòn. (n.d.). *Micro manufacturing, differences between macro and micro-EDM.* Retrieved Dec 2012, from http://www.micromanufacturing.net/didactico/Desarollo/edm-eng/6-differences-between-macro-and-micro-edm.

Mitutoyo America Corporation. (2012). *Surface roughness measurement.* Retrieved January 17, 2015, from Mitutoyo America Corporation website: http://www.mitutoyo.com/wp-content/uploads/2012/11/1984_Surf_Roughness_PG.pdf

Mounier, E. (2002). MEMS, the alternative semiconductor business. *Proceedings of the 3rd Euspen International Conference*, 391-394.

Narasimhan, J., & Rajurkar, K. (2005). Tool wear compensation and path generation in micro and macro EDM. *Journal of Manufacturing Processes, 7*(1), 75-82.

Nelder, J., & Mead, R. (1965). A simplex method for function minimization. *Computer Journal, 7*, 308-313.

Pandey, P., & Jilani, S. (1986). Plasma channel growth and the re-solidified layer in EDM. *Precision Engineering, 8*(2), 104-110.

Pham, D., Ivanov, A., Bigot, S., Popov, K., & Dimov, S. (2007). An investigation of tube and rod electrode wear in micro-EDM dilling. *International Journal of Advanced Manufacturing Technology, 33*, 103-109.

Piegl, L., & Tiller, W. (1997). *The NURBS book* (2nd ed.). Springer.

Potz, D., Christ, W., & Dittus, B. (2000). *Diesel nozzle—the determining interface between injection system and combustion chamber, Thermo- and Fluid-dynamic Processes in Diesel engines.* Springer.

Qian, J., Wang, J., Ferraris, E., & Reynaerts, D. (2013). A holistic approach for zero-defect micro-EDM milling. *IEEE International Symposium on Assembly and Manufacturing (ISAM)*, (pp. 226-229).

Rajurkar, K. P., & Wang, W. M. (1991). On-line monitor and control for wire breakage in WEDM. *CIRP Annals, 40*(1), 219-222.

Rajurkar, K., & Wang, W. (1991). On-line monitor and control for wire breakage in WEDM. *Annals of the CIRP, 40*(1), 219-222.

Rajurkar, K., Levy, G., Mashe, A., Sundaram, M., McGeough, J., Hu, X., . . . DeSilva, A. (2006). Micro and nano machining by electro-physical and chemical processes. *CIRPS Annals - Manufacturing Technology, 55*(2), 643-666.

Ren, Y., Zhu, W., & Lee, Y. (2008). Tri-dexel volumetric modeling for haptic sculpting and virtual prototyping of complex surfaces. *Transactions - North American Manufacturing Research Institution of SME*, (pp. 97-104).

Sanchez, J. A., Plaza, S., Gila, R., Ramos, J. M., Izquierda, B., Ortega, N., & Pombo, I. (2013). Electrode set-up for EDM-drilling of large aspect-ratio microholes. *Procedia CIRP 6 - The Seventeenth CIRP Conference on Electro Physical and Chemical Machining (ISEM),*, 275–280.

Santini, M., & Guilizzoni, M. (2014). 3D X-ray micro computed tomography on multiphase drop interfaces: From biomimetic to functional applications. *Colloids and Interface Science Communications, 1*, 14-17.

Santini, M., Guilizzoni, M., & Fest-Santini, S. (2013). X-ray computed microtomography for drop shape analysis and contact angle measurement. *Journal of Colloid and Interface Science, 409*, 204-210.

Schumacher B M, K. R. (2013). Historical phases of EDM development driven by the dual influence of "market pull" and "science push". *Proceedings of the*

*Seventeenth CIRP Conference on Electro Physical and Chemical Machining (ISEM)*, (pp. 5-12).

Schwarz, M., & Seidel, H.-P. (2010). Fast parallel surface and solid voxelization on GPUs. *ACM Transactions on Graphics*, *29.*

Shao, B., & Rajurkar, K. (2013). Micro-EDM pulse energy distribution ratio determination. *Proceedings of the 8th International Conference on Micromanufacturing.* Victoria.

Singh, A., & Ghosh, A. (1999). A thermo-electrical model of material removal during electric discharge machining. *International Journal of Machine Tools and Manufacture, 39*, 669-682.

Snoeys, R., & Van Dijck, F. (1971). Investigation of electro discharge machining operations by means of thermo-mathematical model. *CIRP Annals, 20*(1), 35-36.

Snoeys, R., & Van Dijck, F. (1972). Plasma channel diameter growth affects stock removal in EDM. *CIRP Annals, 21*(1), 39-40.

Springborn, R. (1976). *Non-traditional machining processes.* American Society of Tool and Manufacturing.

Storn, R. (1996). On the usage of differential evolution for function optimization. *Biennial Conference of the North American Fuzzy Information Processing Society (NAFIPS)*, (pp. 519-523).

Takahata, K. (2009). Micro-electro-discharge machining technology for MEMS. *Micro Electron Mech Syst INTECH*, 144-164.

Tricarico, C., Delpretti, R., & Dauw, D. (1988). Geometrical simulation of the EDM die-sinking process. *CIRP Annals: Manufacturing Technology, 37*(1), 191-196.

Uhlmann, E., Piltz, S., & Doll, S. (2005). Machining of micro/miniature dies and moulds by electrical discharge machining - Recent developments. *Journal of Materials Processing Technology, 167*(2-3), 488-493.

Van Brussel, H., Peirs, J., Reynaerts, D., Delchambre, A., Reinhart, G., Roth, N., . . . Zussman, E. (2000). Assembly of micro-systems. *Annals of the CIRP, 49*(2), 451-472.

Van Dijck, F., & Dutre, W. (1974). Heat conduction model for the calculation of the volume of molten material in electric discharges. *Journal of Physics D, 7*, 899-910.

Wang, J., Ferraris, E., Galbiati, M., Qian, J., & Reynaerts, D. (2013). Combined pulse characterization and discrimination for micro-EDM milling tool wear study. *Proceedings of the 10th International Conference on Multi-Material Micro Manufacture.*

Wilhelms, J., & Van Gelder, A. (1992). Octrees for faster isosurface generation. *ACM Transactions on Graphics, 11*(3), 201-227.

Yan, M., & Liao, Y. (1996). Monitoring and self-learning fuzzy control for wire rupture prevention in wire electrical discharge machining. *International Journal of Machine Tools and Manufacture, 36*(3), 339-353.

Yang, X., Guo, J., Chen, X., & Kunieda, M. (2011). Molecular dynamics simulation of the material removal mechanism in micro-EDM. *Precision Engineering, 35*(1), 51-57.

Yu, Z., Masuzawa, T., & Fujino, M. (1998). Micro-EDM for three-dimensional cavities - Development of uniform wear method. *CIRP Annals - Manufacturing technology, 47*(1), 169-172.

Yuzawa, T., Magara, T., Imai, Y., & Sato, T. (1997). Micro electric discharge dcanning using a mini-size cylindrical electrode. *Kata Gijutsu, 12*, 104-105.

Zahiruddin, M., & Masanori, K. (2012). Comparison of energy and removal efficiencies between micro and macro EDM. *CIRP Annals - Manufacturing Technology, 61*, 187-190.

Zhang, L., Jia, Z., Liu, W., & Li, A. (2012). A two-stage servo feed controller of micro-EDM based on interval type-2 fuzzy logic. *International Journal of Advanced Manufacturing Technology, 59*(5-8), 633-645.

Zhao, Y., Zhang, X., Liu, X., & Yamazaki, K. (2004). Geometric modeling of the linear motor driven electrical discharge machining (EDM) die-sinking process. *International Journal of Machine Tools and Manufacture, 44*(1), 1-9.